Application of Optical Diagnostics to Support the Development of Industrial Gas Turbine Combustors

Von der Fakultät für Ingenieurwissenschaften, Abteilung Maschinenbau und Verfahrenstechnik
der
Universität Duisburg-Essen

zur Erlangung des akademischen Grades

eines

Doktors der Ingenieurwissenschaften

Dr.-Ing.

genehmigte Dissertation

von

Benjamin Witzel
aus
Duisburg

Gutachter: Univ.-Prof. Dr. rer. nat. Christof Schulz
Univ.-Prof. Dr.-Ing. Theo H. van der Meer

Tag der mündlichen Prüfung: 27.11.2015

Kurzfassung

Die vorliegende Dissertationsschrift behandelt die Anwendung moderner optischer Messverfahren zum Zwecke der detaillierten Untersuchung von Verbrennungssystemen stationärer Gasturbinen.

Mittels laserinduzierter Fluoreszenz (LIF) von Aceton als Tracer wurden bildgebende Messungen des Brennstoff-/Luftgemisches verschiedener Brennertypen bei atmosphärischem Druck im nichtreagierenden System durchgeführt. Hierzu wurden spezielle optisch zugängliche Prüfstände sowie eine Versorgungseinrichtung zur Bereitstellung der erforderlichen Tracer-Massenströme entwickelt und in Betrieb genommen. Die Ergebnisse der Tracer-LIF-Messungen wurden mit Ergebnissen klassischer Saugsonden-Messungen verglichen. Dabei konnte gezeigt werden, dass die Tracer-LIF-Messungen deutliche Vorteile hinsichtlich der räumlichen Auflösung sowie der benötigten Zeit zur Durchführung einer Messung bieten. Im Gegensatz zu den Saugsonden-Messungen ermöglichen die Tracer-LIF-Messungen nun auch erstmalig die Untersuchung instationärer Phänomene. Die aufgenommenen Mischungsdaten dienen darüber hinaus als neue Referenz zur Validierung numerischer Simulationen. So konnten bei einem im Rahmen dieser Arbeit durchgeführten Vergleich mit RANS CFD-Simulationen, die von Dr. Lukasz Panke zur Verfügung gestellt wurden, bereits optimierte Parameter für die Durchführung der Simulationen gefunden werden.

Zur Untersuchung des Verhaltens der Flamme in Hochdruck-Verbrennungstests wurde eine wassergekühlte Sonde entwickelt, welche optischen Zugang zur Brennkammer bei minimaler Beeinflussung des untersuchten Systems bietet. Mithilfe der Sonde wurden sowohl spektroskopische wie auch bildgebende Messungen des Flammeneigenleuchtens unter verschiedenen realistischen thermodynamischen Randbedingungen durchgeführt. Für die bildgebenden Messungen wurden verschiedene Kombinationen von optischen Filtern vor der Kamera ein-

gesetzt, um selektiv OH*, CH* oder CO_2* aufnehmen zu können. Simultan zu den Kamerabildern wurden Wechseldruck-Schwankungen innerhalb der Brennkammer aufgezeichnet. Eine nachträgliche Korrelation der aufgenommenen Flammenbilder mit den Wechseldruck-Schwankungen mittels eines Phasensortier-Algorithmus gab dabei neue Einblicke in die Vorgänge innerhalb der Brennkammer während des Auftretens von Verbrennungsinstabilitäten.

Insgesamt ermöglichten die im Rahmen dieser Arbeit angewandten optischen Messtechniken neue Einblicke in die komplexen Vorgänge bei der Gemischbildung von Brennstoff in Luft sowie bei der Verbrennung unter realistischen Randbedingungen. Die dabei gewonnenen Erkenntnisse leisten einen wichtigen Beitrag zur Weiterentwicklung von Gasturbinen-Verbrennungssystemen.

Abstract

The present study is concerned with the application of state-of-the-art optical measurement techniques for the detailed investigation of combustion systems of stationary gas turbines.

By using laser-induced fluorescence (LIF) with acetone as tracer imaging measurements of the fuel/air mixture at atmospheric pressure and at non-reacting conditions were accomplished with different burner types. For this purpose optically accessible test rigs as well as a special facility for the supply with necessary tracer mass flows were developed and taken into operation. The results of the tracer-LIF measurements were compared to results of classical suction-probe measurements. It could be shown that the tracer LIF measurements offer clear advantages regarding the spatial resolution as well as the necessary time for the execution of a measurement. Moreover, contrary to the suction-probe measurements, the tracer-LIF measurements for the first time allow the investigation of unsteady phenomena. Additionally, the recorded mixture data serve as a new reference for the validation of numerical simulations. A first comparison with steady RANS CFD results provided by Dr. Lukasz Panek within the context of this study could already lead to optimized parameters for these simulations.

For the investigation of the flame behavior in high pressure combustion tests a water-cooled probe was developed which provides optical access to the combustion chamber with minimum impact on the examined system. The probe was applied for both spectroscopic as well as imaging measurements of the flame luminescence at gas turbine relevant thermodynamic boundary conditions. For the imaging measurements different combinations of optical filters were installed in front of the camera system in order to selectively record OH*, CH* or CO_2*. Pressure fluctuations inside the combustion chamber were recorded simultaneously to the camera images. A correlation of the recorded images with the pressure fluctuations by using a

phase-sorting algorithm gave new inside of the processes within the combustion chamber during the occurrence of combustion instabilities.

Altogether the optical measurement techniques applied in the frame of this study enabled new insights into the complex processes during fuel/air mixing as well as during combustion at gas turbine relevant boundary conditions. The new knowledge won thereby will make an important contribution for the further development of gas turbine combustion systems.

Contents

Nomenclature

Latin symbols

Symbol	Dimension	Description
A	m^2	Area
f	mm	Focal length
h	J s	Planck's constant
J	-	Fuel/air momentum flux ratio
p	Pa	Pressure
$\dot{m}$	kg s^{-1}	Mass flow
P	MW	Power
P^*	%	Relative power output
R	J (kg K)$^{-1}$	Specific gas constant
SF	-	Scaling factor
T	K	Temperature
v	m s^{-1}	Velocity

Greek symbols

Symbol	Dimension	Description
ζ	-	Friction factor
λ	-	Air factor (= Φ^{-1})
λ	nm	Wavelength
ν	Hz	Photon frequency
ρ	kg m^{-3}	Density
ϕ	-	Equivalence ratio (= λ^{-1})

Superscripts

*	Electronically excited state

Subscripts

0	Jet flow (typically fuel)
∞	Main flow (typically air)
Exp	Experimental conditions
GT	Real gas turbine conditions
Th	Thermal

Abbreviations

2-D	2-dimensional
3-D	3-dimensional
BLZ	*Bayerisches Laser Zentrum* (Bavarian laser centre)
CAR	Cooling-air reduced combustion chamber
CARS	Coherent anti-Stokes Raman spectroscopy
CBO	Cylindrical burner outlet
CCD	Charge-coupled device
CDPO	Combustion driven pressure oscillations
CFD	Computational fluid dynamics
CMOS	Complementary metal oxide semiconductor
CP	Cover plate
CRDS	Cavity ring-down spectroscopy
DES	Detached eddy simulation
DFWM	Degenerate four-wave mixing
DGV	Doppler global velocimetry
DLR	*Deutsches Zentrum für Luft- und Raumfahrt* (German Aerospace Centre)
DNS	Direct numerical simulation
EU	European Union
FID	Flame-ionisation detector
FP	Flow parameter
FRS	Filtered Rayleigh scattering
FWHM	Full width at half maximum
GGI	General grid interfaces
GT	Gas turbine
HCF	High cycle fatigue
HFD	High frequency dynamics
HP	Hole pattern
IFD	Intermediate frequency dynamics
II	Image intensifier
IRO	Intensified relay optics

L2F	Laser-2-focus
LDA	Laser Doppler anemometry
LDV	Laser Doppler velocimetry
LES	Large eddy simulation
LFD	Low frequency dynamics
LIF	Laser-induced fluorescence
LII	Laser-induced incandescence
NBO	No burner outlet (burner without CBO)
MFC	Mass flow controller
PDA	Phase Doppler anemometry
PDV	Phase Doppler velocimetry
P&ID	Piping and instrumentation diagram
PIV	Particle image velocimetry
PMP	Premixed pilot
PZT	Primary zone temperature
RANS	Reynolds-averaged Navier-Stokes equations
RMS	Root mean square
REMPI	Resonance-enhanced multiphoton ionisation
SFI	Swirler fuel injection
SNR	Signal-to-noise ratio
STD	Standard deviation
TDLAS	Tuneable diode laser absorption spectroscopy
TTL	Transistor-transistor logic
ULN	Ultra-low NO_x
UPP	Uniform perforated plate
UV	Ultraviolet

1 Introduction

1.1 Prospects and Challenges for Gas Turbine Combustion

The worldwide demand for electricity has been growing continuously within the last decades. For example, the electricity generated in the European Union (EU) grew by more than 200 GW between 2000 and 2010, which equates an increase of 36% [129]. Within this period, the largest absolute growth in installed capacity was recorded for natural-gas-fuelled power plants, whereas the share of nuclear power plants and plants fuelled with coal or fuel oil even decreased (see Figure 1.1).

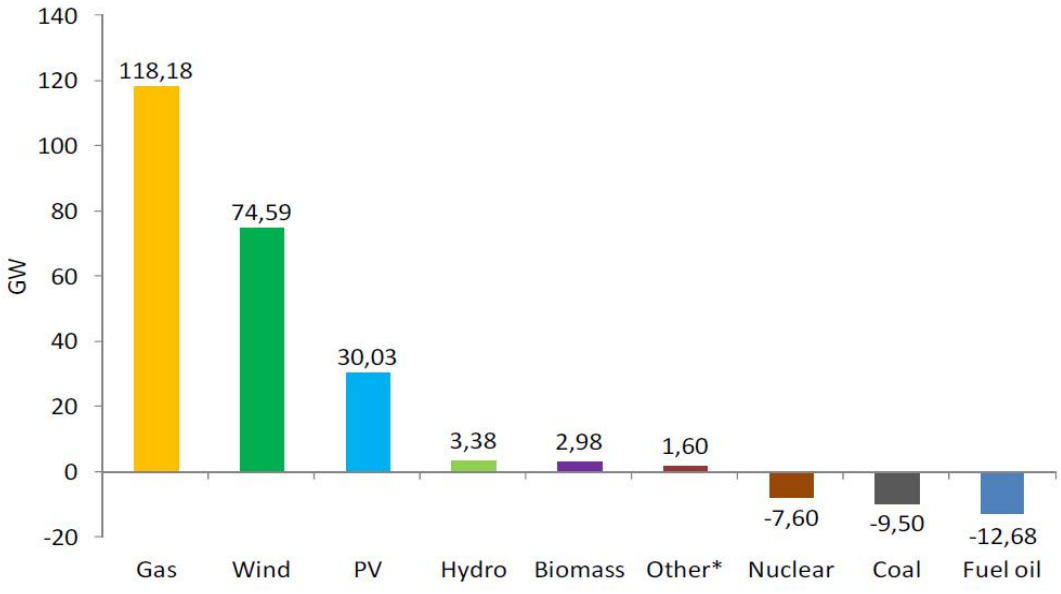

* includes geothermal, waste and heat.
Note: PV = photovoltaic.

Figure 1.1: EU trend in installed electricity generation per fuel or primary energy, 2000 – 2010 [129]

But moreover, another decisive trend can be taken from Figure 1.1: The on-going change of the energy market towards an increasing share of renewable energies, especially wind power and photovoltaic. This also brings new challenges to the energy supply business; because the availability of sufficient wind speeds for wind power or solar radiation for photovoltaic does not correlate with the current demand for electricity. To prevent an increasing risk of insecurity in terms of energy supply, it is indisputable that the resulting gap between electricity demand and electricity produced by the renewables will at least to a great extent need to be filled by conventional power plants [75]. Unfortunately, the predictability of local wind speeds or solar radiation is limited so that operational flexibility in terms of start-up time and costs, ramping rates and turndown capability will become significantly more important for these conventional power plants. Thanks to their superior performance in this area, natural-gas-fired stationary gas turbines (GTs) are expected to play an even more important role in future power generation [129].

This implies that today one of the main development targets for gas turbines is to increase the operational flexibility – in addition to the basic requirements of increased efficiency, reduced emissions, high reliability, and low costs. Figure 1.2 qualitatively illustrates the emission of carbon monoxide (CO) and nitrogen oxides (NO_x), the main pollutants of a typical stationary GT, versus the flame temperature. Since the flame temperature strongly correlates with the engine load the *x*-axis can also be interpreted as indicator for the loading operation range.

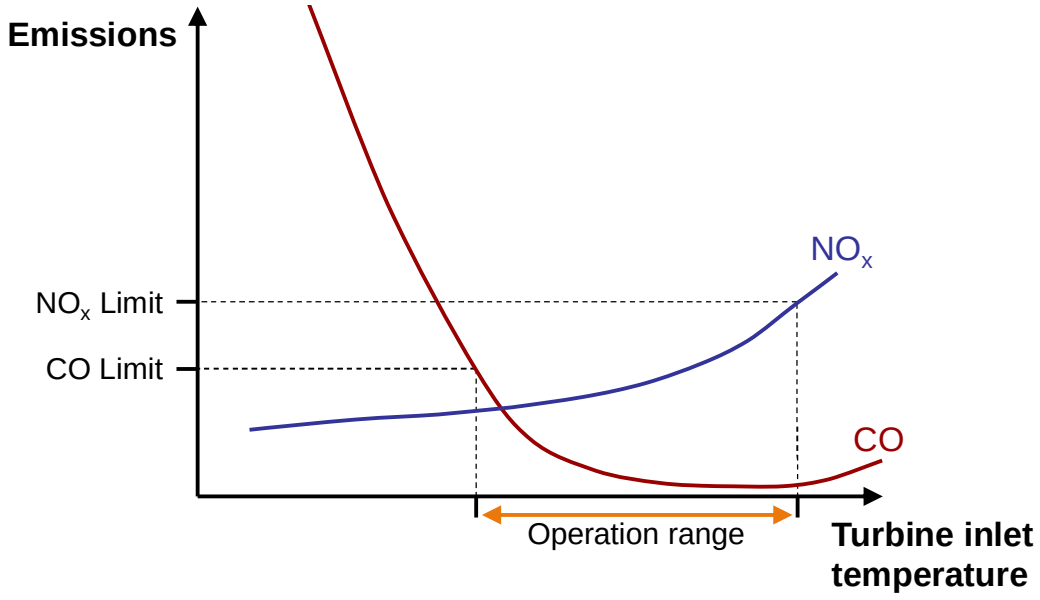

Figure 1.2: Operation range of a typical stationary gas turbine within the allowed CO and NO_x emission limit values

As can be seen, the turn-down capability of the turbine is limited by the increased production of CO at low firing temperatures. The upper end of the operation range is marked by reaching the NO_x emissions limit value. As these emissions are produced during combustion, a key to increase the range of operation is to improve the gas turbine combustion system [62]. For example, the production of NO_x is a strong function of the flame temperature and the residence time in the high-temperature regions [138]. Thus, one way to reduce NO_x emissions is to reduce the cooling air consumption of the combustor or turbine which results in an increased air mass flow participating in combustion and, hence, in a reduced flame temperature level (assuming the fuel mass flow remains unchanged). As the saving of cooling air has practical limits, a second established way to reduce NO_x emissions is to avoid regions with high local flame temperatures resulting from fuel-rich zones. Hence, modern gas turbines are typically equipped with premixed combustion systems operated at lean and nearly uniform premixed fuel/air conditions to reduce the peak flame temperature. In parallel, to reduce the residence time in high-temperature regions, modern low-NO_x combustors have a very compact combustor design leading to a highly turbulent flow and high power densities. As an example, Figure 1.3 shows the evolution of Siemens gas turbine combustors from the early 1970s till today.

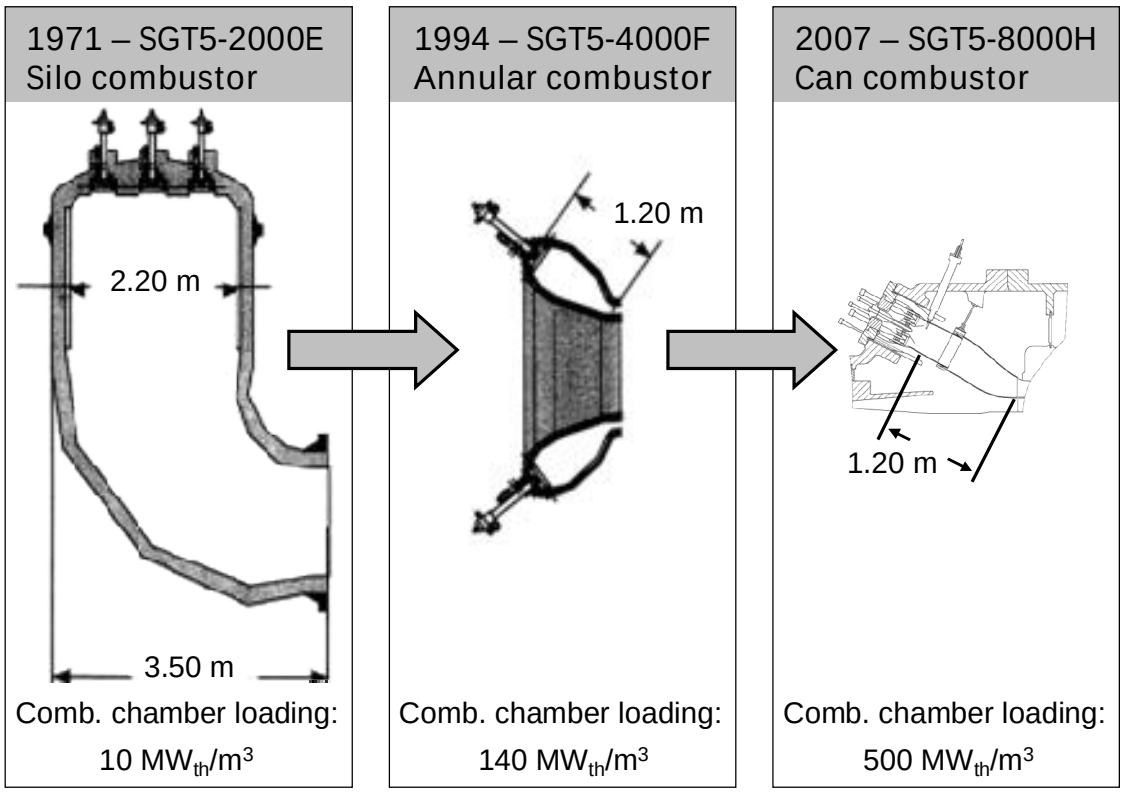

Figure 1.3: GT combustor development from silo to annular and can type

The SGT5-2000E was equipped with two big silo-type combustors with a moderate thermal loading of approximately 10 MW/m^3. In the middle of the 1990s the SGT5-4000F engine with an annular combustion chamber and 24 burners was introduced. This combustor design is already much more compact compared to the silo combustor and leads to a thermal loading of approximately 140 MW/m^3. However, the latest evolution step is marked by the introduction of the SGT5-8000H in 2007. This engine is equipped with 16 can-annular combustors and has a very high thermal loading of approximately 500 MW/m^3 [62].

Unfortunately, combustion systems operated at such highly turbulent and lean premixed conditions are prone to combustion-driven pressure oscillations (CDPO) [33]. Due to the interaction of heat (flame) and sound (pressure oscillation), combustion-driven pressure oscillations are also frequently referred to as thermo-acoustically induced pressure oscillations [108,128]. The effect of unsteady flames or, more general, fluctuating heat sources on acoustics was already described by Lord Rayleigh in 1878 [101]. Almost a century later, in 1971, Putnam published his studies about combustion-driven oscillations in industrial applications [98]. Since then numerous studies focusing on CDPOs in gas turbines were carried out to further understand and control the underlying mechanisms, because the high pressure oscillations increase the risk of flame blow-off and high cycle fatigue (HCF) cracking of combustor parts, bearing distress in the engine rotating assembly, generally cause a reduced lifetime of the associated parts, and often limit emission improvements [33]. It is common sense in many studies that one of the main parameters influencing thermo acoustics in premixed combustion systems are local and temporal fuel/air distribution fluctuations inducing heat-release oscillations [74,76,107,108,128].

Consequently, a better understanding of the interaction of fuel/air mixing and the combustion behaviour in terms of thermo acoustics and emissions is prerequisite for developing advanced gas turbine combustion systems meeting the requirements of the energy supply market.

1.2 Combustion System Validation Strategy

The development of gas turbine combustion system typically follows a defined process. Such processes include a multi-step validation procedure (Figure 1.4) which must be passed by every combustion system, no matter if completely new designed or only slightly changed.

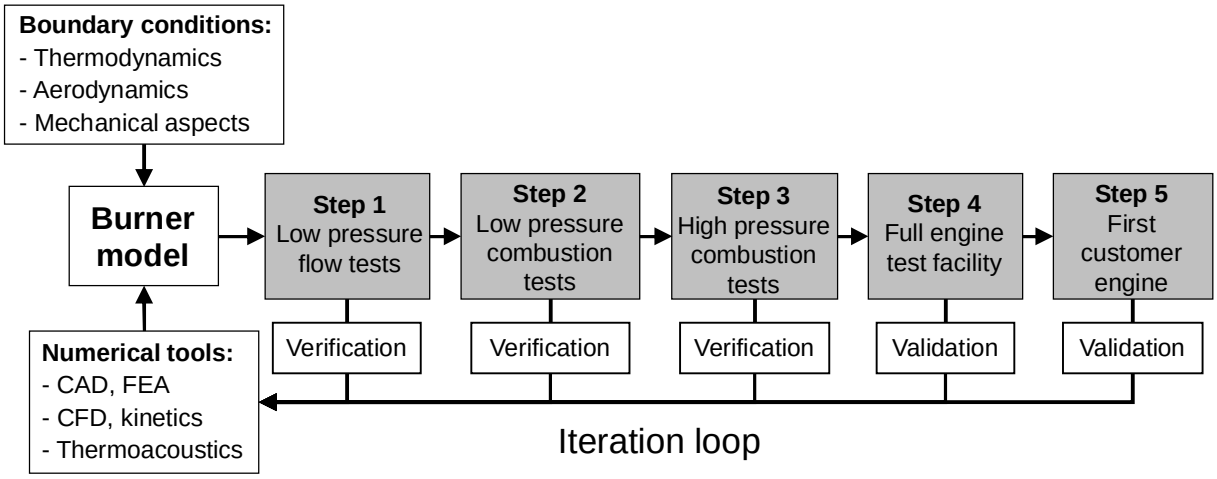

Figure 1.4: Typical industrial gas turbine combustion system validation procedure

As illustrated in Figure 1.4 the validation procedure starts with a new burner version designed with the help of various analytical and numerical tools to meet the defined boundary conditions. The first validation step is the verification of flow characteristics like the air capacity or the fuel/air mixture. These tests are typically done in full-scale single-burner test rigs at atmospheric cold flow conditions. The next step is single-burner combustion testing at atmospheric pressure (step 2) allowing a first evaluation of important features like the ignition behaviour, emissions and the overall combustion performance. Furthermore, the atmospheric combustion test rig can be equipped with windows allowing the detailed investigation of the combustion behaviour with optical measurement techniques. These first two steps are especially valuable to preselect design variants for the subsequent validation steps. Step 3 is the investigation of single burners in combustion tests at increased pressure levels up to full engine pressure. In this step emissions and combustion performance, but also the thermo acoustic behaviour can be investigated under engine-like conditions. Hence, step 3 plays a key role in the validation procedure and is mandatory for each new combustion system before put in an engine. In step 4 a full engine-set of burners is installed in a real gas turbine. These tests are performed in a full-engine test facility, e.g. at the Siemens gas turbine factory site in Berlin, Germany, at the Alstom GT test facility in Birr, Switzerland, at the GE factory test facility in Greenville, USA, or at the MHI demonstration power plant *T-point* in Takasago, Japan. After successful testing, the final hardware design is released for the first engine application at a customer site (step 5). Generally, the complexity of the setup, the validity of the test results, but also the associated costs significantly increase from step to step.

In parallel to the each test the measured data is also used to improve and validate the numerical design tools and to improve the correlation of test rig and real engine results. However, standard test instrumentation typically only delivers information like mass flows, local metal and media temperatures, dynamic and static pressures, and gas composition. This especially limits the detailed validation of complex numerical tools such as 3-D CFD simulations.

1.3 Research Objective

The overall aim of the present thesis is to support the development of next generation gas turbine combustors by improving the experimental tools playing a key role in the combustion system validation process. Today optical measurement techniques are state-of-the-art in a wide range of experiments in flow and combustion science. Examples for widely used techniques in this context are:

- Flow measurements with laser Doppler velocimetry (LDV, also referred to as laser Doppler anemometry, LDA) [127], or particle image velocimetry (PIV) [94,99],
- Species concentration measurements with laser absorption, Rayleigh, and Raman spectroscopy or laser-induced fluorescence (LIF) [32,78,110,114],
- Temperature measurements with coherent anti-Stokes Raman spectroscopy (CARS) [22] or two/multi-line LIF [4,80,125],
- Flame front or heat release rate measurements with LIF [49,50,109,110] or flame chemiluminescence spectroscopy [40,42,47,133].

Many of the mentioned techniques have already been demonstrated in realistic environments. Particularly for applications in internal combustion engines in automotive research a large number of scientific publications is available. In the field of gas turbine related studies many applications of optical measurement techniques are also documented. Relevant works in this context are various LIF measurements by Hoffmann [50], Schildmacher [107], Schneiders [109], Hoeren [49], PIV and DGV measurements by Willert et al. [132], multiple applications of flame chemiluminescence measurements by Güthe et al. [36], Hardalupas et al. [44], and Muruganandam et al. [83], as well as combinations of different techniques by Hubschmid et al. [52], Lückerath et al. [79], and Fischer et al. [26], to name just a few.

However, the application of these scientifically established measurement techniques to industrial large-scale experiments poses particular challenges. The technical realisation of optical access to full-size test rigs operated at gas turbine relevant temperatures and pressures is not trivial, especially if the investigated system should not be affected (e.g., by large water-cooled windows). Furthermore, the sensitive optical setups and the typically complex and sophisticated measurement equipment are not designed for the harsh conditions at industrial laboratories. Hence, most of the aforementioned studies were applied at strongly simplified test rigs or down-scaled burners [26,50,79,108], or even only specific sections of a burner, e.g., a single flow channel, were investigated [49,109,110].

This gap should be closed with the present thesis. In particular, *laser-induced fluorescence* (LIF) with acetone as a tracer for imaging of the fuel/air mixture was established for large-scale applications. Additionally, *flame chemiluminescence imaging* was applied for the advanced evaluation of the flame behaviour during full-scale high-pressure combustion tests with an optical probe to avoid windows. With these newly applied optical diagnostic tools an improved evaluation of full-scale gas turbine combustors was enabled and new insights into the complex processes of mixture formation and combustion behaviour were gained. Hence, this thesis provides a vital step for further developing gas turbine combustion systems. Furthermore, the Siemens combustion system design validation procedure is expected to become more efficient and therefore faster and more cost-effective by increasing the content of information gathered in a single test.

1.4 Thesis Outline

The theoretical background of the applied optical measurement techniques and the selected experimental as well as numerical validation methods is introduced in chapter 2.

Main aspects of the practical realisation of the Tracer-LIF metrology are presented in chapter 3. The general experimental setup and the required supply facilities are described in detail and specific aspects of the experiments performed at combustors from the SGT5-4000F and SGT6-8000H gas turbine frames as well as the related results are presented. Furthermore, results from the SGT5-4000F are compared to results from earlier applied intrusive measurement techniques. In parallel with the optical measurements, selected cases were modelled in

CFD with identical geometric and thermodynamic boundary conditions as in the experiments to establish a common basis for the validation and calibration of the CFD. The comparison of experimental data and simulation are also presented in this chapter.

Chapter 4 deals with the application of chemiluminescence imaging at a full-scale high-pressure combustion test rig. To minimise the impact of the measurement system on the experiment, the optical access to the test rig was designed as a water-cooled endoscope. This optical probe was successfully operated at experimental conditions with an absolute test rig pressure of 9 bar and a flame temperature of approximately 1800 K. After a detailed description of the experimental setup, exemplary test results are presented and discussed. The result discussion is supported by statistical evaluations of various quantities derived from the recorded chemiluminescence images and conventionally measured quantities like emissions and pressure amplitudes.

The thesis is concluded with a summary and outlook for future research in chapter 5.

2 Theoretical Background

2.1 Introduction

The aim of the present study is to support the development of next generation heavy duty gas turbines by improving the experimental evaluation methods for the gas turbine combustion system. Generally, such experiments require test rigs, capable to represent relevant geometry and thermodynamic boundary conditions of a real engine, and measurement techniques to acquire the quantities of interest. In the area of combustion research typically measurements of wall and gas-phase temperatures, species concentrations (e.g. the local fuel/air mixture or exhaust gas composition) and flow properties (e.g. velocity vectors and turbulent fluctuation) are of special interest. Widely used classical measurement approaches for these quantities are thermocouples (temperatures), suction probes (species concentrations), and pitot tubes or hot-wire anemometer (flow velocities). Details for the application of such techniques can be found in the books by Saravanamuttoo [105] and Taylor [123]. However, physical probing can easily perturb the complex heat and species transport in combustion processes and generally is limited in its spatial and temporal resolution [22].

In contrast to classical techniques based on physical probing, optical measurement techniques allow the nonintrusive in-situ investigation of a system. Hence, they have become state-of-the-art in a wide range of laboratory-scale experiments and are indispensable in modern combustion research. Not least due to on-going advances in the development of robust and reasonably priced light sources (particularly lasers) and detectors (e.g. photodiodes and cameras), these techniques have also become attractive for industrial-scale applications such as gas turbine combustors. Therefore, a specific task of the present study was to survey and select optical measurement techniques capable to support the combustion system validation process and to qualify the selected techniques to become standard for the application in the industrial la-

boratories of the Siemens AG Energy Sector. An important part of this qualification was the comparison with data from validated, classical measurement techniques as well as from numerical simulation tools. The principal fundamentals of optical measurement methods and detailed descriptions of the finally selected techniques as well as the applied experimental and numerical validation methods can be found in the following chapters.

2.2 Optical Measurement Techniques

Classical optical measurement approaches are long known and have been used for many decades now. Essential parts of today's knowledge about the inner structure of atoms and molecules were gained with the help of early absorption and emission spectroscopy techniques [17]. Other prominent examples of early optical measurement techniques are interferometry, pyrometry, and schlieren photography [115]. Later, with the commercial introduction of high power-density monochromatic light sources, i.e. lasers, in the 1960s the capabilities of these traditionally employed optical techniques were remarkably enhanced [22]. Moreover, in combination with advances on the detection side (e.g., advanced diffraction gratings, photomultipliers and -diodes, CCD and CMOS detectors for scientific camera systems, and image intensifiers) a wide and still growing number of various new measurement methods could be developed [17].

However, most optical measurement techniques are finally based on the interaction of light[1] and matter. Hence, the explanation of the underlying principles is closely linked to the quantum mechanical description of the inner structure of atoms or molecules. In this view, an atom consists of a nucleus in the centre surrounded by atomic orbitals representing the wave function, i.e. the probability density function, of one or a pair of electrons. The negatively charged electrons are attracted by the positively charged nucleus. Hence, with increasing distance between an electron and the nucleus the average energy of the electrons increases. However, the

[1] In this context light generally means electromagnetic radiation and is not limited to the range of wavelengths that is visible to the human eye ("visible light"). In modern concepts light is also described as photons, representing the elementary particles of the quantized electromagnetic field.

energy difference between the shells can only take discrete values, described by the principal quantum number, and equals integer multiples of $h\nu$, where h is the Planck constant and ν the frequency of a photon. In addition to the different electronic energy levels of an atom, molecules can have different vibrational and rotational energy states, with quantum numbers which can also take zero and positive integer values.

In nature the quantised structure of atoms and small molecules e.g. appears as discrete spectral lines after interaction with a photon. Due to the electron configuration, which is unique for each individual species and thermal state, the distribution of the spectral lines is also species-specific, comparable to a fingerprint. Each spectral line can additionally be assigned to specific electronic, vibrational, and rotational transitions between defined lower and upper energy states. From these dependencies additional information about an investigated species can be derived, as the intensity and shape of spectral lines are depending on pressure, temperature, and the species' velocity (Doppler Effect). Making practical use of these relations is the aim of optical measurement techniques. However, due to superposition of the spectral lines originating from the many different possible energy levels, the spectra become more and more congested with increasing molecular size. Hence, using smaller molecules is preferred for optical diagnostics. Moreover, still today many aspects of the complex interactions of different phenomena in quantum mechanics are not fully understood and are under on-going research. For more information please refer to the books by Atkins [1], Haken and Wolf [41], and Herzberg [45].

Nonetheless, today numerous optical measurement techniques are already commercially available as complete systems and are frequently used in multiple fields of interest. Examples are particle image velocimetry (PIV) [94,99], phase Doppler velocimetry (PDV, also called phase Doppler anemometry, PDA) [56], laser Doppler velocimetry (LDV, also referred to as laser Doppler anemometry, LDA) [127], classical absorption or tuneable diode laser absorption spectroscopy (TDLAS) [20,111], applications of laser-induced fluorescence (LIF) [23,43], and laser-induced incandescence (LII) [61,113]. Further widely used, but not out-of-the-box available techniques are coherent anti-Stokes Raman scattering (CARS) [21,121], different setups based on Rayleigh-, Mie- and spontaneous Raman scattering [22], cavity ring down spectroscopy (CRDS) [137], or resonance-enhanced multiphoton ionisation (REMPI) [135]. Less common techniques are, for example, filtered Rayleigh scattering (FRS) [7], Doppler global velocimetry (DGV) [104,132], laser-2-focus (L2F) [6,48], gaseous image veloci-

metry (GIV) [49], and degenerate four wave mixing (DFWM) [18,100]. Finally, spectrally resolved flame chemiluminescence measurements have again gained increased interest within the last years, mainly due to its comparably simple and robust experimental setup.

Common basic selection criteria for optical measurement techniques are:

- **Measured quantity**
  The different techniques can obviously be classified regarding the quantity to be measured (e.g. temperature, species concentration, velocity, etc.).

- **Qualitative and quantitative techniques**
  Another significant characteristic of a measurement technique is whether the quantity is measured qualitatively, e.g. a relative distribution of a species concentration or temperature, or quantitatively, e.g. absolute species concentration or temperature. Due to the partially highly complex underlying principles and the dependency on many different parameters, the latter requires exact calibration and very well defined experimental boundary conditions.

- **Type of light/matter interaction**
  Optical measurement techniques can be based on different types of light-matter interaction. Simply said, these are basically absorption, emission, and scattering.

- **Active and passive techniques**
  In this context, active means that the application of the measurement technique requires excitation with a light source, i.e. a laser, which is the case for nearly all techniques mentioned above. However, a special role is taken by the passive technique of flame chemiluminescence spectroscopy, as the detected signal originates from electronically excited intermediate species which are produced during the chemical reaction in the flame.

- **Spatial resolution**
  Normally the probing volume is a small, almost spherical probe volume, a 2-D plane, or the data is integrated along a line-of-sight. Examples for the first category are LDV, PDV, CARS, or L2F. A common approach to extent the investigated probe region with these techniques is to mount the laser and detection system on a traversing device for scanning an area of interest. Prominent examples for the second category (2-D

plane) are LIF, PIV, and Rayleigh-scattering. Here the measurement plane is usually defined by a laser light sheet. If the detector is a camera and the measurement result is an image the technique is called imaging technique. Some specific arrangements like Stereo-/tomographic PIV or DGV also allow acquiring 3-D information in a plane. Typical line-of-sight techniques are absorption spectroscopy or flame chemiluminescence measurements. The latter is also frequently applied as imaging method.

- **Temporal resolution**
  On the one hand, the introduction of pulsed lasers enabled experimental setups with extremely short investigation cycles (today down to the range of femtoseconds), capable to temporally "freeze" even very fast processes. On the other hand, the possible sampling frequency greatly increased up to several 100 kHz within the last years allowing real high-speed measurements.

A vast overview of laser diagnostics and spectroscopy techniques and the underlying principals is given in the books by Demtröder [17] and Eckbreth [22]. For a detailed discussion of optical measurement techniques with respect to specific applications please refer to the publications by Wolfrum [135], Kohse-Höinghaus et al. [63,64], or Schulz et al. [112], for example.

Based on an analysis of the Siemens combustion system validation procedure (cf. chapter 1.2) it was decided to implement appropriate optical measurement techniques for the investigation of the fuel/air mixing performance of full-scale GT combustors at atmospheric cold flow conditions (Step 1 in Figure 1.4) and for the improved evaluation of the combustion behaviour of full-scale GT combustors under realistic boundary conditions (Step 3 in Figure 1.4). Hence, a detailed survey of the aforementioned optical measurement techniques and the relevant literature was performed. As the large scale of the investigated systems, the harsh experimental boundary conditions, and the high reliability and reproducibility required by the Siemens validation procedure already present a high hurdle it was decided to prefer mature and proven techniques. With view on the high-pressure combustion tests another key requirement for the selected technique was to minimise the potential impact on the experiment itself (e.g. by avoiding large windows). Following these specifications two techniques were selected for the application in this study: laser-induced fluorescence (LIF) and flame chemiluminescence imaging. The application of the LIF technique was realised with acetone to tracer the fuel flow

in a 2-D imaging setup. For flame chemiluminescence imaging the required optical access to the high-pressure combustion test rig was provided by a specially designed water-cooled endoscope. A detailed introduction to the two selected techniques and the challenges that were associated with their application to Siemens gas turbine combustors is given in the following chapters.

2.2.1 Acetone Laser-Induced Fluorescence for Fuel/Air Mixture Imaging

The underlying physical principles of laser-induced fluorescence (LIF) are the absorption of a photon (i.e. from the laser) and the subsequent emission of a photon. When the photon is emitted on short time scales this emission is called fluorescence. On much longer time scales when metastable electronic states are involved the photon emission is called phosphorescence. Beside the spontaneous emission of a photon the excited species can also return to the equilibrium by transferring the excess of energy through non-radiative decay processes, i.e. collisional quenching, internal conversion (IC) or intersystem crossing (ISC). Figure 2.1 shows the absorption and possible deactivation processes of a typical organic molecule.

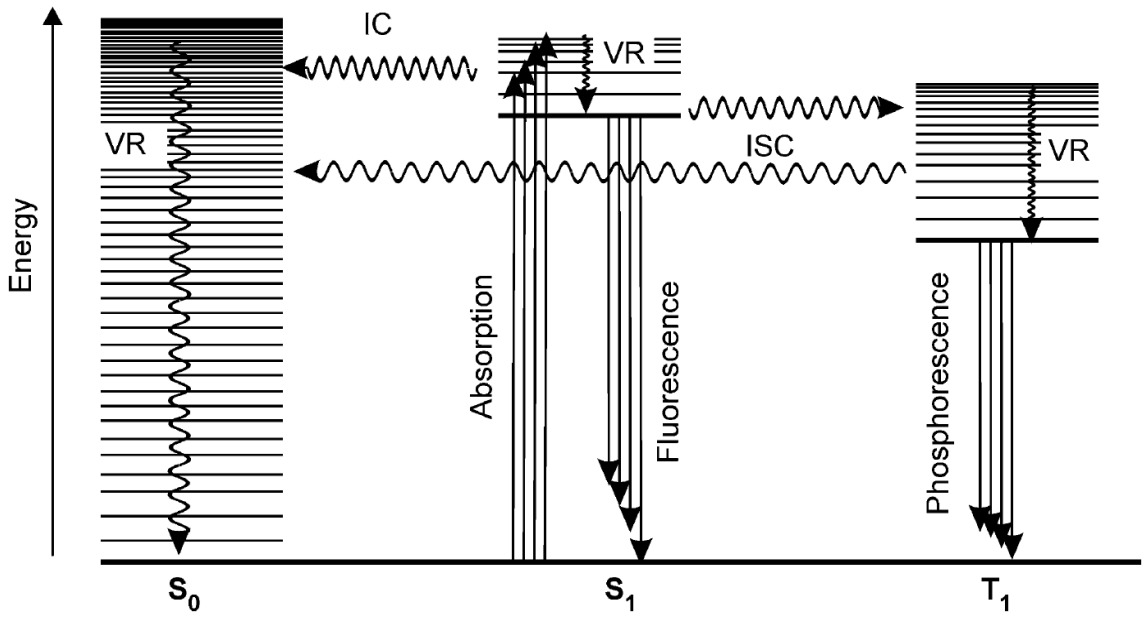

Figure 2.1: Jablonski diagram with photo physical processes of organic molecules during excitation and deactivation [114]

A common approach utilising laser-induced fluorescence for non-intrusive measurements of species concentration or temperature is illustrated in Figure 2.2. Light from a pulsed laser

with high peak power is guided through the system of interest. Most commonly, the laser light is formed into a thin planar sheet defining the investigated probe volume. The laser-induced fluorescence is typically captured by a CCD camera oriented perpendicularly to the laser sheet. The cameras are often combined with image intensifiers to enhance the recorded signal levels or to allow short exposure times to suppress background luminosity.

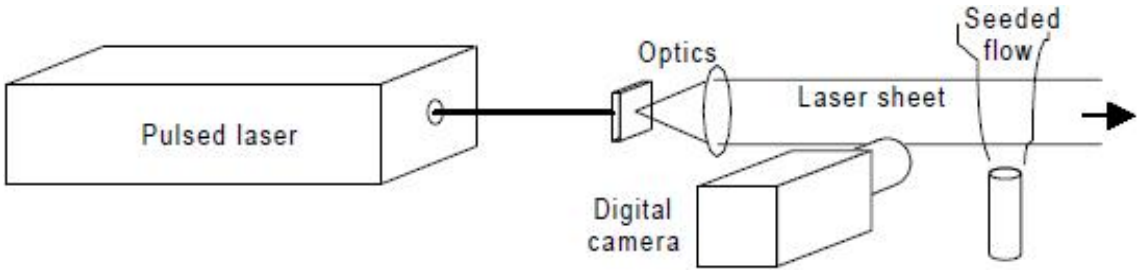

Figure 2.2: Typical setup for laser-induced fluorescence imaging diagnostics [124]

First applications of LIF were already presented in 1977 by Epstein [23]. Since then LIF has been demonstrated in a wide range of reacting and non-reacting systems. In the field of heavy-duty gas turbine combustor development, for example, LIF was utilised by Krämer et al. [68] and Düsing et al. [19].

For the investigation of flows that do not contain fluorescent species the flow can be "marked" by adding a so-called tracer. A tracer is a fluorescent species with well-known photo-physical properties, i.e. the LIF signal intensities should be directly proportional to the desired quantity and should not be influenced by ambient conditions. Furthermore, for the application to Siemens GT combustors the following requirements were specified:

- A high vapour pressure at low temperatures to allow straightforward seeding at high levels
- An absorption spectrum accessible with standard high-pulse-energy lasers
- High fluorescence signal levels to achieve a satisfying signal-to-noise ratio (SNR)
- Insensitivity to effects of collisional quenching, esp. oxygen
- Compatibility with air
- Low toxicity
- Low costs for seeding at high flow rates

After a detailed survey of frequently used tracers finally acetone (CH_3-CO-CH_3) was identified as optimal tracer for the present study. In this context the comprehensive overview of suitable tracers for LIF diagnostics by Schulz and Sick [114] and the included guideline for selection was extremely helpful.

The investigation of acetone as tracer for LIF goes back to the initial work of Lozano et al. [78]. The respective absorption spectrum for excitation from the ground state S_0 to the first excited singlet state S_1 measured by Lozano is shown in Figure 2.3. It can be seen that acetone is well accessible at wavelengths of commonly used lasers (KrF excimer laser at 248 nm (a), Nd:YAG laser at 266 nm (b) and XeCl excimer laser at 308 nm (c), see [79]).

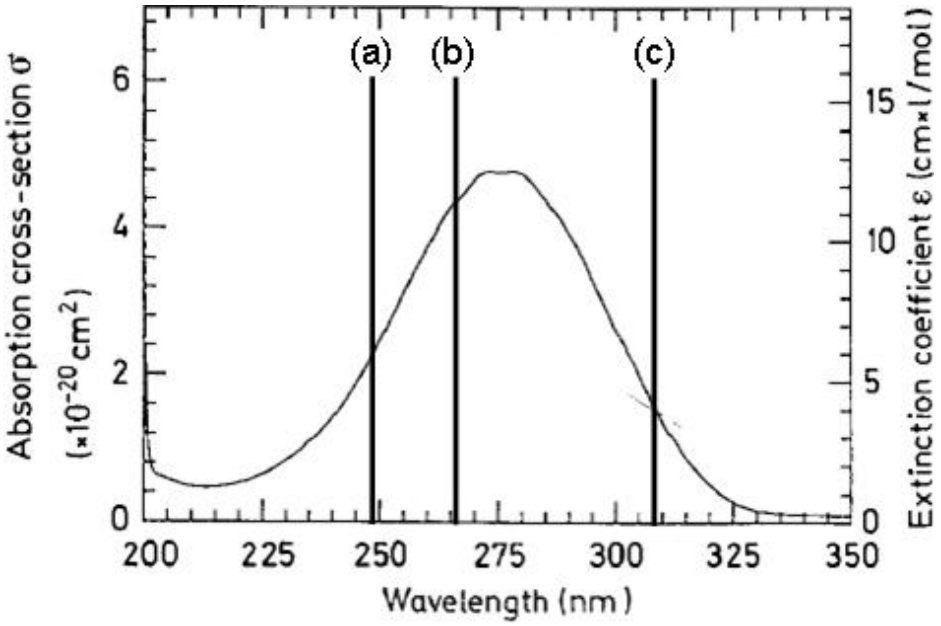

Figure 2.3: Acetone absorption spectrum corresponding to excitation from the ground state S_0 to the first excited singlet S_1 [78]

Fluorescence spectra after excitation at 248 and 308 nm are shown in Figure 2.4. It can be seen that the spectrum is shifted to longer wavelengths compared to the absorption spectrum and the excitation wavelengths. This allows the installation of optical filters in front of a camera lens suppressing stray light from the high power laser.

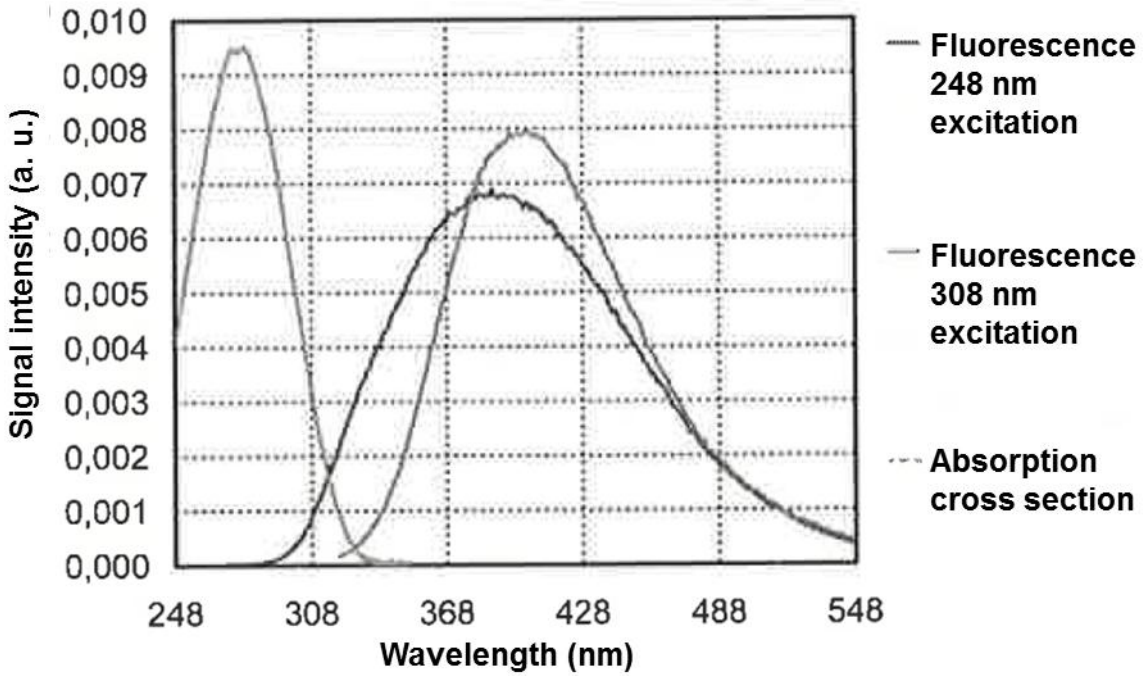

Figure 2.4: Acetone absorption cross section and fluorescence spectra when excited at 248 and 308 nm. The signal intensities are not proportional to each other [77]

A relevant feature for straightforward interpretation of LIF-signals is a linear correlation of the tracer concentration and the fluorescence intensity. As can be seen in Figure 2.5 this requirement is fulfilled for acetone.

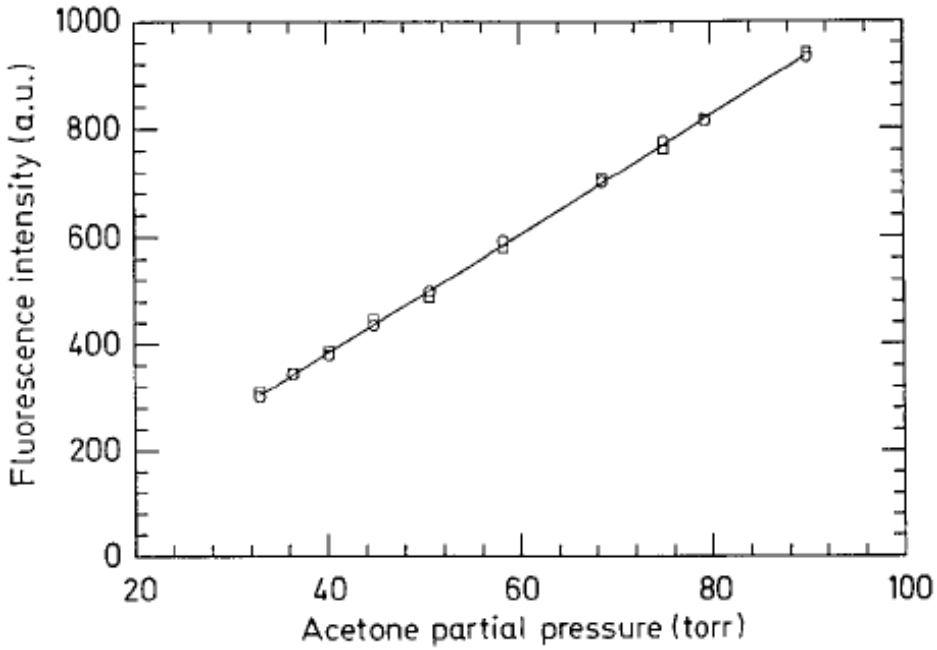

Figure 2.5: Linearity of the acetone laser-induced fluorescence with respect to acetone partial pressure [78]

Furthermore, the LIF signal should ideally be proportional to the laser energy. The linear dependence of the acetone fluorescence with laser energy for three relevant wavelengths is shown in Figure 2.6.

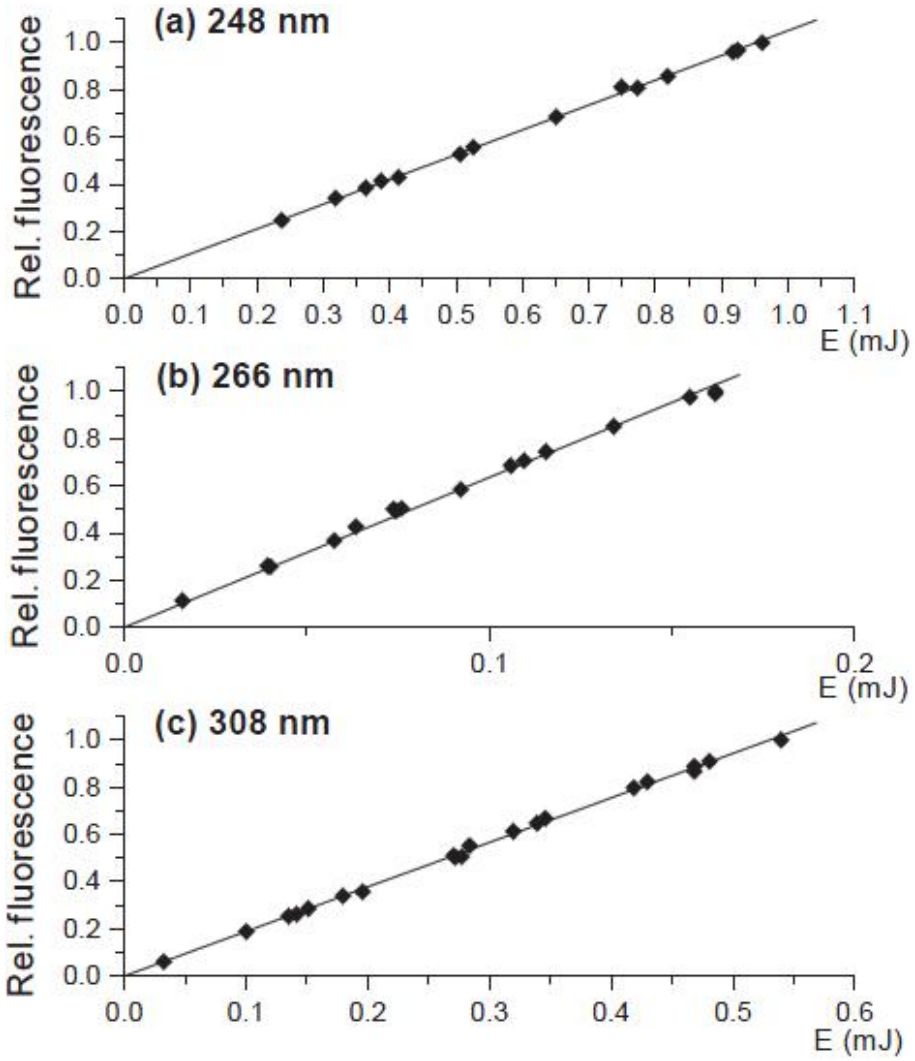

Figure 2.6: Linearity of fluorescence with energy for three excitation wave wavelengths 248 nm (a), 266 nm (b), 308 nm (c). Each data point is the average of 400 fluorescence pulses from a fixed pressure of acetone [126]

However, the fluorescence signals from nearly all known tracers show at least some dependence on local temperature, pressure, and bath gas variation. For acetone these dependencies were thoroughly studied by Thurber in [124] and [126] and were recently expanded by Löffler [77]. The respective data for pressure, temperature and presence of oxygen is shown in Figure 2.7 and Figure 2.8.

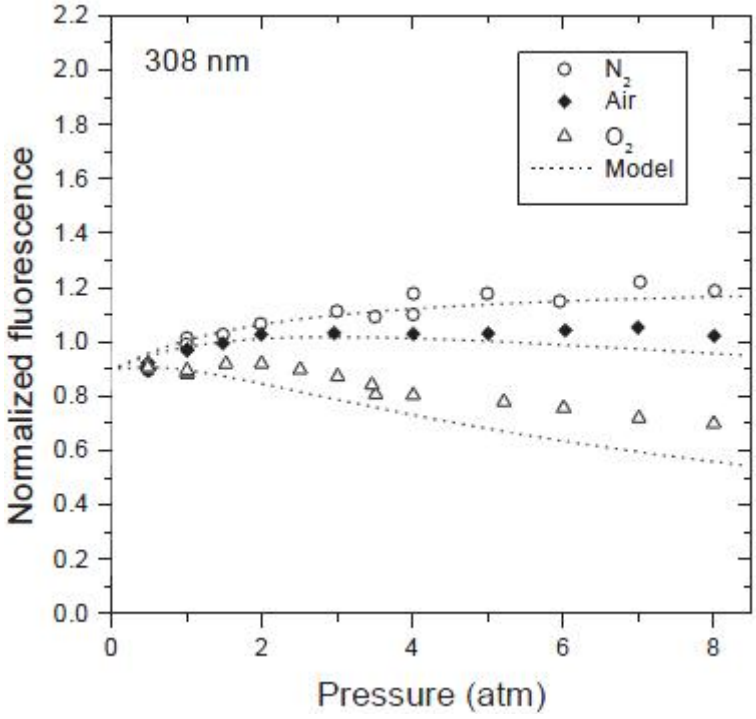

Figure 2.7: Pressure dependence and examination of the effect of O_2 addition on the fluorescence per acetone molecule for 308-nm excitation. Symbols represent data points, and the dotted lines are results from a fluorescence yield model calculation. The data are normalized to unity at atmospheric pressure [126]

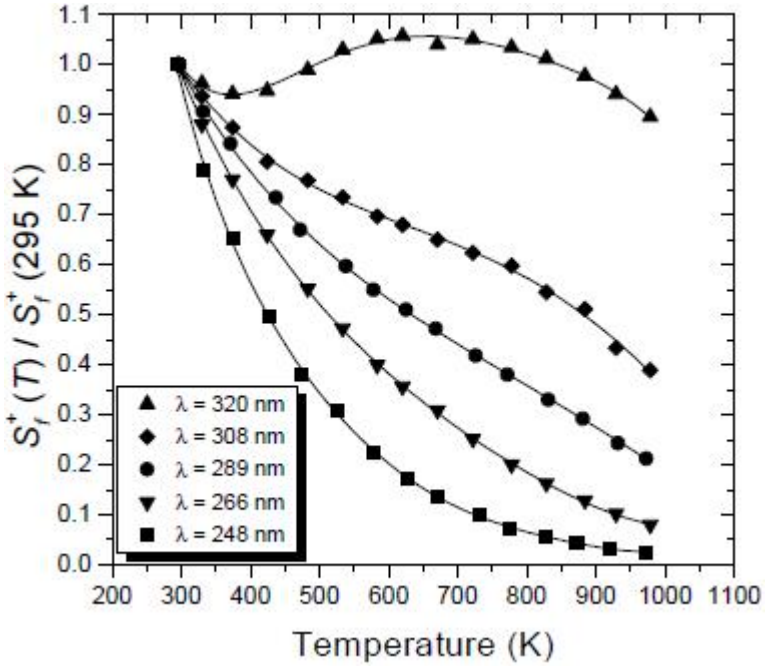

Figure 2.8: Temperature dependence of fluorescence per unit laser energy per unit mole fraction at atmospheric pressure, normalized to the value at room temperature [124]

2.2.2 Flame Chemiluminescence Imaging in Combustion Processes

Broadly speaking, chemiluminescence is the emission of light from electronically excited species[2] produced in a chemical reaction. A prominent example is combustion where several reactions are involved forming excited species as intermediates. Figure 2.9 shows the main carbon reaction pathways for premixed combustion of methane in air as published by Najm et al. [84]. The dominant reaction path is indicated by blue arrows and the electronically excited intermediates are circled in red. The dashed lines indicate that the excited species OH*, CH*, and CO_2* are only produced in side paths with low integrated production rates below 10^{-6} moles/cm^{2}s [84]. Nonetheless, the chemiluminescence emitted from premixed flames is high enough to be visible for a human eye. For example, the characteristic blue colour of a premixed methane/air flame is mainly caused by the CH* and C_2* band emission.

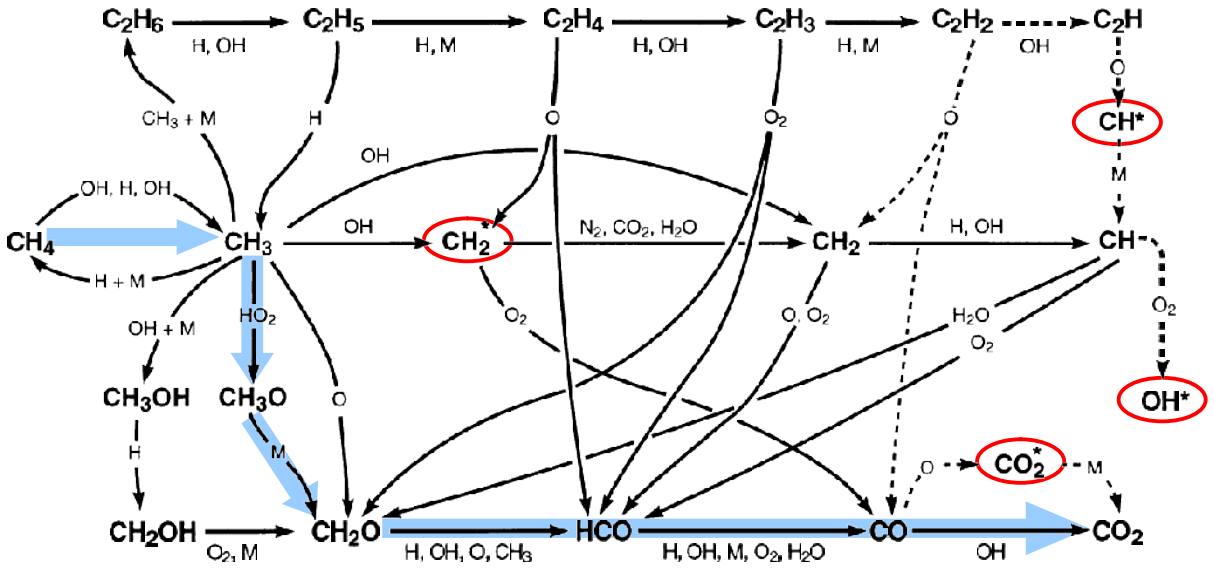

Figure 2.9: Simplified reaction pathway of a premixed methane/air flame with main reaction pathway (blue) and relevant excited species produced in side paths [84]

[2] Throughout this thesis the electronically excited species will be indicated by an asterisk (*). E.g., OH* denotes the electronically excited variant of an OH radical.

Figure 2.10 shows a representative chemiluminescence spectrum of a turbulent methane/air flame recorded by Lauer [72] at atmospheric pressure. The spectral resolution of the spectrometer was 1 nm. One can clearly distinguish the emission bands from the most important species OH* (two peaks from 270 to 325 nm), CH* (main peak around 430 nm), and C_2* (three peaks between 430 and 520 nm). As can be seen, the whole spectrum is superimposed by CO_2* broad-band emission from approximately 270 to 550 nm.

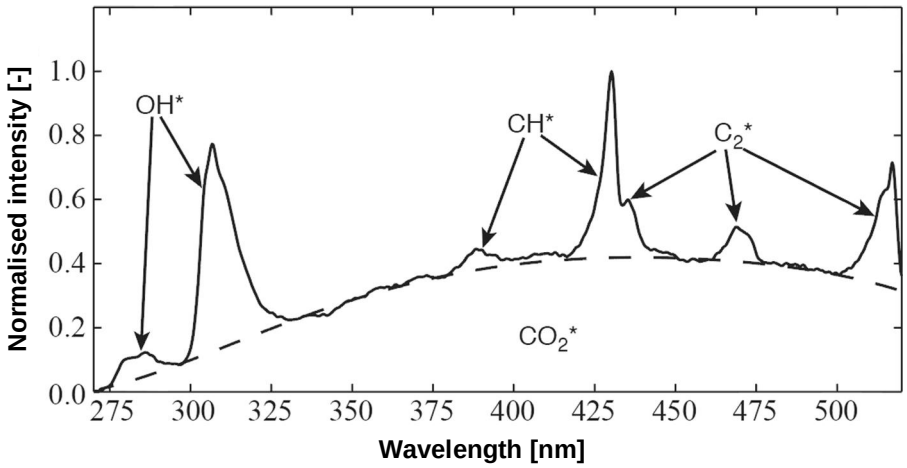

Figure 2.10: Representative chemiluminescence spectrum of a turbulent methane/air flame at atmospheric pressure [72]

In fact, spectroscopic investigations of the flame chemiluminescence for combustion research were already established in the first half of the 20th century. Here especially the comprehensive studies of atmospheric and lower pressure flames with different fuels and stoichiometry from Gaydon [27] and Gaydon and Wolfhard [28,29] are worth mentioning. Around the same time, Clark [13] and Clark and Bittker [14] published first investigations of the correlation of chemiluminescence and integral heat release rate of laminar and turbulent flames at different fuel flow rates and equivalence ratios. Basically, they already found decreasing chemiluminescence intensities for both decreasing equivalence ratio and decreasing fuel flow rate at constant equivalence ratios. For Reynolds numbers up to 6,000 no impact of the turbulence on the chemiluminescence spectra was observed. However, the measured chemiluminescence intensities for higher Reynolds numbers up to 18,000 were lower than predicted by linear extrapolation of the measured data from the lower Reynolds-number range.

Since these early studies chemiluminescence measurements have become an important diagnostic tool in both fundamental and applied research [11]. Fundamental research especially

benefited from the increased availability of instruments with high spectral resolution (i.e., spectrometers and camera detector systems) enabling the observation of chemiluminescence spectra with resolved rotational lines [10]. In parallel the elementary reactions of important chemiluminescent species were investigated in kinetic studies [8,57,67]. Additionally, the dependence of chemiluminescence spectra on temperature, pressure [46,47], fuel composition [86,97], stoichiometry [65,66], and turbulence as well as the correlation of certain species with heat release [102,103] was the topic of multiple studies. These data also served as basis for the development of spectral simulation tools. A widely used spectral simulation program and database in this context is *LIFBASE* [81]. The progress in fundamental research also triggered chemiluminescence measurements in the field of technical applications. Here experimental investigations especially focus on measurements of the reaction zone [26,133], integral heat release rate [72], and stoichiometry as well as on thermo acoustic evaluations [37,52,71]. This is often accompanied by chemiluminescence modelling for a variety of purposes like determination of heat release rate correlations [59], equivalence ratio evaluations [90], or general combustion diagnostics [58,88,130]. A comprehensive summary of different chemiluminescence applications with respect to heavy-duty gas turbine combustors is given in the recent publication by Güthe et al. [36]. Moreover, the comparably simple, cheap and reliable setup for chemiluminescence measurements has recently led to a number of applications for control purposes in technical combustion systems, especially gas turbines [44,83,85] and industrial furnaces [89,122].

The aforementioned examples show the diverseness of flame chemiluminescence measurements with the accompanying variation of experimental realisations. Common setups include spectrometers and cameras for spectrum measurements, photomultipliers and photo diodes measuring the spectrally integrated chemiluminescence signal, typically combined with an optical band-pass filter, or imaging methods with one or more intensified UV-sensitive camera(s) with optical band-pass filter(s).

Generally, deducing qualitative information about the flame behaviour from chemiluminescence measurements is relatively straightforward. However, quantitative measurements require significantly higher effort and have to be taken with care. On the one hand, special challenges arise from the line-of-sight nature of chemiluminescence measurements leading to a general loss of spatial information and, depending on the chosen detector setup, a significant reduction of the OH* signal in the range of 308 nm due to absorption by OH [10]. On the oth-

er hand, turbulence, flame strain and wrinkling strongly affect the local heat release distribution limiting the interpretation of the spatial chemiluminescence information, in particular for imaging setups. Consequently, the feasibility of chemiluminescence measurements for scientific combustion diagnostics has frequently been scrutinised and is still topic of on-going research. Critical reviews of the aforementioned aspects and the resultant limitations for practical application purposes e.g. can be found in the works of Najm et al. [84], Haber [39], Nori and Seitzman [87], Lauer [72] and Lauer and Sattelmayer [73]. Depending on the experimental setup, additional image distortion may arise from beam steering as a consequence of refractive index variations due to the inhomogeneous distribution of temperature and chemical composition in the investigated volume. This effect was investigated by Ertem et al. [24] using large eddy simulations in combination with a ray tracing model.

2.3 Applied Validation Methods

The results from the fuel/air mixing measurements with 2-D tracer LIF will be compared with results from the method that was previously used within the Siemens GT combustion system validation process. This method uses a rake of suction probes mounted on a rotatable lance in the centre of the burner to be investigated. The underlying principles and the experimental setup of this classical intrusive probing technique will be introduced in chapter 2.3.1.

Currently steady RANS CFD is still the standard method for fuel/air mixture simulations at the Siemens Energy Sector. However, the LIF-measurements will be used as reference data to evaluate the feasibility and limitations of the RANS CFD approach. The basic fundamentals of this approach will be introduced in chapter 2.3.2.

The chemiluminescence images will also be used for comparison to CFD simulations. For this purpose, OH* and CH* reaction mechanisms were implemented in the CFD code and a specific post-processing tool generating line-of-sight images from the CFD simulations was developed. This tool and the used modelling approach for turbulent premixed combustion will also be introduced in chapter 2.3.2.

2.3.1 Experimental Methods

The fuel/air mixing measurements within the Siemens GT burner validation procedure were previously done using a suction probe rake mounted on a rotatable lance. This lance can be installed in the centre of the pilot burner.

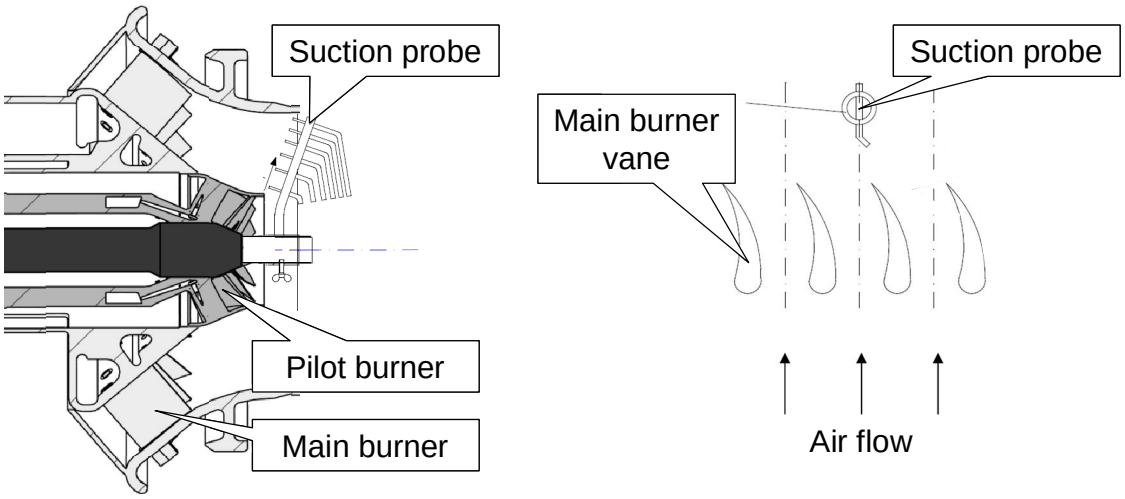

Figure 2.11: Experimental arrangement for suction probe measurements

Figure 2.11 shows the experimental setup for the suction probe measurements. On the left hand side one can see the cross-section of a GT burner with the installed suction probe rake. The principal sketch on the right hand side shows the arrangement of the suction probe relative to the main burner flow path. It can be seen that the combustor air enters the main burner and is swirled by the vanes. The fuel is typically injected through holes integrated in the burner vanes. The suction probe is located downstream of the vanes and measures the swirled fuel/air mixture. The angle of the single suction probe tubes relative to the burner axis and the mass flow of the suction probes are adjusted to meet isokinetic probing conditions, i.e. the angle and velocity matches the flow conditions at the measurement plane.

The suction probe measurements are done at atmospheric cold flow conditions in a full-scale single-burner test rig (see Figure 2.12). For testing air is sucked through the rig using a liquid ring pump located far downstream of the test rig outlet. The fuel is replaced by compressed air doped with a known concentration of propane (typically in the range of 150 ppm). With the suction probes the propane/air mixture is extracted out of the test rig and led to a set of flame ionisation detectors (FID). The FIDs measure the individual propane concentration of every suction probe tube so that the local fuel/air mixture can be calculated. However, due to

the distance between suction probe and the FIDs, one has to wait for 30 s till a measured mixture arrives at the FID. Then, the propane concentration is measured for 20 s and averaged afterwards.

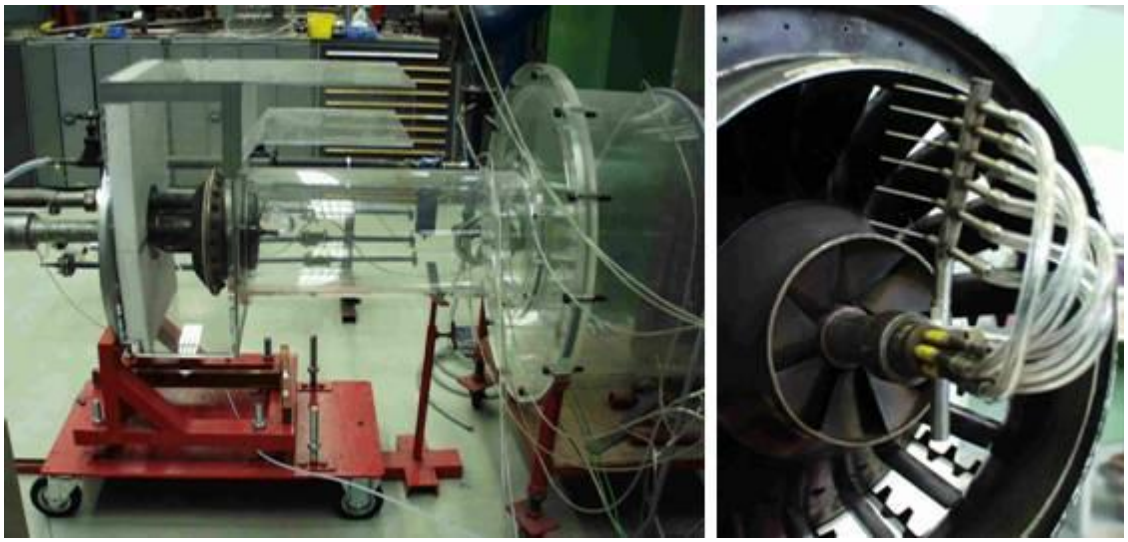

Figure 2.12: Pictures of the test rig (left) and the suction probe rake mounted to a burner (right)

To increase the spatial fuel concentration information, two different probing rakes with 6 tubes each can be used sequentially, resulting in a total number of 12 radial tube positions. These positions are chosen in a way that the total area of the investigated burner exit plane is divided into 12 planes of the same area. With each probing rake the lance is rotated in steps of 3° from 0° to 180° and in steps of 6° from 186° to 354°. This results in 90 different circumferential probe positions and a total number of 1080 measurement points covering the complete main burner outlet. However, a finer spatial resolution is principally possible with the current setup, but is typically not realised due to time reasons.

Typical results from a suction probe measurement are shown in Figure 2.13. The results are normalised to a mean value of 1. The left hand side shows the relative fuel concentration for 6 different radial positions over the circumferential position. It can be seen that the concentration strongly fluctuates around the mean value. This is mainly caused by the single vanes of the main burner. The right hand side shows a 2-D contour plot of the relative fuel concentration. Here one can also identify the same trends as in the concentration profile. Moreover, the contour plots are especially useful to quickly identify regions with worse fuel/air mixture.

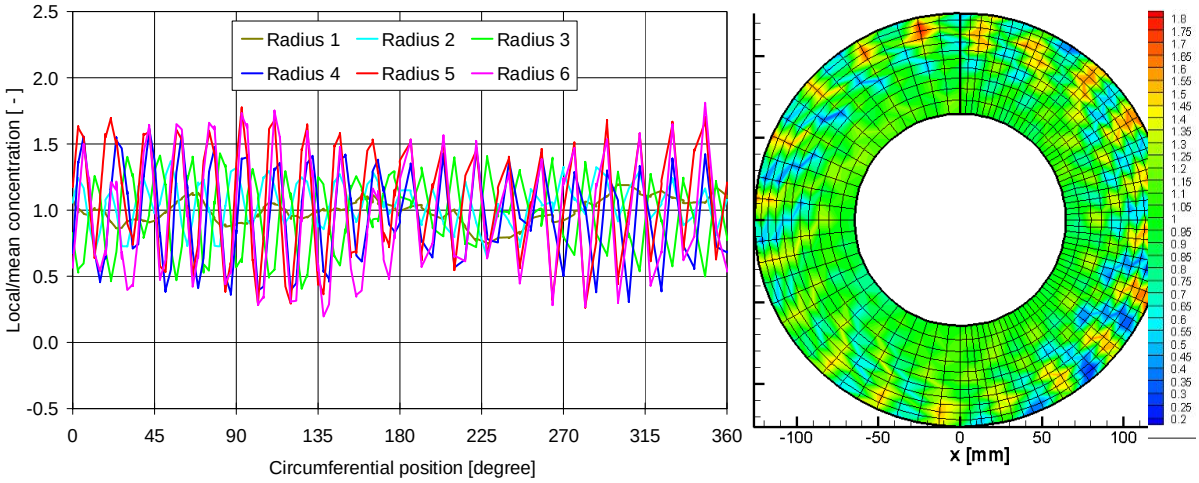

Figure 2.13: Typical results from a suction probe measurement. Left hand side: Relative fuel concentration for each radial position over the circumferential position. Right hand side: 2-D contour plot of the relative fuel concentration.

Additional information such as the circumferentially or radially averaged fuel distribution or the standard deviation between the different circumferential or radial probe positions is used for the evaluation and can be calculated from the suction probe data. Figure 2.14 shows a typical circumferentially averaged radial fuel concentration profile as well as the circumferential standard deviation of the relative fuel concentration plotted over the relative channel height of the main burner. From past experience it is known that especially the radial fuel distribution has a significant impact on the thermo-acoustic behaviour of the burner.

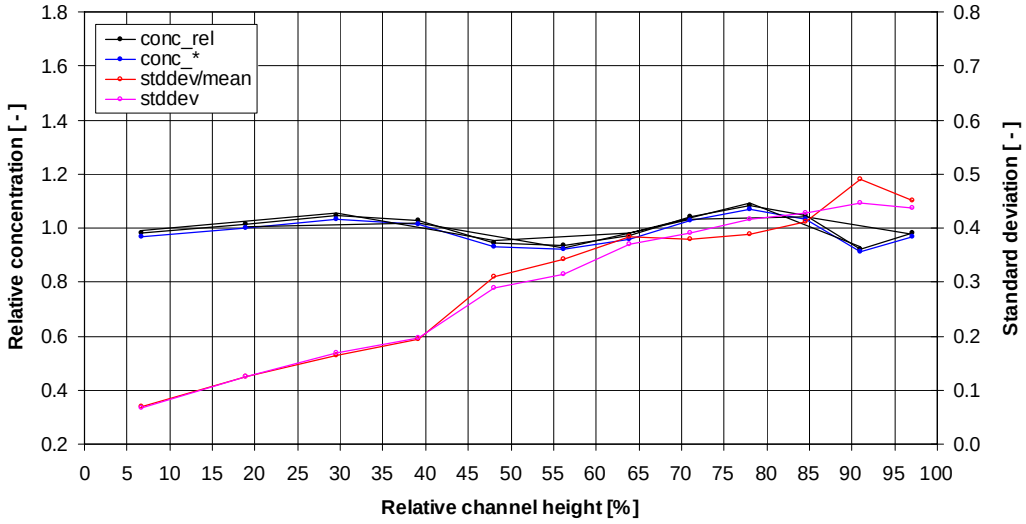

Figure 2.14: Typical radial concentration profile and standard deviation plotted over the main burner flow channel height

Advantages of the suction probe measurements are the robust and comparably simple experimental setup, the good reproducibly and repeatability of the measurements, and the long experience with this technique at the Siemens flow lab. However, major limitations of the suction probe method are the missing information about temporal fluctuations of the fuel/air mixture, the flow disturbing probe, the comparably long time required for a measurement, and the restriction that to date only the main burner of the Hybrid burner can be investigated. Furthermore, previous comparisons of suction probe measurement results and numerical mixing simulations did not show a good agreement, so that the accuracy of both the experiment and the simulation were frequently questioned. The LIF experiments in this study should help to overcome some of these limitations and to improve the agreement of experiment and simulation.

2.3.2 Numerical Methods

Numerical methods predicting turbulent flow and/or combustion properties are playing an increasingly important role in the development of combustion systems. One of the main tasks in this context is solving the Navier-Stokes equations with the help of computational fluid dynamics (CFD). The basic procedure for CFD is the definition of the physical domain of the problem by a CAD model, the discretisation of the domain volume into cells (*meshing*), the definition of the fluid properties at the inlet and outlet of the model boundaries, and, if necessary, the initial starting conditions. Then the simulation is started and the equations are solved iteratively. In CFD generally three levels of computation may be distinguished:

- **Direct numerical simulations (DNS**) "simply" solve the Navier-Stokes equations. In this approach all turbulence scales down to the Kolmogorov scale are resolved. This naturally requires a correspondingly high grid and time resolution resulting in a very high computational effort. Hence, DNS is currently limited to academic problems.

- In **large-eddy simulations (LES)** a filtered version of the Navier-Stokes equations is solved. With this approach only the large turbulent scales are resolved whereas smaller scales are modelled. This results in a less demanding grid resolution and less computational effort as for DNS. Additionally, on-going advances in computing lead to increasing computer performance and decreasing costs for computational time. Therefore, LES becomes more and more attractive for industrial applications.

- For **Reynolds-averaged Navier-Stokes (RANS)** simulations an averaged version of the Navier-Stokes equations is solved. Here all turbulent scales are modelled. The requirements regarding grid and time resolution are comparatively low so that typical RANS simulations can be performed on conventional workstation computers. Hence, RANS simulations today are still state-of-the-art for a wide range of industrial applications.

Figure 2.15 shows a turbulent simulation of an arbitrary quantity versus time for the three computation approaches. With DNS all time variations of the quantity would be captured. Using LES would only predict the low-frequency variations of the quantity. The RANS simulation would predict the constant mean value of the quantity. For more detailed information on the general modelling approaches please refer to pertinent literature like the books by Pope [96] or Poinsot and Veynante [95].

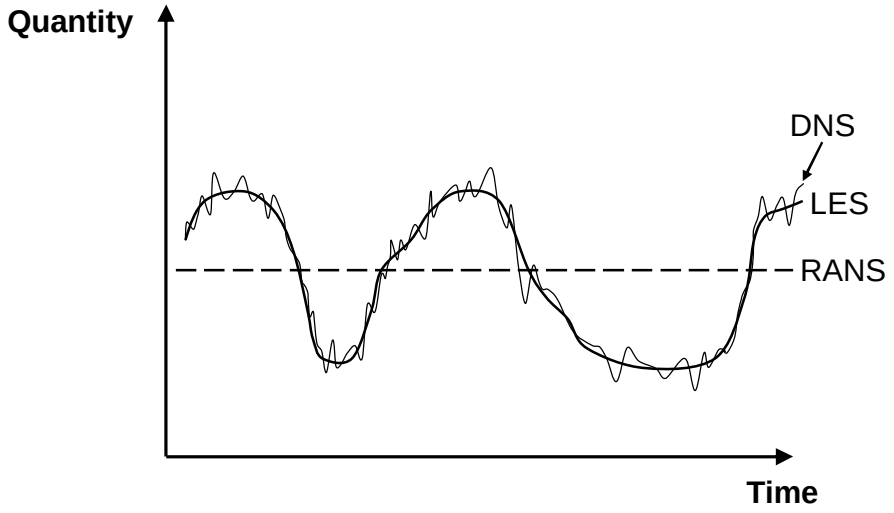

Figure 2.15: Qualitative comparison of the DNS, LES and RANS approach for a turbulent simulation of an arbitrary quantity [95]

Another modelling method that was developed in the late 1990s is **detached-eddy simulations (DES)**. DES may be described as a hybrid RANS/LES approach in which the model uses LES in regions far from solid boundaries while treating near-wall regions with a RANS type model. Due to this simplification, the grid resolution for DES is not as demanding as for LES so that the computational effort is significantly decreased. Hence, it is assumed that DES has potential to replace RANS simulations in the short-to-medium term. First reviews of DES hybrid models can be found in the publications by Cabot and Moin [12] or Piomelli and Balaras [93].

However, for modelling the not directly solved turbulent scales all approaches except DNS require additional equations. Here also multiple approaches are established and can be selected depending on the individual type of problem. Commonly used turbulence closure models are the two-equation approaches *k*-ε, the *k*-ω and the *shear stress strain* (SST) model. Furthermore, the *explicit algebraic Reynolds stress model* (EARSM), which is basically an extension of the standard two-equation models, is frequently used. A detailed discussion of these models is given in [96], for example.

However, due to the nature of numerical modelling, the simulations have a limited accuracy and multiple error sources. Typical errors in CFD simulations may originate from general model errors, especially for turbulence and combustion, and from numerical errors such as spatial and temporal discretisation, round-off, and iteration. Hence, CFD simulations should be validated regularly.

Within the present study the following two specific simulation tasks were of interest:

- **Fuel/air mixing simulations** at Siemens are typically carried out with a steady RANS approach. The simulations usually do not include the chemical reaction of the fuel/air mixture. As this approach has limitations especially for highly turbulent flows, a detailed validation with LIF measurements is done in scope of this thesis. In a future study, the LIF data will also serve as benchmark to evaluate the accuracy and effort of DES and LES compared to the standard RANS approach.

- **Turbulent premixed combustion simulations** at Siemens are also typically performed using the RANS approach. The modelling of the fuel/air reaction is based on the widely accepted GRI 3.0 mechanism [117]. To allow for a better comparison of CFD simulations and chemiluminescence images recorded in scope of this study, Görs [30] added the OH* and CH* formation and consumption reactions as suggested by Kojima et al. [66]. Furthermore, Görs developed a line-of-sight post-processor based on the commercial ray tracing tool *POV-Ray* to simulate relevant effects like the line-of-sight signal integration, light fading, and absorption.

2.4 Conclusions

The preceding chapter started with a brief introduction to optical measurement techniques typically applied in the field of combustion research. Afterwards, the fundamentals of LIF and chemiluminescence imaging were discussed in more detail, because the LIF imaging technique is used for the investigation of fuel/air mixing in a full-scale atmospheric-pressure cold flow test rig and the chemiluminescence imaging is applied at a full-scale high-pressure combustion test rig in the scope of this thesis. Furthermore, the experimental setup of a previously used physical probing technique was introduced, because results derived with this technique will be compared with results derived from the LIF experiments later in chapter 3.3.5. Finally, numerical methods for fuel/air mixing and turbulent combustion applied at the Siemens Energy Sector were briefly discussed, as they will be used for a comparison with the measured fuel/air mixing and chemiluminescence images in following chapters.

3 Acetone-LIF Imaging Applied to Gas Turbine Combustors

3.1 Introduction

This chapter covers the application of acetone tracer-LIF measurements at different full-scale Siemens gas turbine combustors with the goal to investigate their fuel/air mixing behaviour. First of all, general aspects like the lab facilities, the scaling approach for atmospheric cold flow conditions, the optical setup, and the image post-processing procedure are introduced. As the measurements were conducted at different burner types from two different gas turbine versions (SGT5-4000F and SGT6-8000H), the engine-specific details of the experimental setup, the testing procedure, as well as exemplary test results and their interpretation are presented in separate sub-chapters. Additionally, LIF measurement results from the SGT5-4000F burner are compared to results from suction probe measurements and steady RANS CFD simulations.

3.2 Experimental Method

The presented tracer LIF experiments were performed in suction operation mode at atmospheric pressure and without air preheating. The approach for the required scaling from engine to atmospheric cold flow conditions is described in chapter 3.2.1. The experimental setup was located in the Siemens flow lab shown in Figure 3.1. Its main components were two full-scale optical test rigs for SGT5-4000F and SGT6-8000H combustors, the tracer gas supply facility, the air supply line, a data acquisition system, the excimer laser, and required optical elements like different lenses and mirrors installed on a traverse unit. Due to the location of the exper-

imental setup in this factory building with different working areas, the area was enclosed with steel plates and certified laser safety curtains to minimise potential risks for uninvolved people e.g. by laser radiation. Additionally, the laser beam path was encapsulated as far as possible already inside the enclosed area. Furthermore, sufficient measures to ensure a safe operation of the tracer gas supply facility in terms of fire/explosion safety were taken.

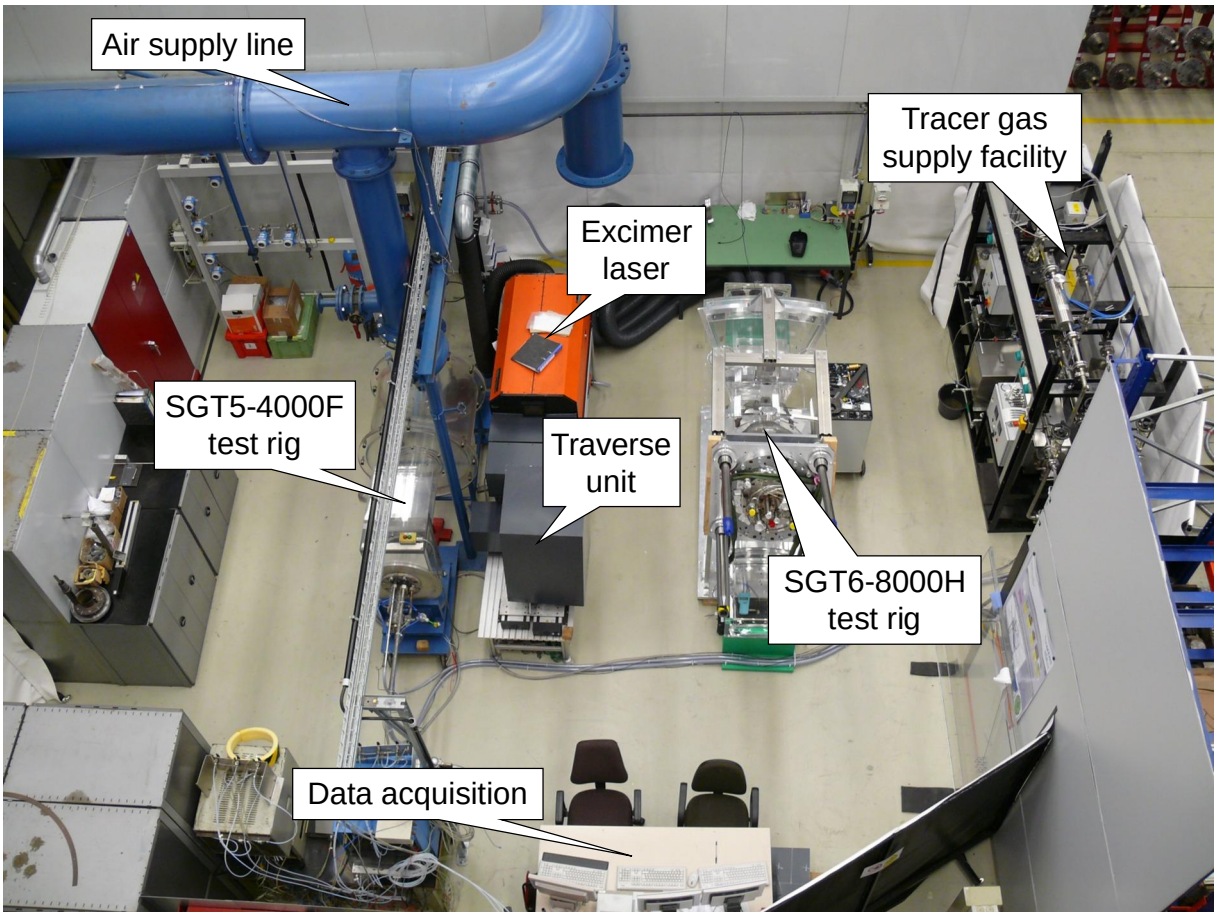

Figure 3.1: Tracer-LIF setup in the Siemens flow lab in Mülheim

The test rigs shown in Figure 3.1 mimic relevant engine geometry and provide optical access to the combustion chambers. As LIF experiments were carried out at burners from the SGT5-4000F engine and the SGT6-8000H engine, two separate test rigs were used. A detailed description of the rigs is given in chapter 3.3.1 and 3.4.1, respectively. The selected tracer for the LIF measurements was acetone mixed in nitrogen as carrier gas. To provide sufficiently high mass flows of tracer gas with a defined mixture of acetone and nitrogen the tracer gas mixing facility was developed and installed. This facility is described in chapter 3.2.2, also including a brief description of the general lab supply facilities. The excimer laser provided the light required to induce the acetone fluorescence. The additional optical elements for light

sheet generation, laser beam energy recording, etc. were installed on a traverse unit to allow measuring the fuel/air mixing at different locations and at different test rigs without modifying the optical setup. This setup is presented in chapter 3.2.3. Finally, the post-processing procedure for the recorded LIF images is described in chapter 3.2.4.

3.2.1 Flow Boundary Conditions and Scaling Approach

To evaluate the flow behaviour of combustor hardware at real engine conditions based on data from experiments performed at atmospheric cold flow conditions, it is necessary to consider some rules of similarity and scaling when defining the flow boundary conditions for the experiment.

Scaling factor for the air mass flow

According to Aurel Stodola's early studies [118] one of the most important similarity parameters for the characterisation of a turbine is the relative pressure drop $\Delta p/p$. Hence, this parameter is kept constant while scaling the air flow for the experimental boundary conditions. This leads to

$$\frac{\Delta p_{exp}}{p_{exp}} = \frac{\Delta p_{GT}}{p_{GT}} \qquad \text{Equation 3.1}$$

where the index *exp* represents the thermodynamic boundary conditions of the experiment and *GT* represent real gas turbine conditions. Generally, the pressure drop for incompressible fluids is determined as:

$$\frac{\Delta p}{p} = \zeta \times \frac{\rho v^2}{2p} \qquad \text{Equation 3.2}$$

ζ is the friction factor, ρ is the fluid density, and v is the fluid velocity. The assumption of incompressibility is valid for compressible fluids for Mach numbers < 0.3.

Substituting v and ρ in Equation 3.2 by

$$v = \frac{\dot{m}}{\rho A} \quad \text{and} \quad \rho = \frac{p}{RT} \qquad \text{Equation 3.3}$$

and inserting the result in Equation 3.1 leads to

$$\frac{\zeta_{\mathrm{exp}} \dot{m}_{\mathrm{exp}}^2 R_{\mathrm{exp}} T_{\mathrm{exp}}}{2 p_{\mathrm{exp}}^2 A_{\mathrm{exp}}^2} = \frac{\zeta_{\mathrm{GT}} \dot{m}_{\mathrm{GT}}^2 R_{\mathrm{GT}} T_{\mathrm{GT}}}{2 p_{\mathrm{GT}}^2 A_{\mathrm{GT}}^2} \qquad \text{Equation 3.4}$$

Here, $\dot{m}$ denotes the mass flow, R the specific gas constant, T the temperature in K and A the effective area. For air, R and A are identical for experimental and gas turbine conditions. Furthermore, ζ does not significantly change, as long as the flow is fully turbulent ($Re_t >> 10^4$). Consequently, Equation 3.4 can be reduced to

$$\frac{\dot{m}_{\mathrm{exp}}^2 T_{\mathrm{exp}}}{p_{\mathrm{exp}}^2} = \frac{\dot{m}_{\mathrm{GT}}^2 T_{\mathrm{GT}}}{p_{\mathrm{GT}}^2} \qquad \text{Equation 3.5}$$

This equation may be re-arranged to

$$\dot{m}_{\mathrm{exp}} = \dot{m}_{\mathrm{GT}} \times \frac{p_{\mathrm{exp}}}{p_{\mathrm{GT}}} \times \sqrt{\frac{T_{\mathrm{GT}}}{T_{\mathrm{exp}}}} \qquad \text{Equation 3.6}$$

Besides constant $\Delta p/p$ also the Mach-number stays constant while scaling. On the other hand, the Reynolds-number significantly decreases for the experimental cold flow conditions. But, as long as the flow is still fully turbulent ($Re > 10^5$) this is expected to only have a minor impact on the similarity of experiment and real engine. Moreover, the bulk air flow velocity at the experiment decreases. This has to be considered if time delays should be measured, for example.

Scaling factor for the tracer gas mass flow

For the tracer LIF experiments the fuel has to be replaced by the tracer gas, a mixture of acetone as fluorescent marker and nitrogen as carrier gas. The natural gas fuel injection at the investigated gas turbine combustors is based on the jet in cross-flow concept. This means that the fuel is injected through multiple small fuel nozzles arranged perpendicular to the main air flow. According to Cox [15] and Holdeman [51], the most decisive design parameter for this injection concept is the penetration depth of the fuel into the air flow. The fuel penetration

depth mainly depends on the fuel/air momentum flux ratio *J*. Hence, for the calculation of tracer mass flow in the experiment the following scaling rule is defined:

$$J_{\mathrm{exp}} = J_{\mathrm{GT}} \qquad \text{Equation 3.7}$$

For jet in cross-flow configurations, *J* can be expressed as

$$J = \frac{\rho_0 \cdot v_0^2}{\rho_\infty \cdot v_\infty^2} \qquad \text{Equation 3.8}$$

with ∞ indicating the jet flow (typically fuel) and 0 indicating the main flow (typically air). As the tracer gas has a different density as natural gas, the following requirement is derived by combining equation 3.7 and 3.8:

$$\rho_{\mathrm{tracer}} \cdot v_{\mathrm{tracer}}^2 = \rho_{\mathrm{fuel}} \cdot v_{\mathrm{fuel}}^2 \qquad \text{Equation 3.9}$$

By using Equation 3.3 the velocities of jet and main flow can be substituted. After transposing the equation and square root extraction this leads to Equation 3.10, which is valid for engine conditions:

$$\dot{m}_{\mathrm{tracer}} = \dot{m}_{\mathrm{fuel}} \cdot \sqrt{\frac{R_{\mathrm{fuel}}}{R_{\mathrm{tracer}}}} \qquad \text{Equation 3.10}$$

For the additional scaling to atmospheric cold flow conditions the same scaling approach as for the air is applied. This results in:

$$\dot{m}_{\mathrm{tracer,exp}} = \dot{m}_{\mathrm{fuel,GT}} \cdot \frac{p_{\mathrm{exp}}}{p_{\mathrm{GT}}} \cdot \sqrt{\frac{T_{\mathrm{fuel,GT}} R_{\mathrm{fuel,GT}}}{T_{\mathrm{tracer,exp}} R_{\mathrm{tracer,exp}}}} \qquad \text{Equation 3.11}$$

A possible separation of the marker substance (propane or acetone) and the carrier gas (compressed air or nitrogen) in the tracer due to different transport properties of the two species may not be important for the described practical applications since the relevant mixing processes in the investigated gas turbine combustors are not diffusion-controlled.

3.2.2 Flow Lab and Supply Facilities

The Siemens flow lab is located in a workshop hall at the Siemens factory site in Mülheim. In this lab compressed air, nitrogen, and cooling water are available in sufficient scale. Additionally, depending on the selected blower and air supply line configuration, air mass flows up to 3.5 kg/s in pressure or suction operation mode can be provided.

As described earlier, the tracer LIF experiments required sufficiently high mass flows of tracer gas with a defined mixture of acetone as fluorescent substance and nitrogen as carrier gas. The acetone concentration in the tracer gas correlates linearly with the measured fluorescence intensity. Hence, it is very important to ensure a high accuracy and reproducibility of the acetone dosing and its mixing with the carrier gas. To fulfil these requirements, a special tracer gas supply facility was designed and commissioned at the flow lab. Figure 3.2 shows a sketch of this supply facility. The main components of the facility were:

- The nitrogen supply line with a N_2 pre-heater and temperature, pressure and mass flow controllers (red).
- The acetone reservoir, pump and mass flow control unit (purple).
- The acetone evaporation unit with heat exchanger and steam generator (dark blue).
- And the static mixer followed by three burner supply lines (green).

The nitrogen was stored outside the lab in high-pressure bundles. The electrical pre-heater in the nitrogen line had an electrical power of 9 kW and was used to avoid acetone condensation in the tracer gas mixture as consequence of low nitrogen temperatures due to the expansion of the nitrogen out of the high pressure bundles. The nitrogen mass flow was controlled by a *Bronkhorst* mass flow controller (MFC). The acetone was stored in a reservoir directly in the supply facility and pumped by a mass flow controlled pump into the heat exchanger for evaporation. The heat exchanger was fed by 160°C hot steam coming from a steam generator, also with 9 kW electrical power, operated within a closed water cycle. After evaporation acetone and nitrogen were mixed in a static mixer ensuring a homogeneously mixed tracer gas. Afterwards, the mixture was split on up to three lines with separate Coriolis mass flow meters and pressure valves to adjust the split between the three lines. The lines were directly connected to different burner fuel stages.

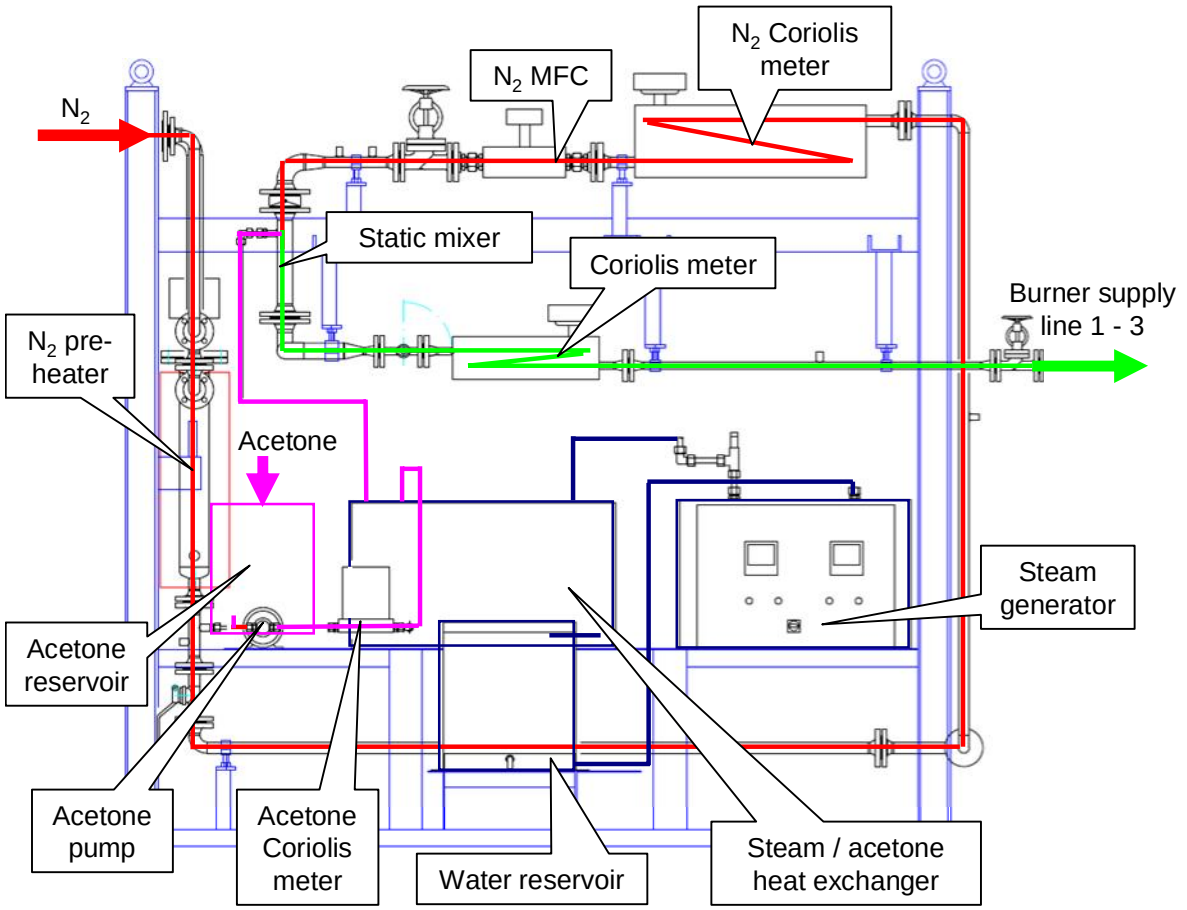

Figure 3.2: Sketch of the tracer gas supply facility

The three burner supply lines were optimized for different mass flow regions to stay within the defined mass flow measurement accuracy of ±1% for each mass flow range. The respective mass flow ranges for each line were:

- Low mass flow range: 1–15 g/s
- Intermediate mass flow range: 3–45 g/s
- High mass flow range: 20–80 g/s

All mass flows were measured with Coriolis mass flow meters to guarantee a sufficiently high measurement accuracy independent from the flow medium temperature, pressure and density (e.g., for varying acetone concentration). The mass flow, temperature, and pressure measurement devices were connected to a *Delphin* module converting the signals for the data acquisition system. A detailed piping and instrumentation diagram (P&ID), the respective list of the individual components indicated in the P&ID, and technical drawings of the supply facility can be found in Appendix A.

3.2.3 Optical Setup

Basically, the optical setup for the LIF experiment consisted of the XeCl excimer laser, an online energy monitor, a beam homogeniser, and mirrors and lenses. Some of the optical elements were installed on an *x*-*z*-traverse unit with the aim of moving the laser sheet in horizontal and vertical direction. Figure 3.3 shows the details of the optical setup.

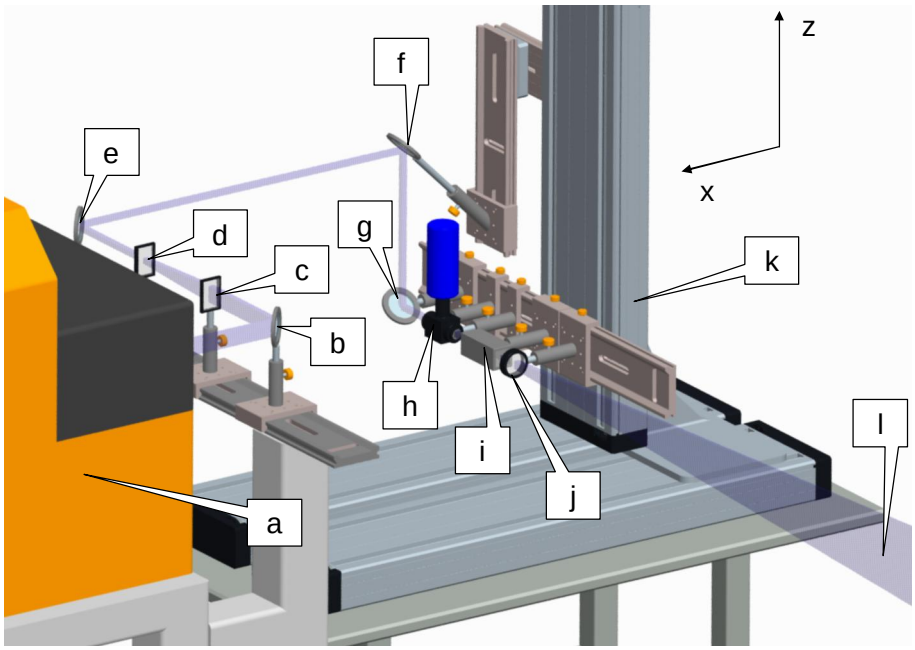

Figure 3.3: Sketch of the optical setup for the LIF measurements

a. *Lambda Physik EMG EST 150* pulsed XeCl excimer laser
b. Mirror
c. Cylindrical quartz lens, $f = 150$ mm
d. Cylindrical quartz lens, $f = -50$ mm
e. Mirror
f. Mirror (fixed at constant *z*-level)
g. Mirror
h. Online energy monitor
i. *BLZ* beam homogenizer including sheet-forming optics
j. Spherical Fourier quartz lens, $f = 1000$ mm
k. Traverse unit to move the laser sheet along the *x*- and *z*-axis in steps of 1 mm
l. Laser sheet, approx. 130 mm high and 1 mm thick

The XeCl excimer laser (a) produced a pulsed beam with 308 nm wavelength. The beam dimension was 30 mm in vertical direction and 10 mm in horizontal direction. The first mirror (b) deflected the beam by 90° to the cylindrical lenses (c) and (d). Lens (c) was a cylindrical lens with a focal length of 150 mm and was required for converging the beam in vertical direction. The second lens (d) was also a cylindrical lens, but with a focal length of −50 mm to parallelise the beam again. This resulted in a beam shape of 10 mm in vertical and horizontal direction, which was essential for passing the apertures of the energy monitor and the beam homogeniser, respectively. Next, the beam direction was deflected three times by the mirrors (e), (f) and (g). Mirror (f) was fixed on an *x*-*z*-positioning table (= traverse unit) at a constant *z*-level and could only be moved in *x*-direction, whereas mirror (g) and the subsequent components (h) to (j) could be moved in *x*- and *z*-direction. For accurate measurements at different measurement planes it was extremely important to adjust the beam path between mirrors (e) and (f) and between the mirrors (f) and (g) exactly parallel to the *x*- and *z*-arms of the traverse unit. The energy monitor (h) extracted a small portion of the beam and measured the respective laser energy for every single laser pulse with a photo-diode. This laser energy value was required for the post-processing to normalise all recorded images to the same reference laser energy value. The beam homogeniser (i) was used to compensate spatial fluctuations of the laser energy distribution in the laser beam and, furthermore, to expand the laser beam to a sheet. For details of the working principle of the beam homogeniser please refer to [92]. Finally, a spherical Fourier lens (j) with a focal length of 1000 mm was used to optimise the laser sheet divergence and thickness for the distance where the measurements were done. All mirrors were specially coated for 308 nm and all lenses were made of fused silica.

The optical setup was completed by an Intensified CCD-camera system from *LaVision GmbH*. As the location of the camera system and the selected camera lens were different for the SGT5-4000F and the SGT6-8000H setups, they are described in chapter 3.3 and 3.4, respectively.

3.2.4 Image Recording and Post-Processing Procedure

The image post-processing procedure is illustrated in Figure 3.4.

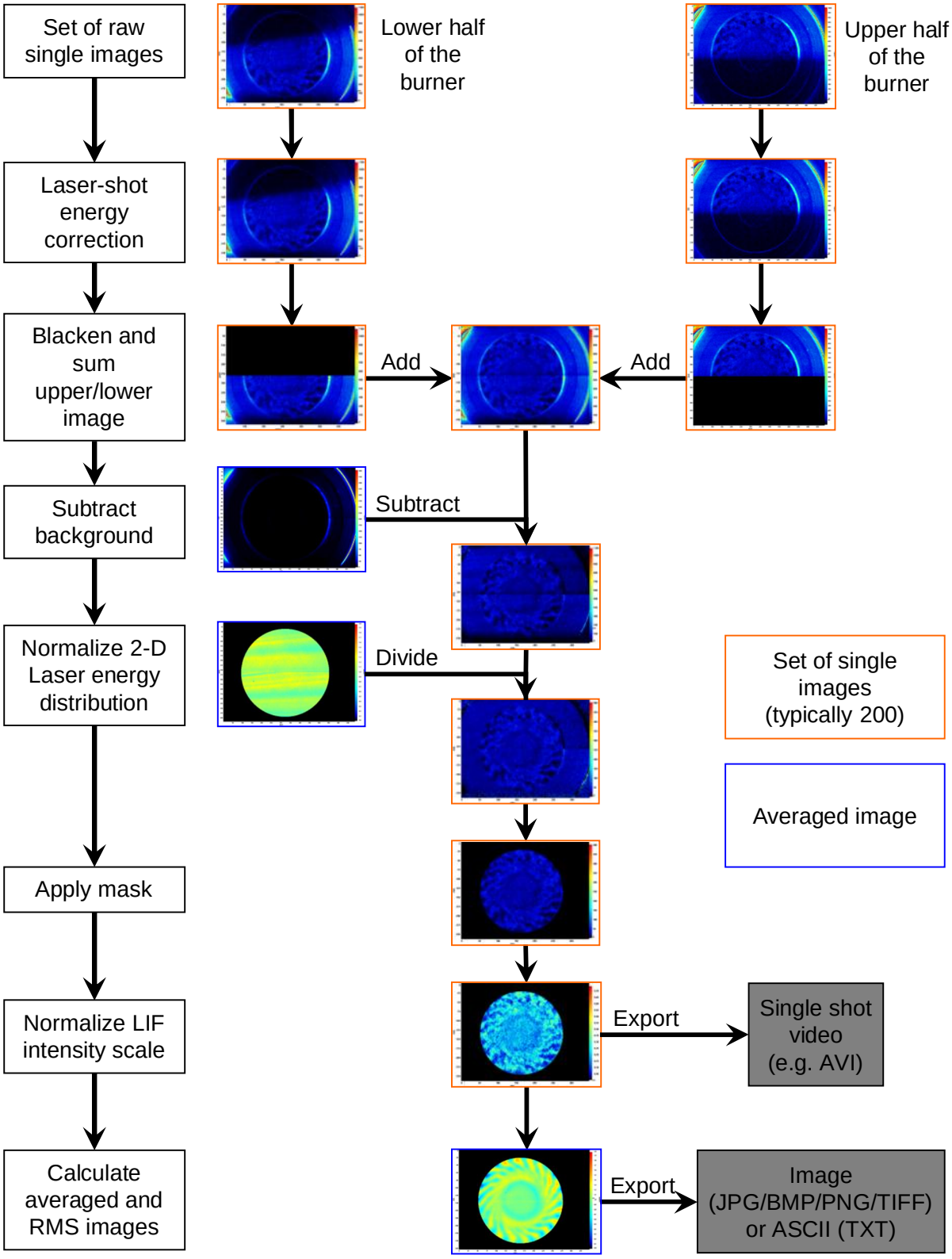

Figure 3.4: LIF image post-processing procedure

During the LIF experiments for each measurement point a set of so-called “single images” was recorded. A typical number of single images for one measurement point was 200, which is statistically high enough for the calculation of meaningful averaged images and the temporal standard deviation. The single images were recorded with a frequency of 4 images per second and a camera exposure time of 5 μs to capture the full amount of emitted fluorescence. However, the duration of fluorescence-signal emission was an order of magnitude shorter so that a single image temporally “froze” the local tracer concentration.

The first step in image post-processing was to normalize the single images to an identical laser energy reference value by using the laser energy as recorded for each single image by the online energy monitor.

As mentioned before, the upper and lower half of the burner outlet was recorded sequentially, since the burner outlet area was too big to be covered by a single laser sheet. Therefore, in the next step the lower half of the upper images and the upper half of the lower images were set to zero and afterwards added to obtain the full 360° images.

The next steps were the subtraction of an averaged background image and the correction of the 2-D laser energy distribution profile. For this purpose, additional sets of the background and the 2-D laser-energy distribution were recorded for each test configuration. The background images were recorded with the laser switched on, but without tracer gas fed through the supply lines. The 2-D laser-energy distribution was recorded with the laser switched on and with a homogeneous tracer gas filling inside the test rig. To avoid an explosive acetone/air mixture, the test rig was always flushed with pure nitrogen before filling it with tracer gas. The 2-D laser image was masked to only show the area of interest and normalized to a mean value of 1 so that the LIF mixture image intensity in the single images of the recorded measurement points was not changed. Furthermore, the 2-D laser energy distribution image was corrected in terms of laser-light absorption across the measurement plane by using a macro based on the law of Lambert-Beer. Figure 3.5 shows a typical post-processed image of the background (left) and the 2-D laser-energy distribution (right).

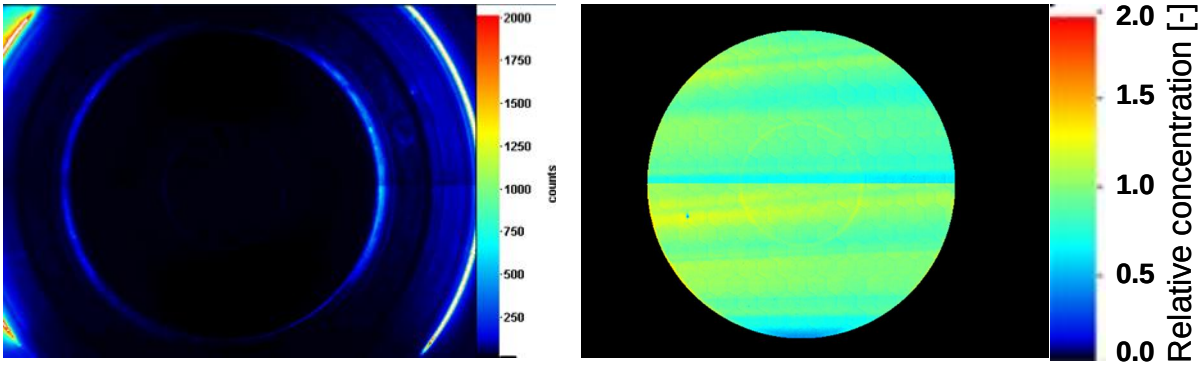

Figure 3.5: Typical background image (left) and normalised 2-D laser-energy distribution image (right)

After the background subtraction and energy distribution correction, a mask was added to the fuel/air mixing images to set everything else than the area of interest to zero (= black).

Additionally, the global average LIF-intensity for each averaged image was calculated to normalise the LIF-intensity to an intensity scale where 1 means perfectly mixed (green), values < 1 are fuel-lean (blue to black) and values > 1 are fuel-rich (yellow over red to white).

For selected cases additional information was derived from the images after finishing the above described post-processing procedure. In particular, the circumferentially as well as radially averaged fuel concentration profiles (as already used for the suction probe measurement investigations), histogram plots of the intensity distribution, and the global standard deviation of the measured concentrations were calculated to allow for a more detailed investigation of the fuel profiles.

The Image recording and post-processing in this study was performed with the *LaVision* software "*DaVis*", version 7.2. This software included most of the post-processing steps as macros, allowed batch processing, and featured numerous standard formats for the export of images or videos.

3.3 Setup and Results for the SGT5-4000F Combustor

This chapter focuses on the LIF experiments conducted at Siemens SGT5-4000F combustors. The SGT5-4000F engine was introduced in 1996 and is equipped with the characteristic annular combustion chamber with 24 so-called *Hybrid burners*. The Hybrid burner is a swirl-

stabilised lean premixed combustion system with a central pilot burner. The first Hybrid burner version was equipped with a small diffusion pilot to combine the advantages of lean premixed flames (low NO_x) and diffusion flames (stable combustion) and to extend the operating range of premixed combustion to leaner part load conditions [120].

Afterwards, frequent evolutionary design improvements of the combustion system were released to meet the continuously changing market requirements. Major evolution steps were the introduction of the cooling-air reduced combustion chamber (CAR) with impingement-cooled ceramic heat shields in 2005, a premixed pilot (PMP) in 2006, and an aerodynamic premix burner optimisation in 2007 [62]. The base power output at ISO conditions from the latest SGT5-4000F version is 295 MW with a pressure ratio of 18.8 and a gross efficiency of 40%. The latest burner design evolution as used in this engine version was defined as baseline variant for the presented LIF experiments. Additionally, different prototype Hybrid burner variants were investigated to evaluate their potential for future engine applications.

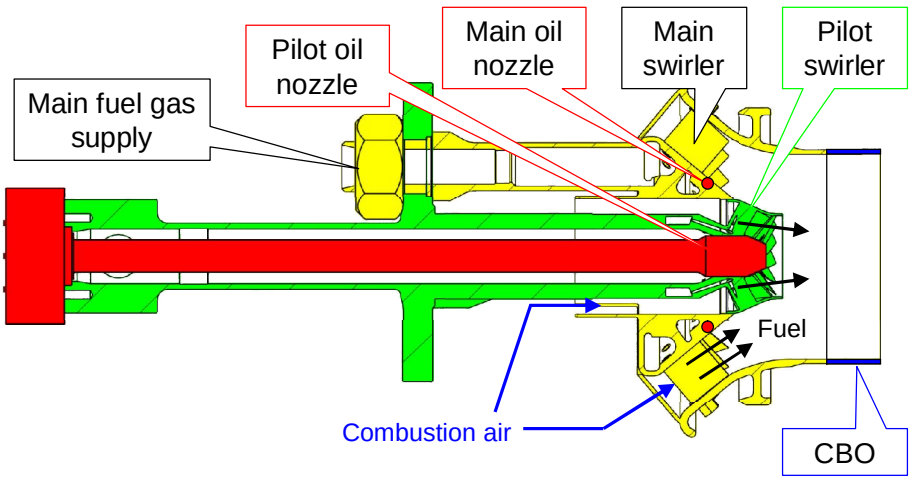

Figure 3.6: Principal sketch of the Hybrid burner design [62]

Figure 3.6 shows a principal sketch of the Hybrid burner design on the example of a dual fuel version for natural gas and oil operation. The main parts of the burner are the main stage with natural gas and oil nozzles (yellow and red), the natural gas pilot (green), the pilot oil nozzle (red), and the Cylindrical Burner Outlet (CBO, blue). A burner without CBO is called NBO burner. The main and pilot fuel gas is injected through holes in the swirler vanes (black arrows). Some of the investigated prototype burner variants were equipped with an additional second natural gas stage in the main burner (yellow) where the split between these two stages allowed an additional variation of the fuel/air mixture. In the following the respective main

stages will be referred to as “A” and “B” and the pilot stage as “P”. The A-, B-, and P-stage were connected to the three supply lines coming from the tracer gas supply facility so that arbitrary fuel splits between the different stages could be set.

More details of the SGT5-4000F experimental setup and the test rig are introduced in chapter 3.3.1. Afterwards, the testing procedure is described in chapter 3.3.2. Exemplary test results are presented and discussed in chapter 3.3.3. Finally, the selected results are compared to test results from suction probe measurements (chapter 3.3.4) and steady RANS CFD simulations (chapter 3.3.5).

3.3.1 Experimental Setup

For the acetone LIF measurements different design variants of the Hybrid burner were installed in a full-scale single burner cold flow mixing test rig (see Figure 3.7). This test rig was completely made of acrylic glass and mimicked important features of the geometry of a SGT5-4000F engine, e.g. the 180° flow turn from the air inlet to the burner. A relevant simplification compared to the real engine (besides the single-burner setup) was the cylindrical flow channel downstream of the burner outlet.

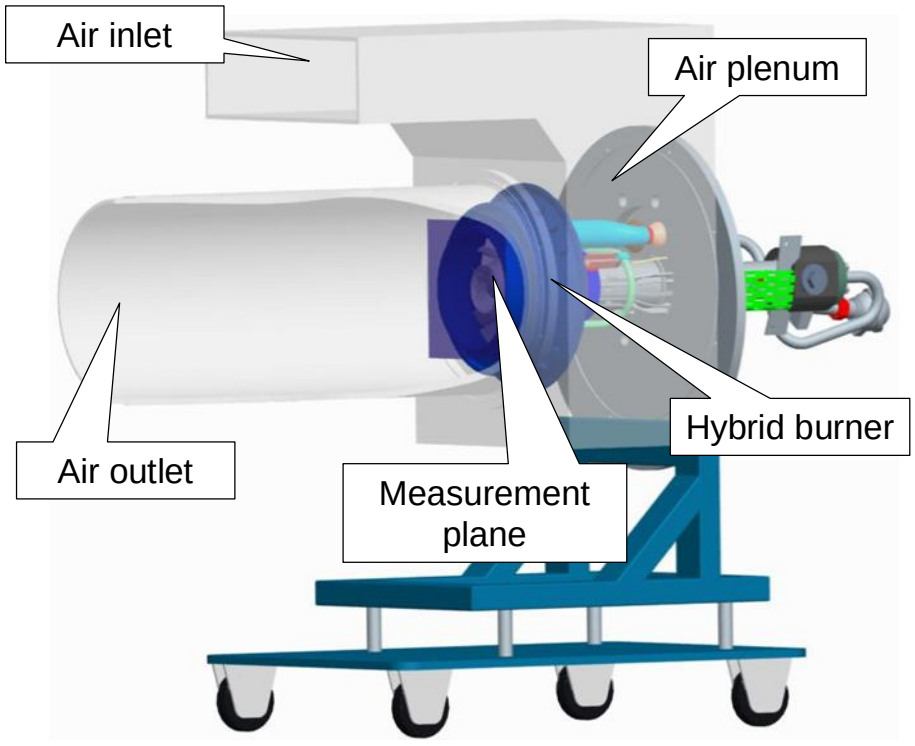

Figure 3.7: SGT5-4000F single burner mixing test rig

Because standard acrylic glass is not transparent in the wavelength range required for the laser-induced excitation of acetone (here: 308 nm), the cylindrical flow channel downstream of the burner had to be replaced by a similar cylinder made of a UV transparent material. A standard material widely used for this purpose is quartz glass. However, the manufacturing of a cylinder with a required diameter in the range of 300 mm is challenging and expensive. Consequently, the feasibility of different other materials was investigated prior to the test rig modification. In this context, a special UV-transparent acrylic glass, which was originally developed for medical and tanning bed industry applications, was investigated. Laboratory tests showed that at atmospheric conditions the selected tracer (acetone) evaporates faster than it would take to seriously harm the surface of the selected material. Further advantages of this material were its ability to be machined into complex geometries and its comparatively low price. Hence, the UV-transparent acrylic glass was finally selected for the application in frame of the present study. For more details of the material's properties like transmission spectra please refer to Appendix C.

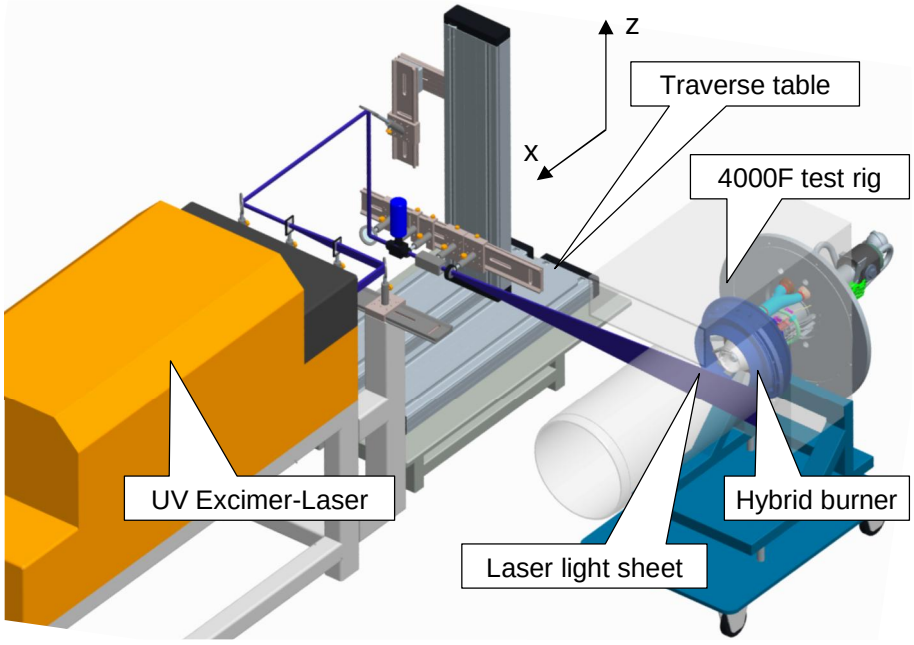

Figure 3.8: Experimental setup for the investigation of SGT5-4000F combustors

For the LIF experiment the excimer laser and the traverse unit with the laser light sheet-generating optics were positioned next to the modified test rig (see Figure 3.8). By using the traverse unit the laser light sheet could be moved to different axial positions perpendicular to the burner outlet plane.

The acetone fluorescence signal was recorded with a *LaVision Imager Intense* CCD-camera with UV-sensitive *LaVision IRO* image intensifier and a 100 mm *EADS Cerco* UV lens with an *f*-number of 2.8. The camera system was fixed on a stable aluminium rack located behind the downstream plenum of the test rig. The viewing direction was against the flow direction towards the burner outlet perpendicular on the laser sheet plane.

3.3.2 Testing Procedure

The LIF experiments were performed at flow boundary conditions scaled from real engine conditions. Figure 3.9 shows a matrix of the investigated boundary conditions, normalised to the reference conditions at 100% GT load, also referred to as *base load* (red ball).

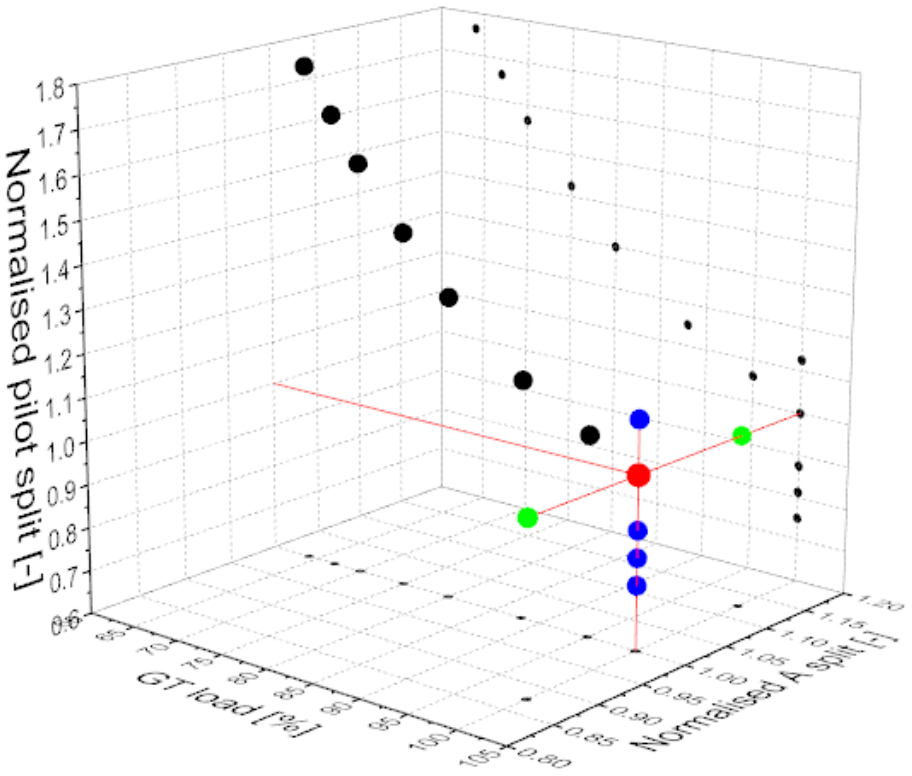

Figure 3.9: Matrix of investigated boundary conditions during the LIF experiments

As can be seen, the fuel and air mass were varied to simulate a real engine loading curve (black balls). Furthermore, the A/B split of the main stage (green) and the overall pilot stage split (blue) were varied at base load reference conditions.

The test procedure was repeated for seven Hybrid burner variants including different fuel gas hole patterns, main air flow-conditioning devices, and pilot/main burner combinations. The

selection of these burner combinations was aligned with high pressure combustion tests with the aim to compare results from “classical” emission and dynamic pressure measurements with the measured mixing characteristics. One burner configuration was furthermore selected for a detailed comparison with CFD simulations. For this purpose the three different A/B fuel stage splits at 100% load (green and red balls) were additionally measured at five different axial positions to compare the data at different mixing lengths.

3.3.3 Results and Analysis

In this section exemplary LIF mixing measurement results are presented. This includes details of a selected reference case in form of post-processed images, histograms of the relative fuel concentration, and radial and circumferential fuel profiles derived from the images. Additionally, the mixing fields at different flow boundary conditions and from a NBO burner, an identical burner with CBO and a modified CBO burner are compared. The respective measurement planes for the NBO and the CBO burners can be seen in Figure 3.10.

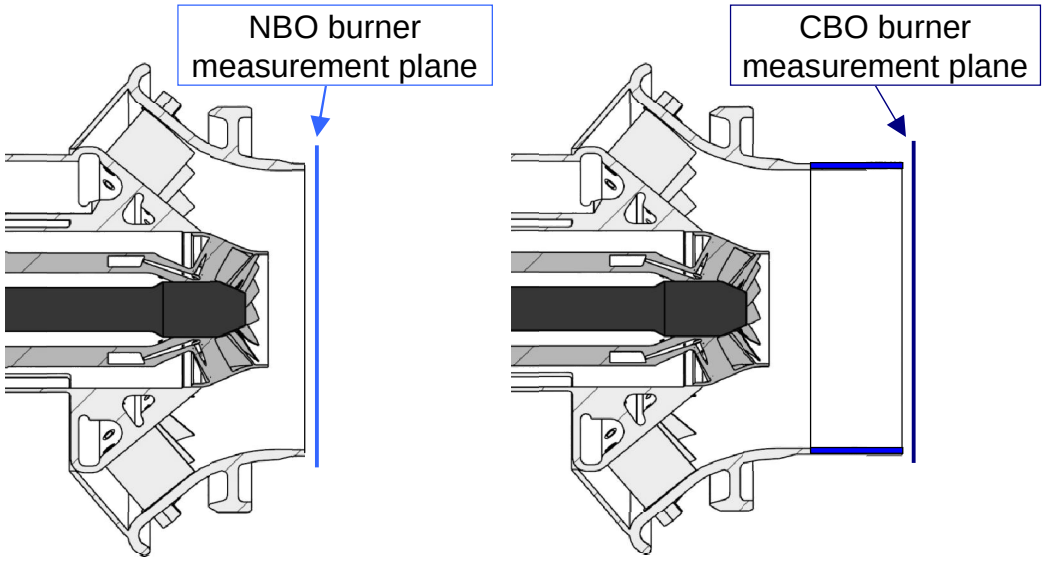

Figure 3.10: Location of LIF measurement planes for NBO (left) and CBO (right) burner configurations

Figure 3.11 shows typical examples of post-processed single images of the NBO burner variant at base load reference conditions. All images presented in this section are looking against the flow direction. It can be seen that the mixture field in the pilot region is comparatively homogeneous and does not significantly change from image to image. The premix burner region, on the other hand, shows a temporally less stable mixing field which has also a wider

range of mixture quality. Especially towards the outer radius, the spread between fuel-rich and fuel-lean regions increases due to the decreasing relative fuel penetration depth caused by the increasing distance between the vanes from inner to outer radius. Additionally, a tendency to a fuel-rich and a fuel-lean ring may be estimated in the region between the main and pilot burner.

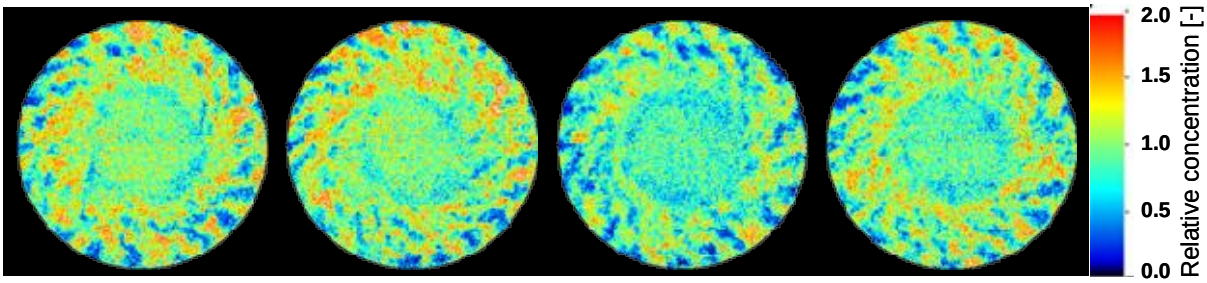

Figure 3.11: Typical single images of the NBO burner variant at base load reference conditions

However, for the comparison of different mixture fields, e.g. from different hardware variants or boundary conditions, averaged images calculated from a set of single images are more feasible. Since averaged images lose all temporal information, images of the temporal standard deviation (STD) can be calculated, additionally. The lower the value in the STD image, the lower is the variation in the set of single images at the corresponding location. Hence, the STD images can be interpreted as a 2-D distribution of the temporal mixture fluctuations.

Figure 3.12 shows the averaged (left hand side) and STD image (right hand side) for the NBO burner base load reference case. In the averaged image one can see that the pilot region is quite well mixed. In the premix burner region again the circumferentially periodical change of fuel-rich and fuel-lean regions between the single vanes can be seen. Additionally, a fuel-lean ring surrounding the pilot cone followed by a fuel-rich ring can be seen. The lean ring close to the pilot cone could most probably be explained by the improved mixing in the shear layer between the pilot and the premix burner flow. However, compared to the single images (Figure 3.11) the maximum intensity is generally lower. Based on this it can be assumed that the averaged images typically show a more homogeneous fuel distribution compared to reality.

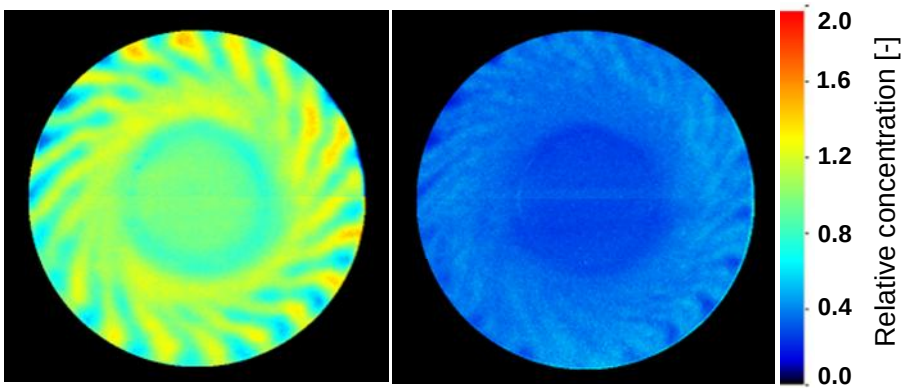

Figure 3.12: Averaged (left) and STD image (right) of the NBO burner base load reference case

The standard deviation shown in the image on the right hand side of Figure 3.12 is clearly lower than the values of the averaged or single images. This means that the overall temporal fluctuations of the mixture profile are comparatively low. Especially the pilot region shows a very low standard deviation so that it can be assumed that the pilot has a temporally quite stable mixture profile. The premix burner region shows a slightly higher standard deviation which is increasing from inner to outer radius and also seem to be slightly higher on the right side (viewing against flow direction). Moreover, the lean and the rich ring around the pilot also seem to be temporally quite stable. A higher standard deviation can be observed in the area of the rich and lean streaks of the vane channels towards the outer radius, but not in the region where the highest fuel concentration is measured, but directly next to it. This means that highest temporal mixing fluctuations occur as an envelope of the fuel rich streaks in the outer main burner region. However, it should be mentioned that the experimental conditions are isothermal meaning that all combustion chamber pressure induced fluctuations are missing and only cold flow turbulence is present.

Figure 3.13 shows the histogram of the number of pixels for each relative fuel concentration value derived from the averaged image in Figure 3.12. It is assumed that NO_x is mainly produced in hot = fuel rich areas (values > 1). For real gas turbine boundary conditions the temperature increases exponentially with increasing fuel/air ratio. Consequently, an optimal histogram should show a small standard deviation in order to reduce NO_x emission. From this point of view, the burner corresponding to the histogram in Figure 3.13 shows some potential for optimisation.

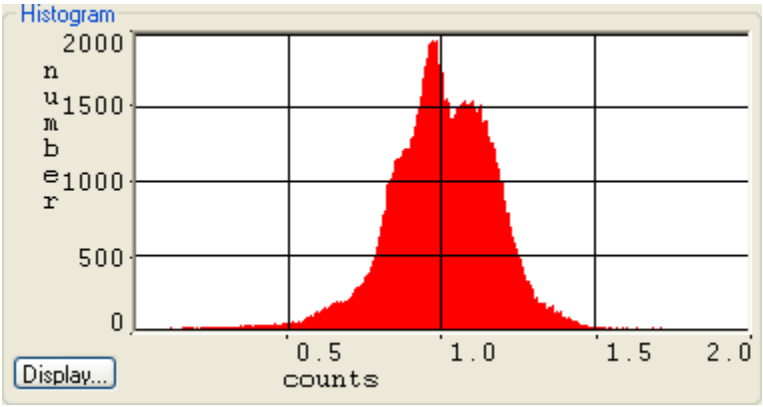

Figure 3.13: Histogram of the NBO burner base load reference case

Experience from past Hybrid burner development programs has shown that the combustion performance in terms of emissions and combustion stability at base load conditions is especially impacted by the fuel/air mixture distribution of the main swirler [62]. Consequently, equivalent concentration profiles were derived from the LIF measurements. Figure 3.14 shows the radial profile averaged in circumferential direction for the main burner flow channel from the inner to the outer radius. Figure 3.15 shows the radially-averaged fuel distribution of the main burner from 0° to 360°. The calculation procedure for these profiles is similar to the procedure established for measurements with suction probes (c.f. chapter 2.3.1), but is based on a higher spatial distribution, i.e., the number of virtual radii is 48 instead of 12 as with the suction probes and the circumferential resolution is 2° instead of 3° for 0°−180° and 6° for 180°−360° as with the suction probes. Profiles with higher spatial resolution did not show an improvement and hence were not used for further investigations.

In the radial profile in Figure 3.14 one can again see the fuel-lean ring close to the main burner hub (0 to 20% relative channel height) followed by the fuel-rich ring (20 to 55% relative channel height). Due to the circumferential averaging, the rich and lean streaks of the single vane channels cannot be seen in the radial profile and the rest of the relative fuel concentration looks quite well mixed, except for a slight decrease of fuel concentration towards the premix cone (100% channel height).

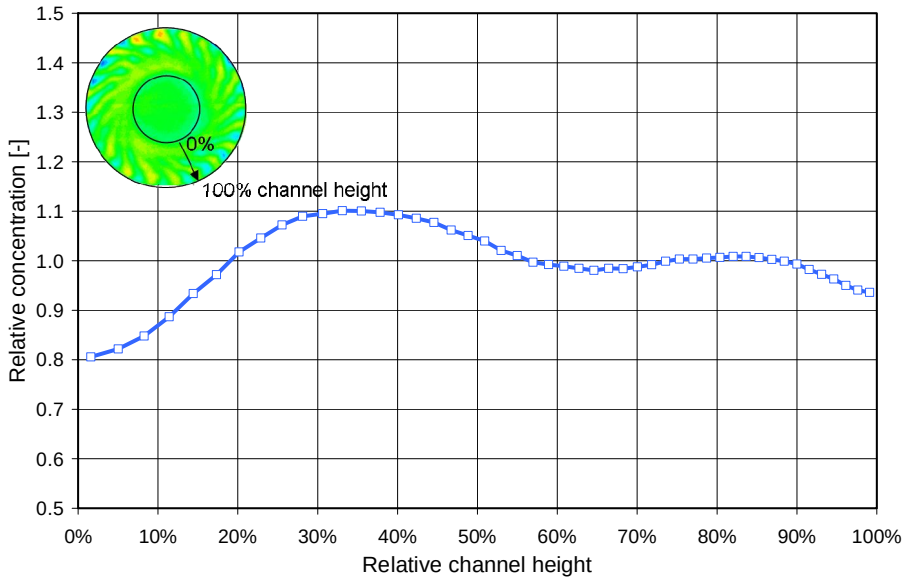

Figure 3.14: Radial concentration profile of the NBO burner main stage at base-load reference conditions

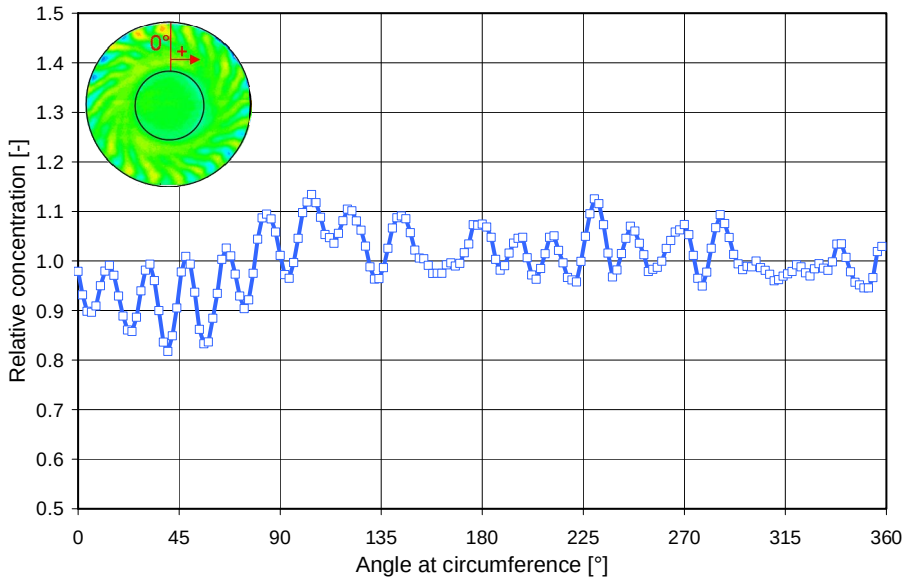

Figure 3.15: Circumferential concentration profile of the NBO burner main stage at base-load reference conditions

The circumferential profile in Figure 3.15 is dominated by the alternating lean/reach mixing profile of the single vane channels. Additionally, a generally leaner region from 0° to 80° and a slightly richer region from 80° to 290° can be identified, which might be caused by a non-uniform air distribution at the main burner inlet.

Table 3.1 shows the LIF image of the NBO burner base load reference case and two images with increased and decreased A-stage split. Furthermore, these images are compared to imag-

es of an identical burner combination, but with CBO, and another CBO burner version with modified main air inlet flow conditioner (“CBO burner variant 1”). All images were recorded at identical flow boundary conditions.

Main stage split	NBO burner	CBO burner	CBO burner variant 1	Map
Decreased A-stage	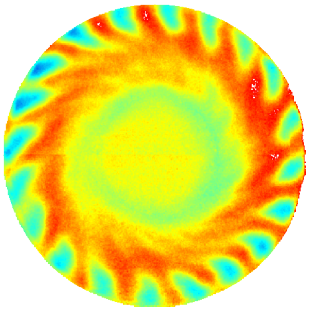	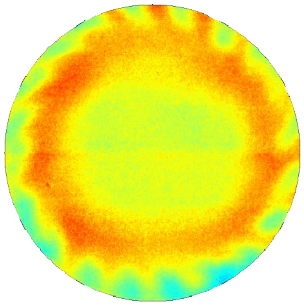	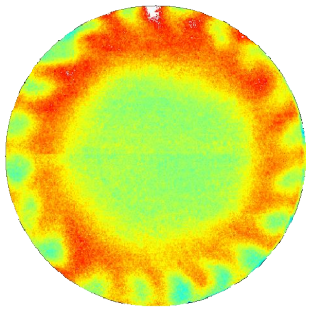	
Nominal split	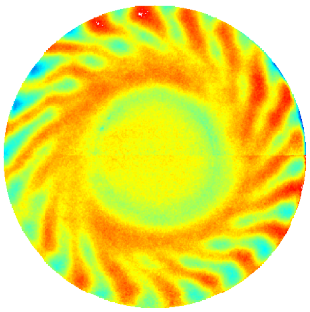	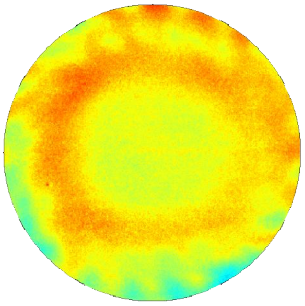	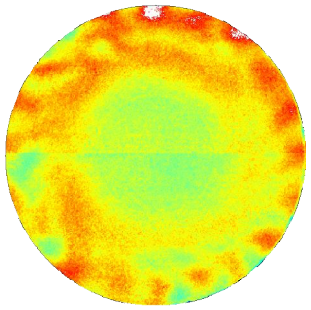	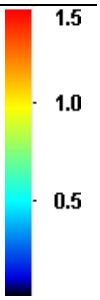
Increased A-stage	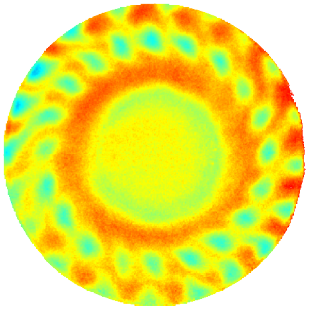	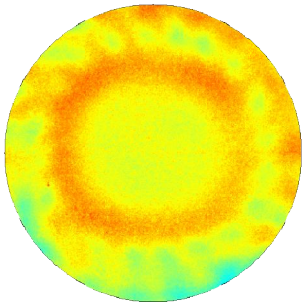	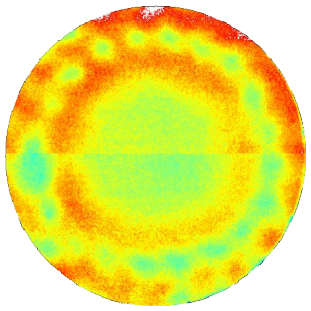	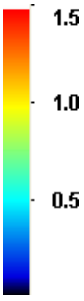

Table 3.1: LIF images of a main stage split variation for the NBO burner, CBO burner and modified CBO burner

The aim of changing the A-stage split is to change the radial fuel distribution of the main burner. At decreased A-stage split more fuel is shifted to the centre of the main burner whereas at increased A-stage split more fuel is shifted towards the inner and outer radius. This provides an effective measure influencing the combustion stability and, therefore, widening the range of stable operation of the gas turbine.

The effect of the A-stage split variation is clearly visible in all three hardware configurations, though not to the same extend. Compared to the NBO burner the increased mixing length at the CBO burner configurations leads to a generally improved fuel/air mixture. The lean ring caused by the shear layer between the main and pilot flow is not present anymore. Furthermore, the effect of the single vane channels is reduced and, due to the swirl, the fuel rich ring of the main stage is slightly shifted towards outer radius. Compared to the CBO burner the modified CBO burner (variant 1) shows less fuel in the pilot burner region, but more fuel in the main burner region. This must be caused by a change of the pilot/main air split, as the pilot stage fuel split was identical in both measurements.

The effect of the fuel-staging on the radial fuel distribution is more clearly visible in Figure 3.16, which as an example shows the radial concentration profile of the NBO burner main stage for the three different A-stage splits.

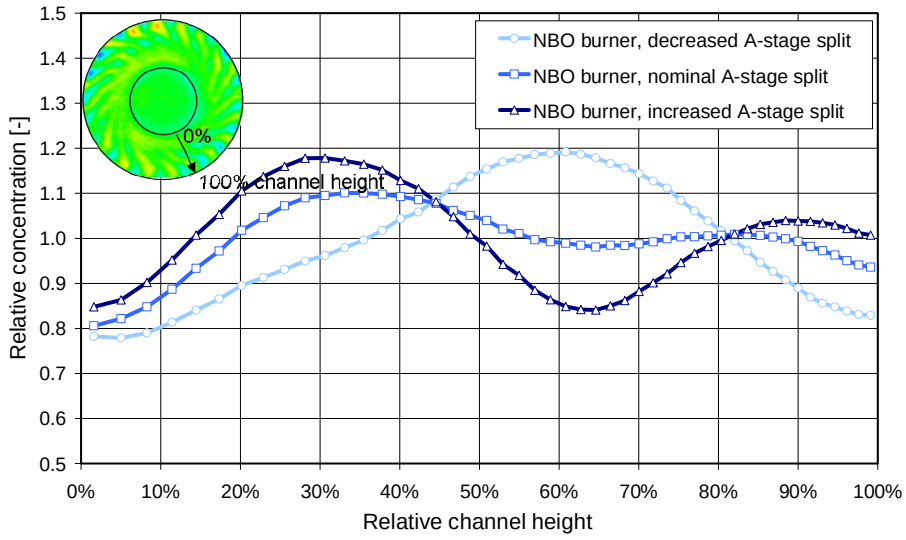

Figure 3.16: Radial concentration profile of the NBO burner at different A-stage splits

At decreased A-stage split more fuel is shifted to the region between 45% and 80% height of the main swirler channel, whereas at increased A-stage split more fuel is shifted from the centre towards the inner and outer radius.

For a better comparison of the fuel/air mixing of the different Hybrid burner configurations Figure 3.17 shows the radial concentration profiles of the NBO burner, the CBO burner, and the CBO burner variant 1 at nominal A-stage split. It can be seen that the CBO burner profile is generally more homogeneous than the NBO burner profile. Furthermore, the profile shape

is slightly shifted towards the outer radius. This was already expected from the interpretation of the LIF images and, as stated earlier, can be explained by the increased mixing length of the CBO burner. Also expected was that the modified CBO burner shows a different fuel profile compared to the CBO burner. As a consequence of the modified main air flow conditioner less air is present at the outer radius resulting in a fuel rich region and more air is present towards the inner radius resulting in a leaner fuel/air mixture. From this point of view the modified main air flow conditioner would not be recommended for real engine applications.

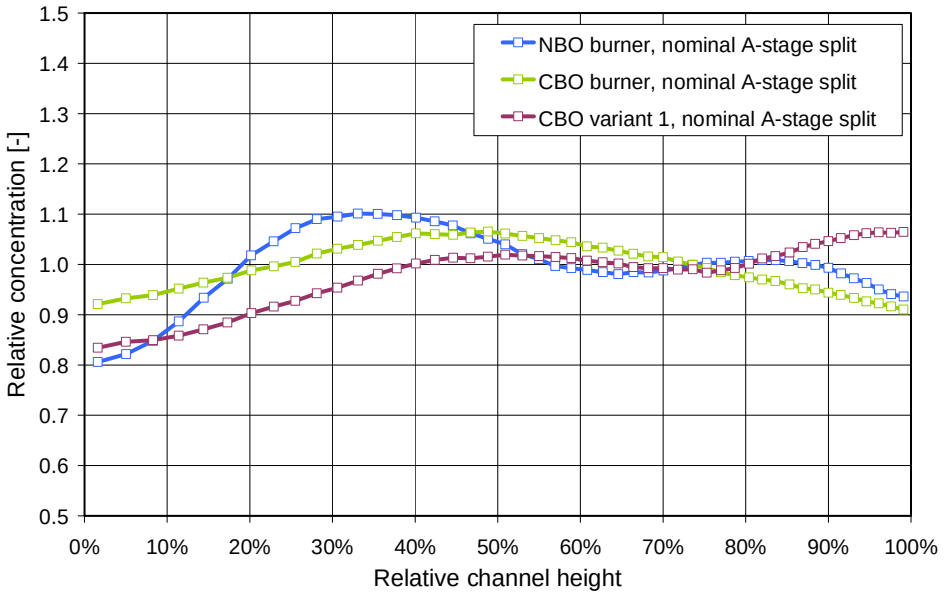

Figure 3.17: Radial concentration profile of the NBO burner, CBO burner and modified CBO burner at nominal A-stage split

The histograms of the three Hybrid burner configurations and the different A-stage splits are shown in Table 3.2. The general trends of the effect of the A-stage variation are similar for all three burner configurations. The best fuel/air mixture is achieved at nominal split, followed by the conditions at an increased A-stage. The decreased A-stage split, however, leads to a significant increase of the second peak at values above 1. In terms of a hardware comparison the CBO burner provides the best fuel/air mixture followed by the modified CBO burner. Hence, the histograms all in all confirm the previous interpretation of the LIF images and the radial profiles.

Main stage split	NBO burner	CBO burner	CBO burner variant 1
Decreased A-stage	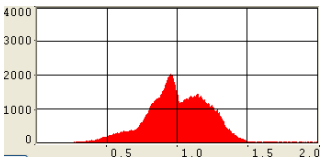	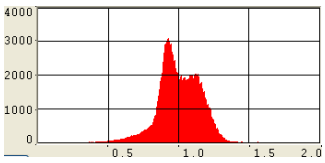	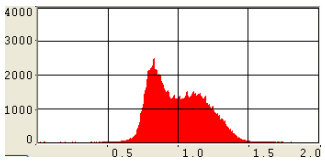
Nominal split	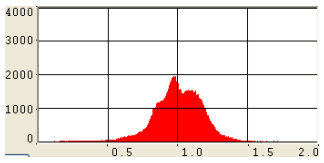	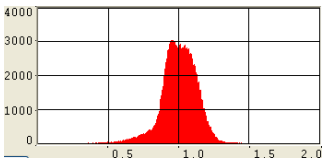	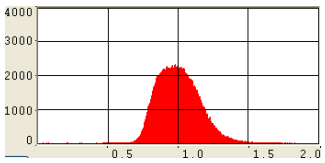
Increased A-stage	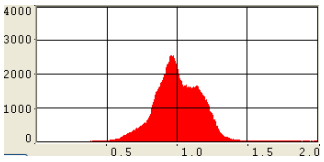	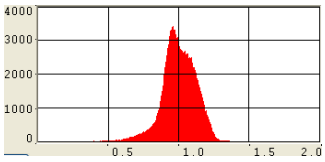	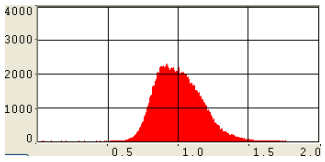

Table 3.2: Histograms main stage split variation NBO, CBO and modified CBO burner

In Table 3.3 LIF images and corresponding histograms of a load variation are shown. For the measurements the total fuel mass flow, the P-stage split and the total air mass flow were varied related to a real engine load curve. The presented results were recorded with the CBO burner. Please note that all images are separately normalised to a mean value of 1, because the focus of the fuel/air mixing investigations was on the identification of fuel lean and fuel rich regions for each specific measurement point. However, due to this normalisation procedure, the decreasing total tracer mass flow with decreasing GT load is not visible in the presented images.

GT load	LIF image	Map	LIF histogram
100%	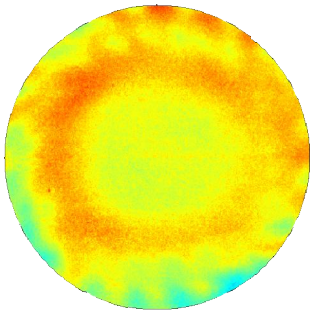	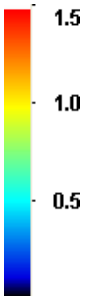	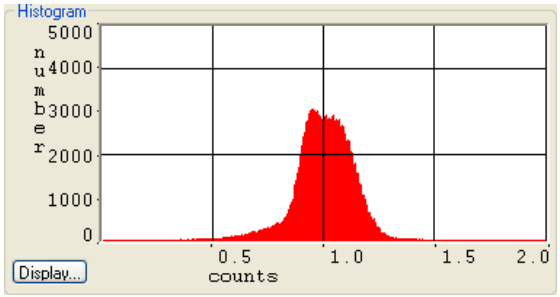
95%	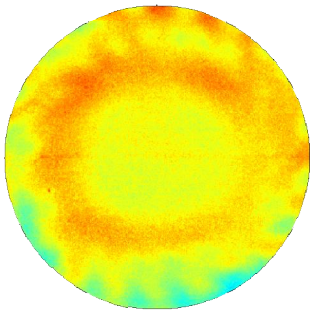	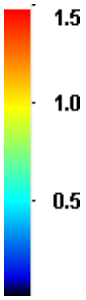	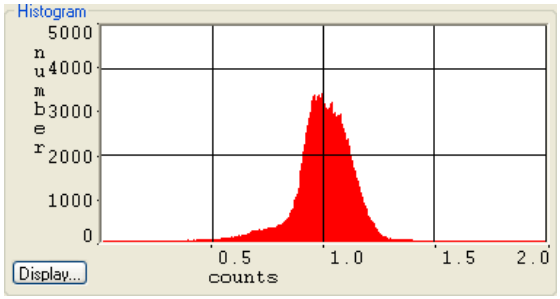
88%	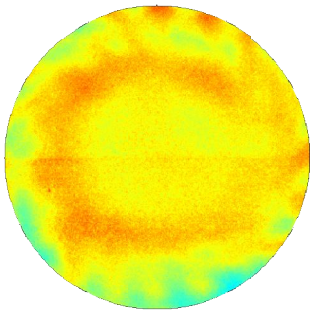	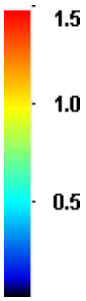	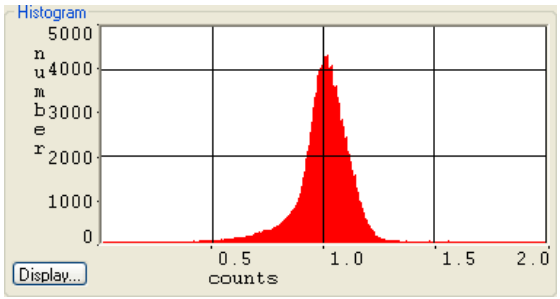
80%	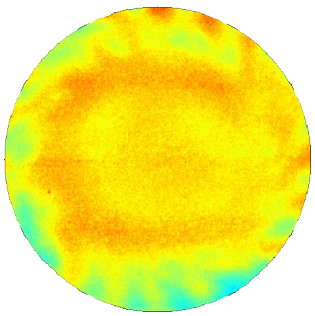	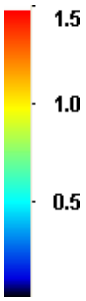	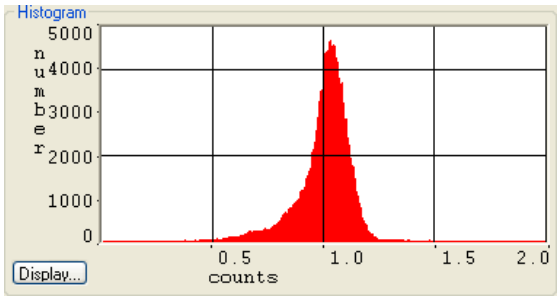

GT load	LIF image	Map	LIF histogram
75%	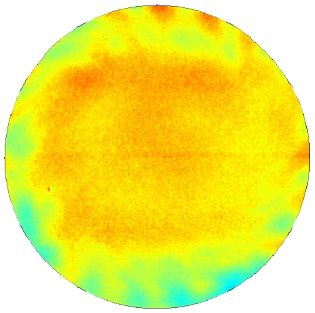	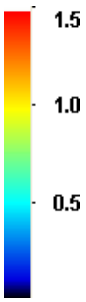	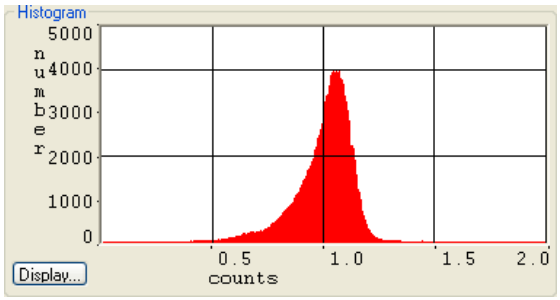
70%	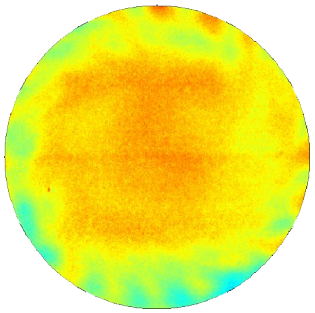	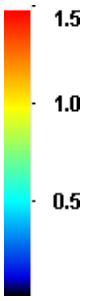	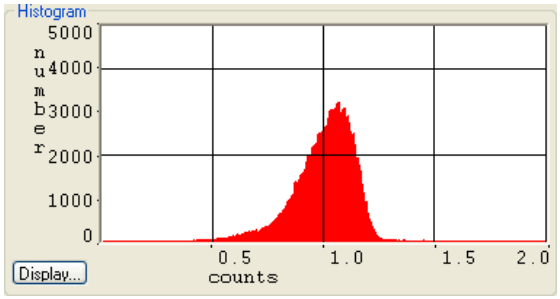
67%	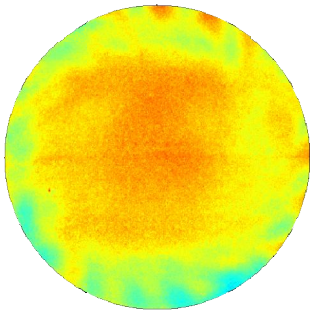	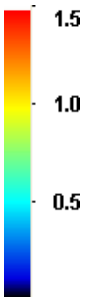	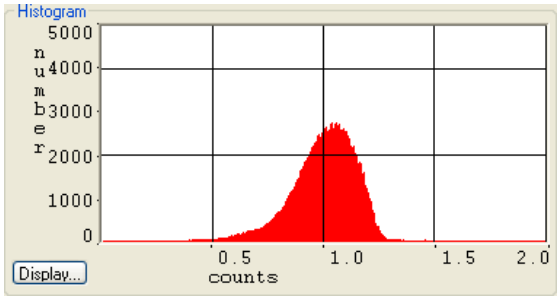
64%	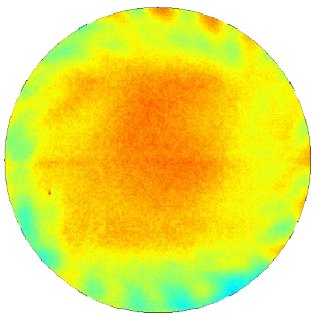	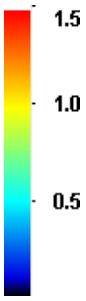	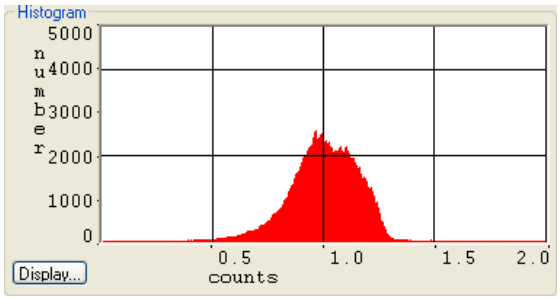

Table 3.3: LIF images and histograms for the load variation of the CBO burner

First of all, the LIF images from 100% to 64% GT load show the increasing P-stage split, which is required to stabilise the flame at decreasing load. In this context it is especially re-

markable that despite increasing tracer mass flow the pilot region seems homogeneously mixed at all load levels. The fuel/air mixture in the main burner region shows similar structures at all load levels, but with decreasing total intensity with the decreasing tracer mass flow for lower loads. This indicates that the general fuel/air mixture preparation of the Hybrid burner with the Swirler Fuel Injection (SFI) design is quite robust against changing momentum flux ratio caused by the changing mass flows in the intended operation range.

From 100% to 80% GT load the histogram shape becomes thinner with an increasing peak. Afterwards the shape becomes flatter and wider again. At 80% load and below the peak occurs at values above 1. By interpreting the histograms the most homogeneous fuel/air mixture is achieved at 88% GT load. This is most probably because the P-stage split, which is adjusted at this load level, matches well with the pilot/main air slit measured in an air capacity test rig. This means that the pilot stage at base load conditions is operated leaner compared to the main stage. However, this is only true for the cold flow case, as the pilot/main air split might change under fired conditions.

3.3.4 Comparison to Other Experimental Results

In this section the relative fuel concentration profiles from the LIF experiments are compared to results from suction probe measurements. Please note that the investigated measurement planes for the suction probe measurements and the LIF experiment are not identical (see Figure 3.18). Both measurements were done with the NBO burner configuration.

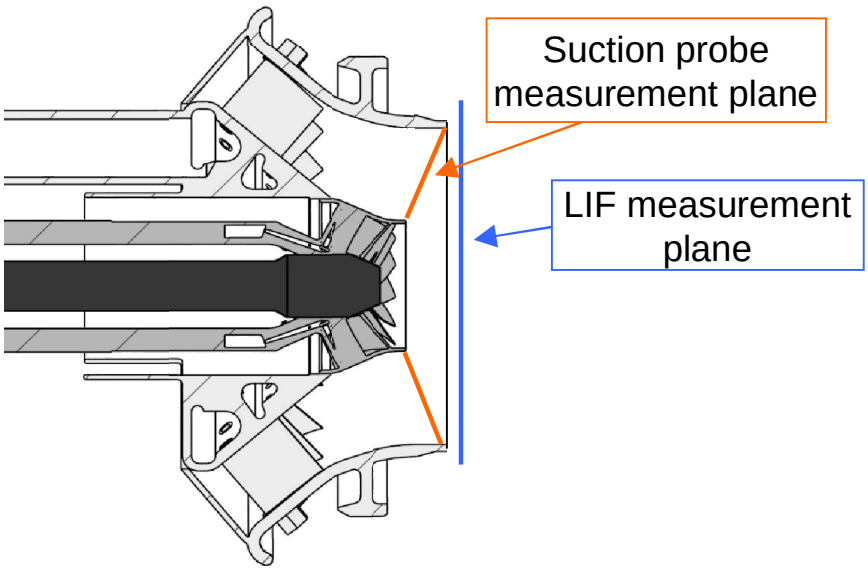

Figure 3.18: Location of LIF and suction probe measurement planes

Figure 3.19 shows the radial profiles for the baseline hardware at nominal fuel splits. The general range and shape of the measured concentrations is quite similar, but the profile from the suction probe is a bit shifted towards the premix hub (0% channel height). This may be caused by the different measurement position. It is assumed that downstream of the burner exit the swirled flow opens towards the outer side of the flow channel so that the radial profile of the suction probe would also be shifted towards the right side of the shown diagram, if it was measured at a more downstream position comparable to the LIF measurements. In contrast to the LIF-measured plane the suction probe measurements did not detect the fuel-lean area close to the premix hub (0–20%). This emphasises the assumption, that this lean area is caused by the shear-layer between the main and pilot flow which, due to the location of the measurement plane, cannot be detected with the suction probes.

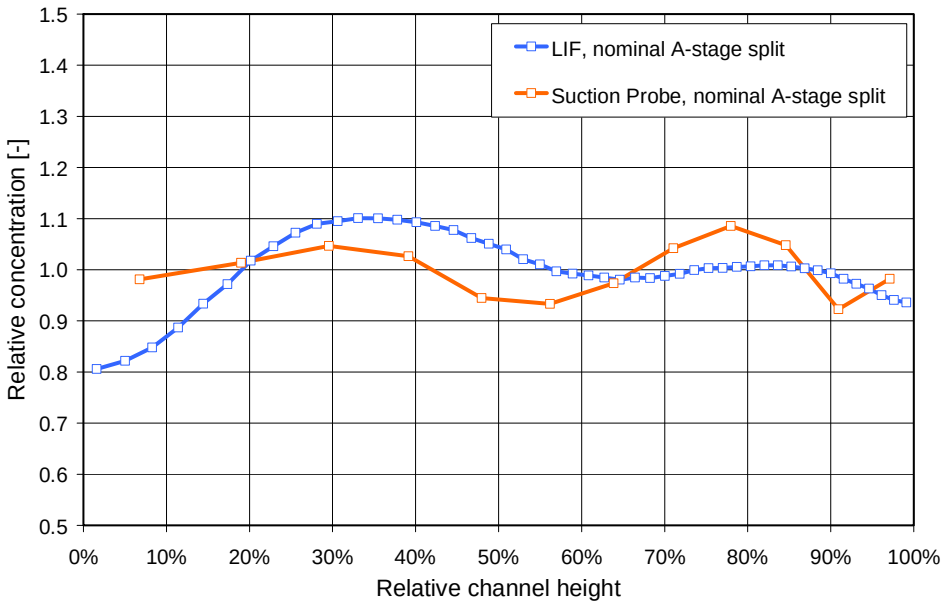

Figure 3.19: Radial profile comparison of LIF and suction probe measurement at nominal main stage split

Similar trends as for the nominal split can also be seen for the cases with main stage split variation plotted in Figure 3.20. However, the deviation of the measured concentration profiles is slightly larger; especially for the increased A-stage split case.

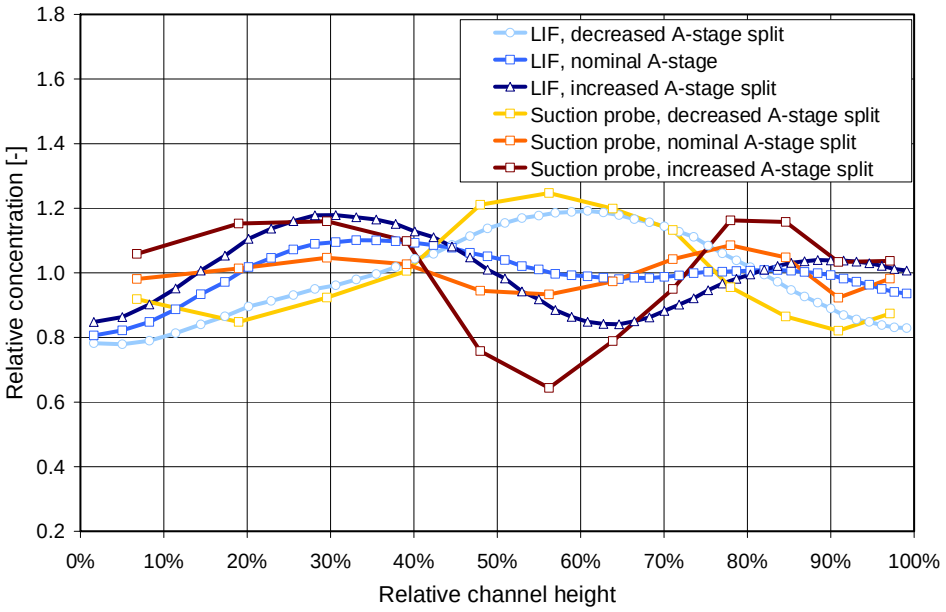

Figure 3.20: Radial profile comparison of LIF and suction probe measurement at different main stage splits

Despite the completely different measurement approach (non-intrusive vs. intrusive) and the different measurement positions, the compared profiles measured with LIF and suction probes show a quite satisfying agreement. However, this is only valid for time-averaged data, as the suction probe method does not provide any temporal information of the fuel/air mixing. Furthermore, the spatial resolution of the suction probes with 1068 investigated points for the whole main burner outlet plane is quite coarse and important effects like the increased fuel/air mixing at the pilot/main flow shear layer cannot be detected at all.

3.3.5 Comparison to Numerical Simulations

Another important aim of the LIF experiment was to generate reference data for an assessment of the accuracy of the Siemens standard fuel/air mixing simulations. As written in chapter 2.3.2, RANS CFD simulations are still widely used as standard approach in industrial applications. Hence, a steady RANS simulation was carried out with *Ansys CFX* 13.0 for the comparison with experimental results. The simulation was performed by Dr. Lukasz Panek. For turbulence modelling a Shear Stress Transport model (SST) with reattachment modification was used. The turbulent Prandtl and Schmidt numbers were set to 0.7 during the simulations. As simplification measure the fuel injection was modelled with an equal distribution for all fuel injection holes. However, the fuel injected through the PMP and the main swirler was

defined as separate but identical species to allow for better tracking of its origin in the mixing planes.

Figure 3.21 shows how the CFD model of the mixing test rig was constructed in modular form. Each part was meshed separately and brought together in CFX. Element sizes at interfaces were matched and general grid interfaces (GGI) were used to minimize errors.

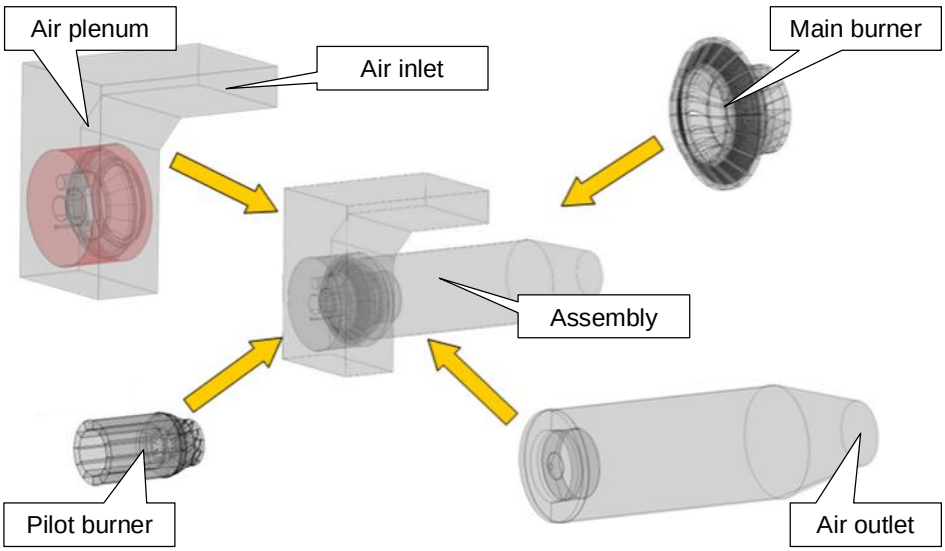

Figure 3.21: CFD model of the SGT5-4000F mixing rig

The measurements were performed at five measurement planes at different axial positions downstream of the NBO burner outlet (see Figure 3.22). For CFD additional data was obtained from a plane directly at the burner outlet. Due to reflection of Laser light at the burner hardware, experimental data for this plane is not available. The comparison of LIF and CFD at different axial positions is aimed at tuning relevant CFD parameters to correctly predict mixing at different mixing lengths and not only for a single reference position. The respective distances x_i from the burner outlet plane to the single measurement planes were defined as (normalised by the burner outlet diameter D):

Plane 0: $x_0/D = 0.000$ (CFD only)
Plane 1: $x_1/D = 0.047$
Plane 2: $x_2/D = 0.093$
Plane 3: $x_3/D = 0.163$
Plane 4: $x_4/D = 0.256$
Plane 5: $x_5/D = 0.349$

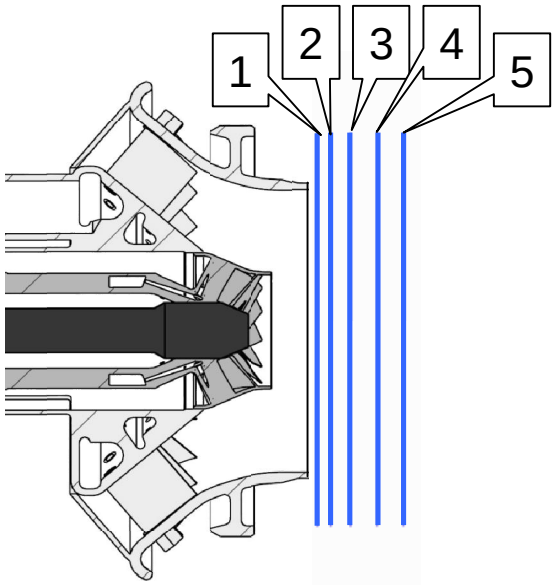

Figure 3.22: Location of the five measurement planes for LIF and CFD comparison

Figure 3.23 shows the post-processed LIF and CFD images of the baseline hardware at nominal fuel split. To ease the comparison of LIF and CFD images, all images were converted to an identical colour map using the image visualisation tool *Tecplot*. All images are looking against flow direction. Unless otherwise stated, all presented results refer to the first axial measurement plane 1.

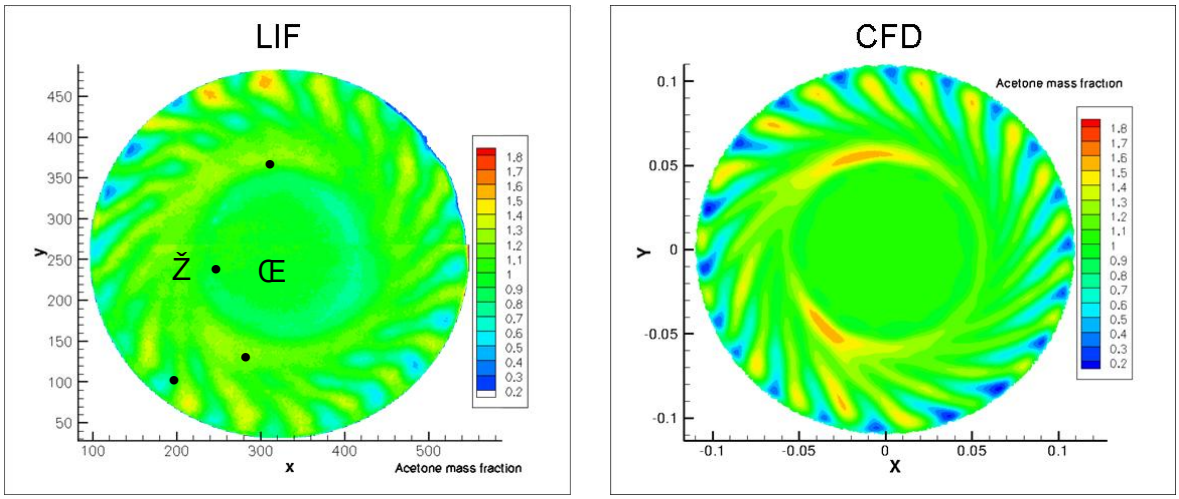

Figure 3.23: Images of LIF/CFD mixture field for NBO burner base load reference case

Compared to the LIF image (left hand side) the CFD image (right hand side) shows generally a slightly worse fuel/air mixture. However, the general fuel/air distribution of the experiment and the CFD match quite well. For example, the well mixed pilot region (Œ), the fuel-lean and fuel-rich rings (• & Ž), and the vane profiles (•) can be seen in the LIF and the CFD

image – though not to the same extend. This may at least to some extend be caused by the used modelling approach of an equally distributed fuel injection for all fuel injection holes. The two fuel-rich pockets (•) in the fuel rich ring can be identified in the LIF as well as in the CFD image. These rich pockets are caused by an air deficit in that region resulting from two strong air recirculation zones upstream of the burner in the lower left and right corner of the air plenum. Due to the swirl, they occur in the measurement plane at rotated positions.

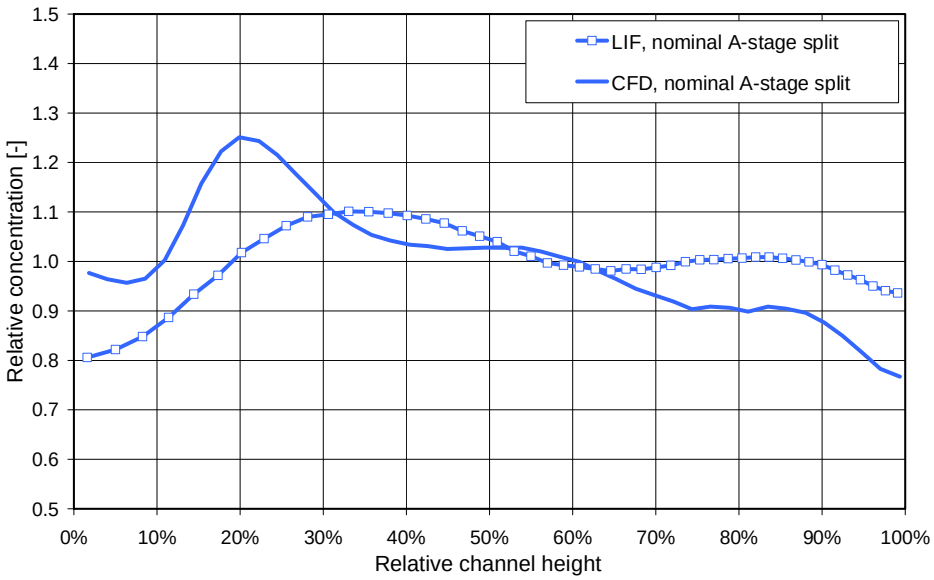

Figure 3.24: Radial profile comparison of LIF and CFD for NBO burner base load reference case

Figure 3.24 shows a comparison of the radial fuel profile of the main burner passage derived from experiment and CFD. It can be seen that the CFD profile is dominated by the rich ring close to the burner hub. Especially the two rich pockets (cf. • in Figure 3.23) increase the values of the circumferentially averaged profile in this region. The lean ring identified in the experimental data (0 – 20% relative channel height) is not present in the CFD profile. Furthermore, the CFD profile towards the burner cone (> 65% channel height) is leaner compared to the experiment. This may partly be caused by the fact that all values of a radial fuel profile were normalised to a mean value of 1, so that for the CFD the two rich pockets also lead to a relative decrease of the other values. However, the general differences in the radial profiles from experiment and CFD could already be seen in Figure 3.23.

The respective histograms are shown in Figure 3.25. The CFD histogram (right hand side) shows a thinner and higher peak at 1. The second peak above 1 is also present, but less pro-

nounced. Generally, the spread of counted values in the CFD is wider, especially for values below 1.

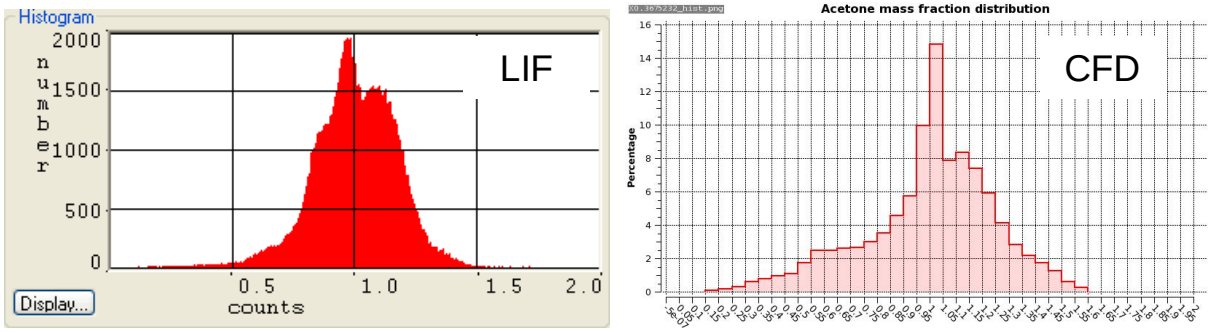

Figure 3.25: Histograms of LIF and CFD mixture field for NBO burner base load reference case

Figure 3.26 additionally shows the radial profile from the suction probe measurements. Despite differences like the measurement approach and the investigated measurement plane the agreement of the two measured profiles is better than with the CFD simulation.

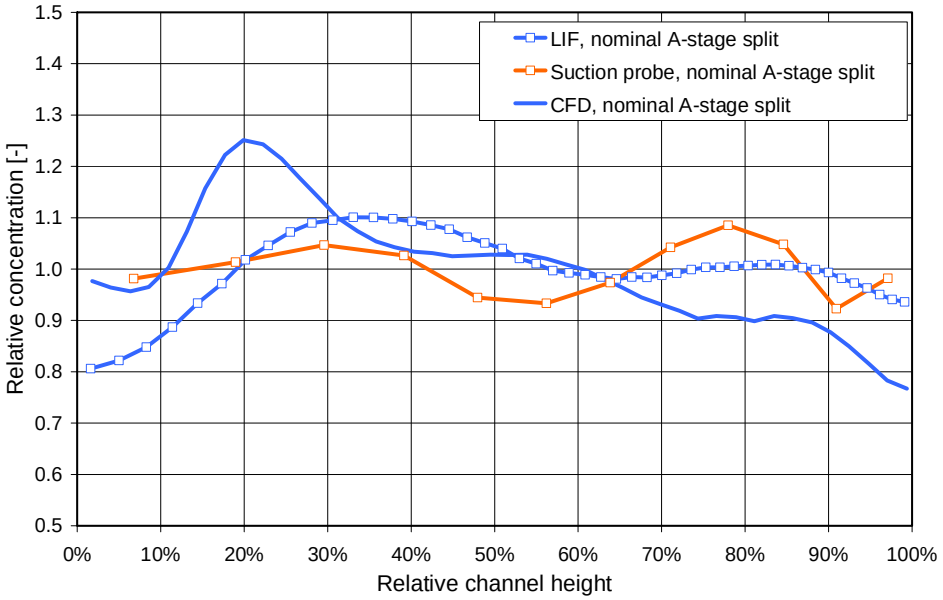

Figure 3.26: Radial profiles for NBO burner reference case from LIF, suction probe and CFD simulation

Table 3.4 shows LIF and CFD images of the NBO burner at different A-stage splits. Again, the staging effect is clearly visible: Increased A-stage causes the fuel rich ring to move towards the centre of the main burner, whereas at an increased A-stage fuel split a lean ring in the centre of the main burner occurs due to shifting more fuel to the inner and outer radius.

Main stage split	LIF	CFD	Map
Decreased A-stage	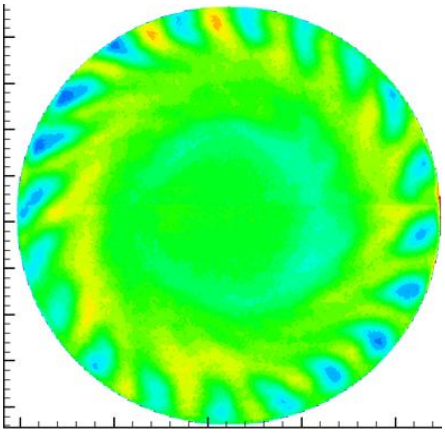	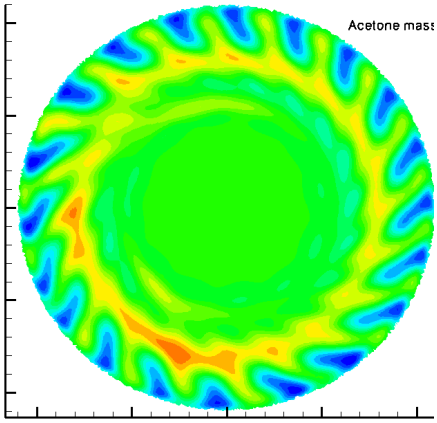	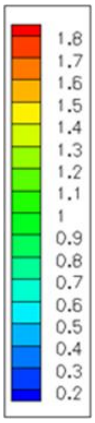
Nominal splits	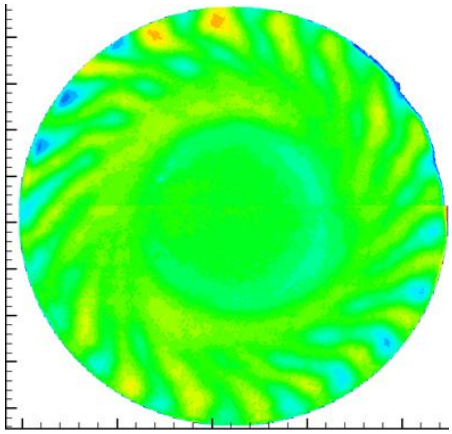	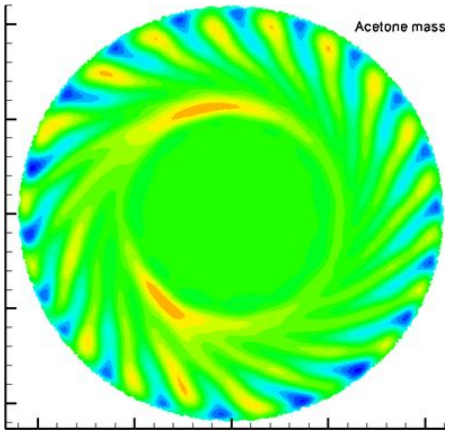	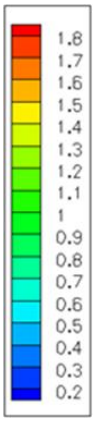
Increased A-stage	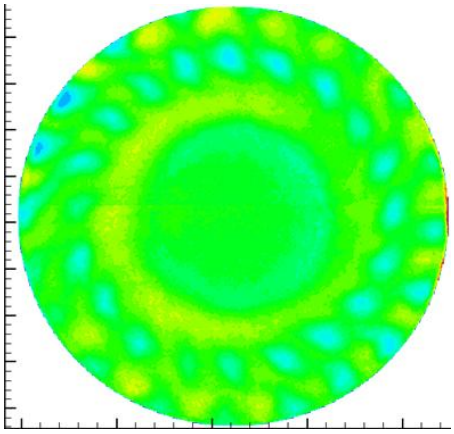	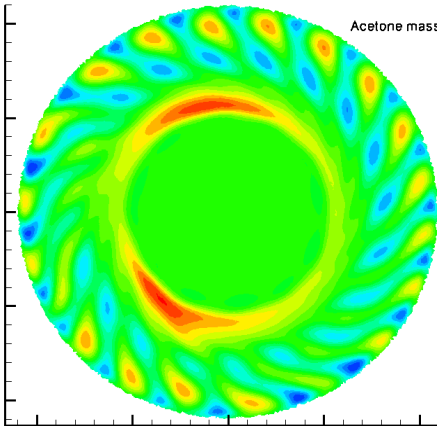	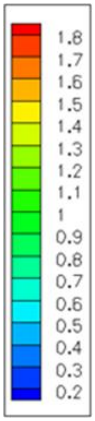

Table 3.4: LIF and CFD images of the main stage split variation for the NBO burner

The corresponding histograms for the different A-stage splits are shown in Table 3.5. Compared to the nominal split the decreased A-stage case shows an increased second peak at values above 1. The case with increased A-stage on the other hand shows a slightly better profile

in terms of a higher number of values around 1, indicating that this case might have potentially lower NO_x emissions.

Main stage split	LIF	CFD
Decreased A-stage	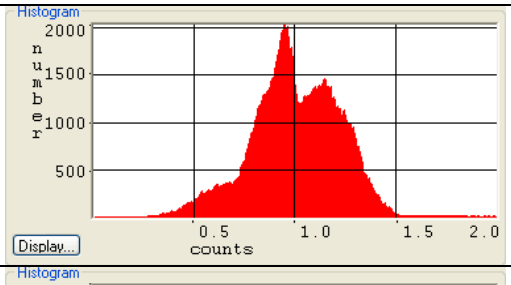	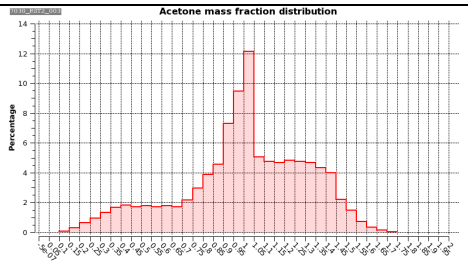
Nominal splits	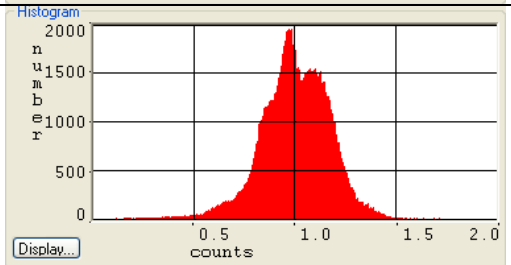	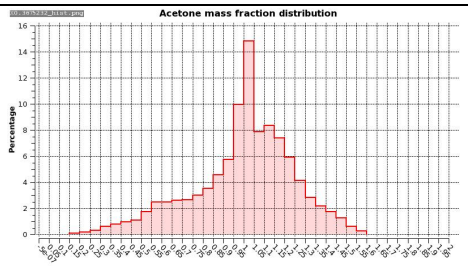
Increased A-stage	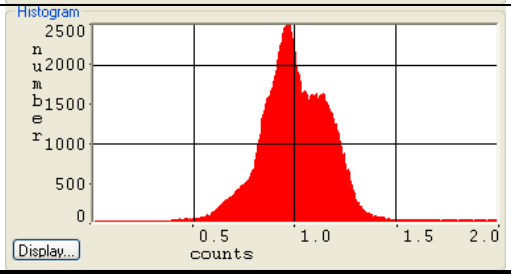	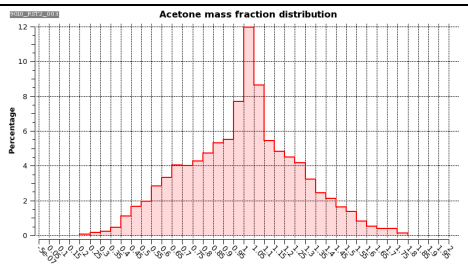

Table 3.5: Histograms from LIF and CFD of the main stage split variation for the NBO burner

For reasons of clarity, Figure 3.27; Figure 3.28 and Figure 3.29 at first show the radial profiles derived from LIF and CFD for nominal, decreased and increased A-stage split separately. Afterwards, Figure 3.30 shows the comparison of the radial profiles from all three cases in one plot. It can be seen that the profiles from CFD are dominated by the rich ring close to the premix hub. Moreover, the CFD predicts a significantly higher effect of the A/B staging on the radial fuel profile.

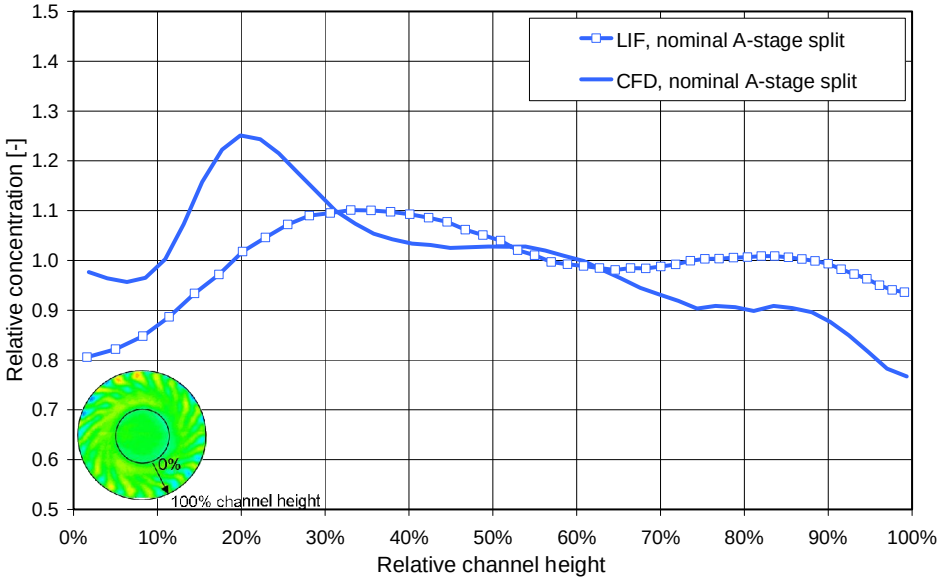

Figure 3.27: LIF and CFD radial profiles at nominal A-stage split

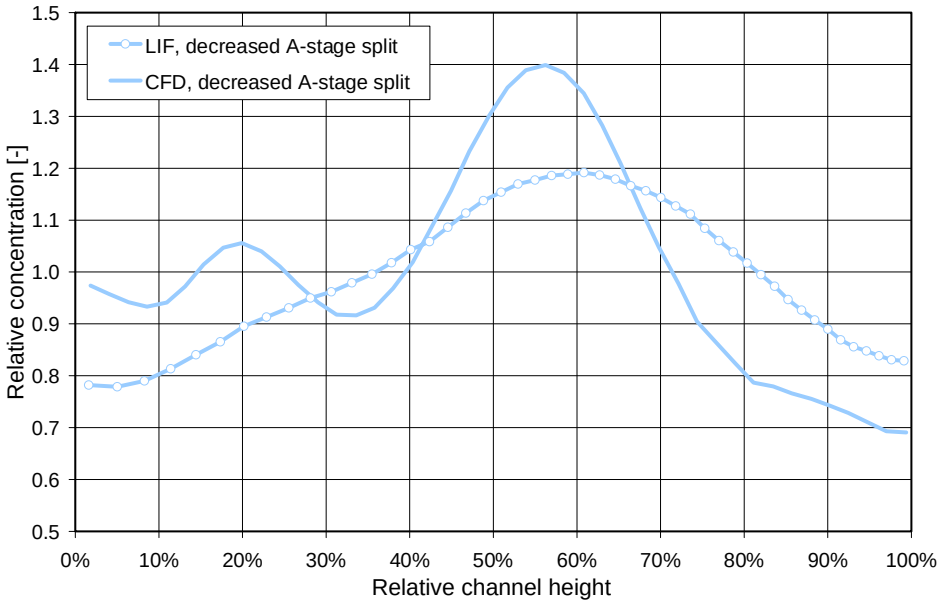

Figure 3.28: LIF and CFD radial profiles at decreased A-stage split

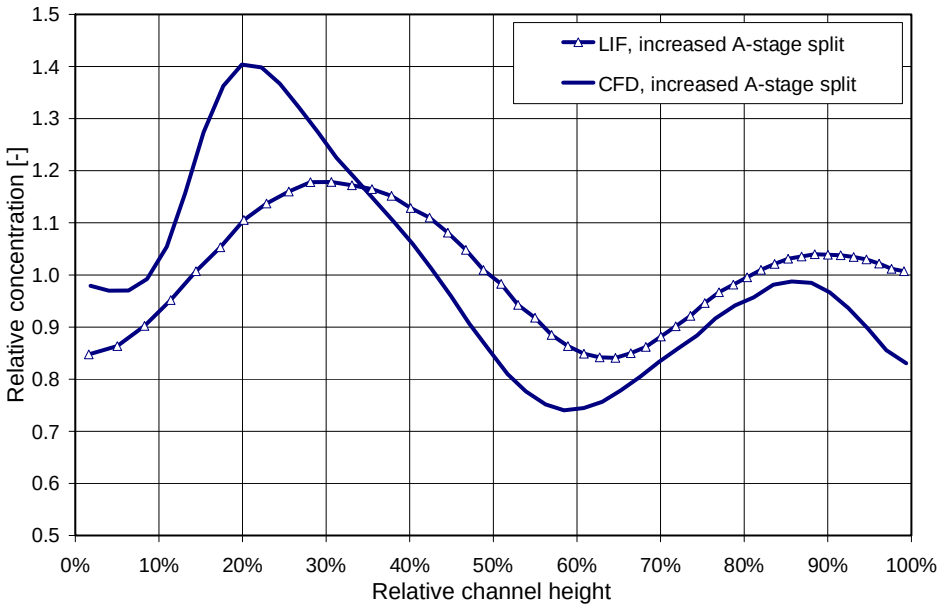

Figure 3.29: LIF and CFD radial profiles at increased A-stage split

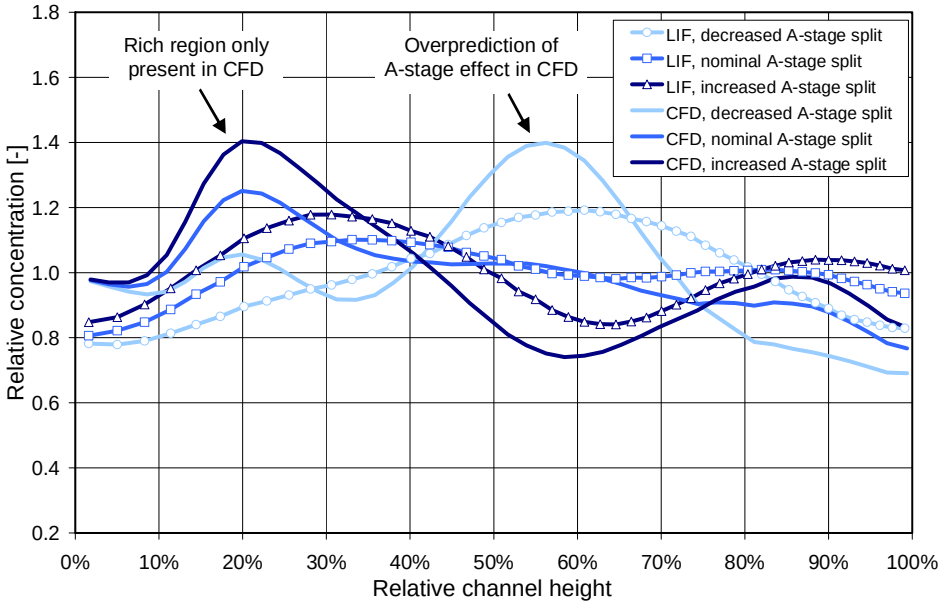

Figure 3.30: Summary of LIF and CFD radial profiles at different A-stage splits

Measurement plane	LIF	CFD	Map
0	Not possible	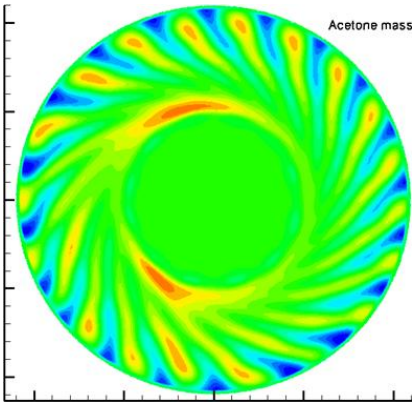	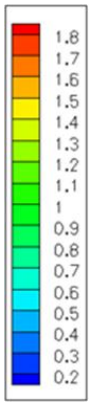
1	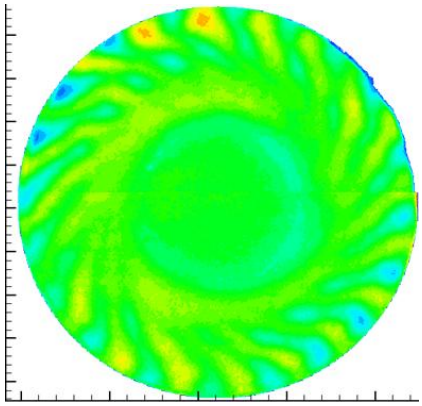	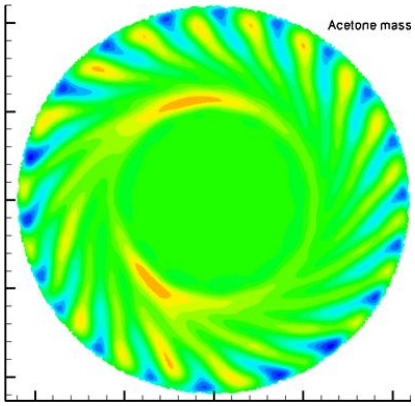	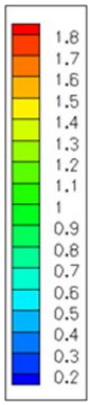
2	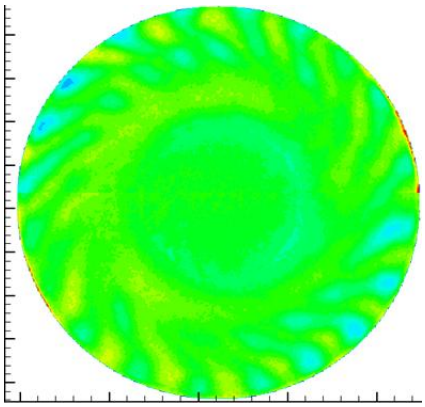	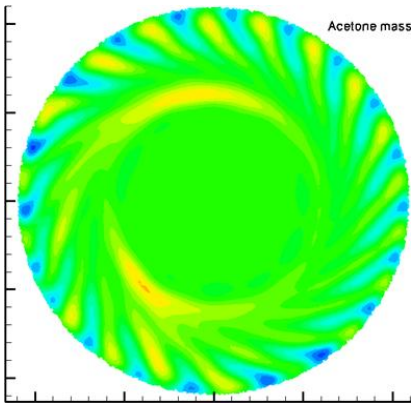	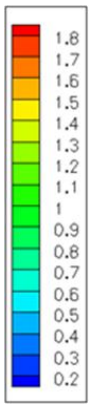
3	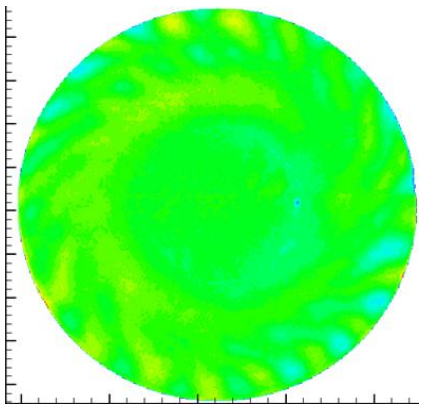	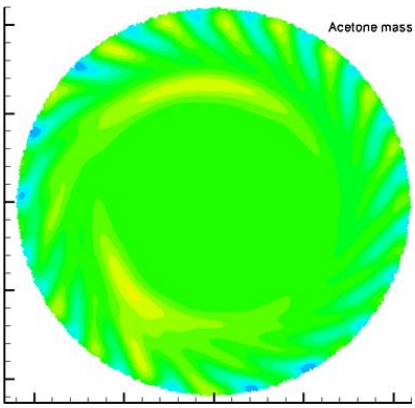	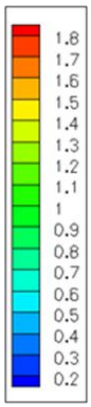

Measurement plane	LIF	CFD	Map
4	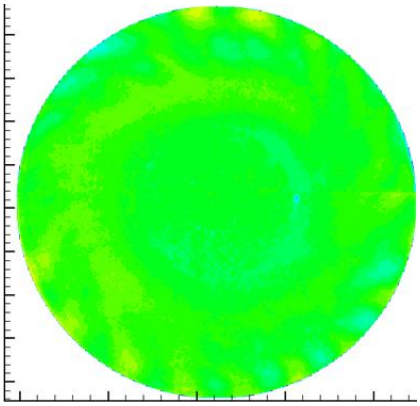	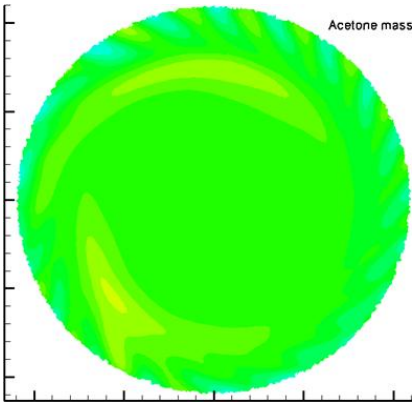	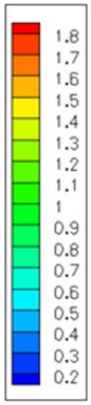
5	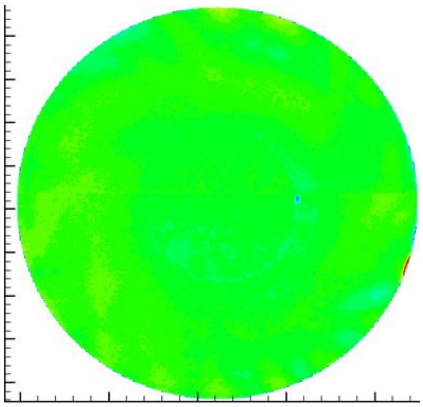	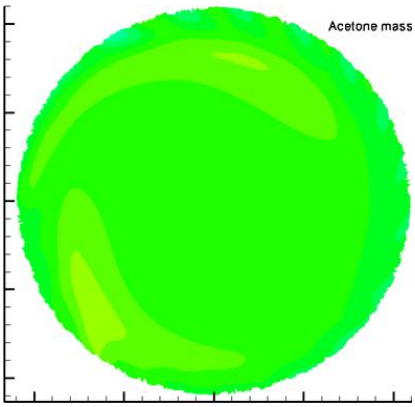	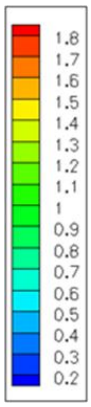

Table 3.6: LIF and CFD images for nominal A-stage split at different axial measurement positions

Table 3.6 shows the LIF and CFD images of the NBO burner at nominal A-stage split recorded at the five different axial measurement positions. The fuel/air mixture along the flow path develops as expected and with increasing mixing length becomes more and more homogeneous. The tendencies and general structures in the LIF and the CFD images show a satisfying agreement. However, the previously observed tendency of the CFD predicting slightly worse mixing can be seen at all axial positions along the flow path.

Similar tendencies in the change of the histogram shapes for the experiment and the simulations at the different axial positions can also be observed in the respective histograms in Table 3.7. As one could expect, with increasing mixing length the histogram shape for LIF as wells as CFD becomes thinner and higher with an increasing peak around values of 1.

Measurement plane	LIF	CFD
0	Not possible	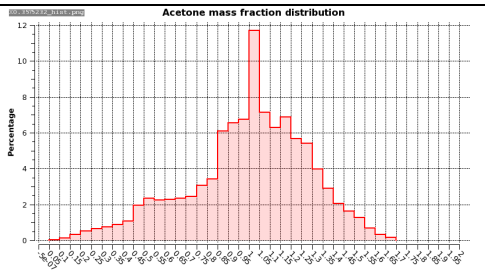
1	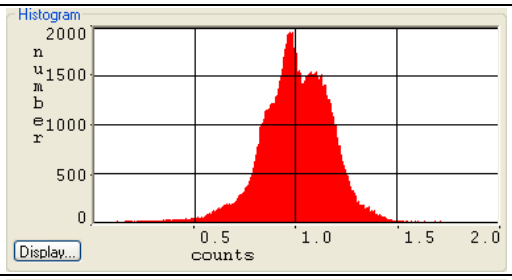	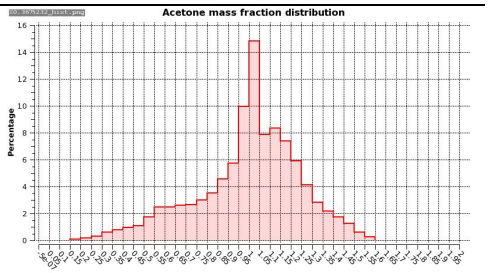
2	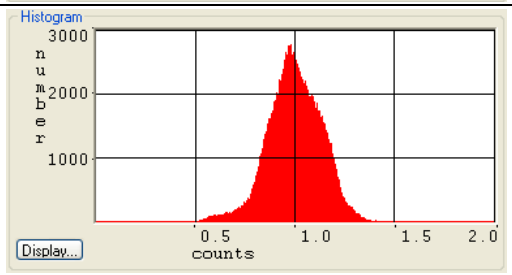	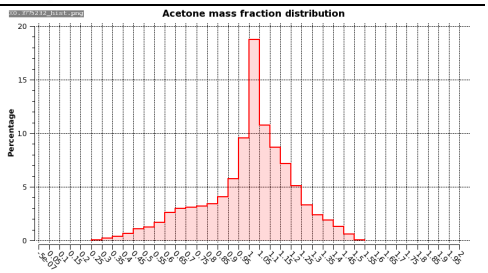
3	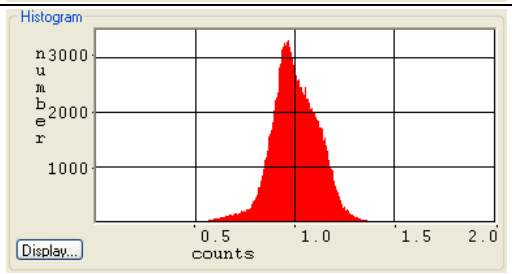	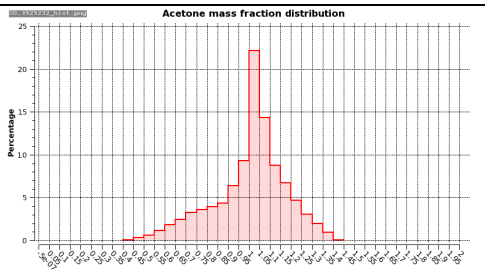
4	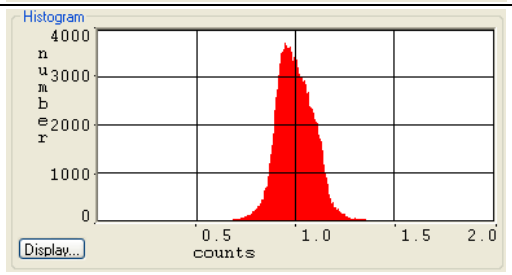	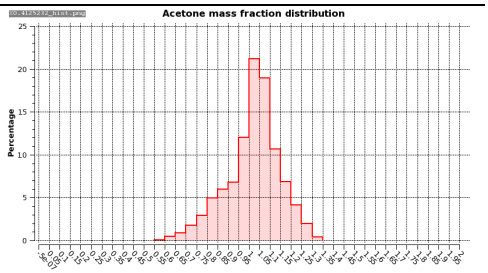
5	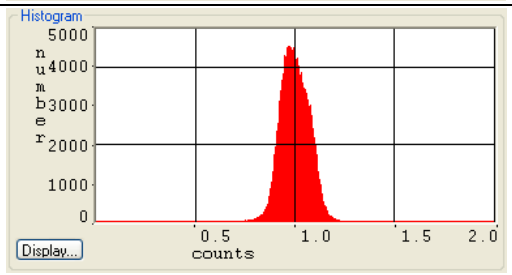	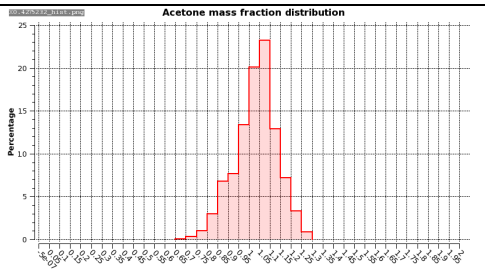

Table 3.7: Histograms from LIF and CFD for nominal A-stage split at different axial measurement positions

To quantify the mixing enhancement with increasing mixing length, the global standard deviation for each averaged image for the LIF experiment and the CFD simulation was calculated. The standard deviation may be interpreted as a measure for the global mixing quality with a value of 0 corresponding to a completely homogeneous fuel/air distribution.

The calculated standard deviations for CFD and experiment at the different axial positions are shown in Figure 3.31. Unfortunately, experimental data at different mixing lengths was only recorded with nominal A-stage split. However, a comparison of the available LIF and CFD data at the reference measurement plane 1 (x/D = 0.0465) shows a systematic offset of the CFD simulations for all three cases. This offset corresponds to the slightly worse mixing quality present in all CFD simulation results discussed in this thesis and can most probably be contributed to an underprediction of the mixing directly at the point of fuel injection caused by the RANS modelling approach. Furthermore, it can be seen that the nominal split case provides the better fuel/air mixture compared to the other two cases. However, the difference between the increased and nominal A-stage split in the experiment is much smaller than in the CFD data.

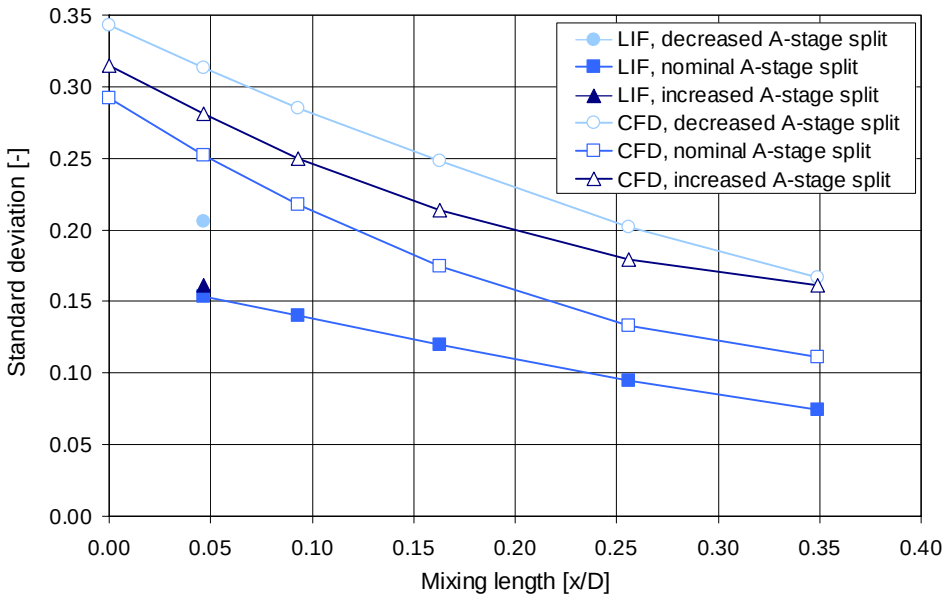

Figure 3.31: Standard deviation along flow path (axial position)

Another criterion for the comparison of LIF and CFD is the “slope” of the mixing quality with increasing mixing length. It can be seen that the slope from the experiment is smaller than from CFD. In this context it is particularly noticeable that the slope for the increased A-stage

split in the CFD simulation is significantly different compared to the other two cases. However, a scientific explanation for this phenomenon can currently not be given.

A potential optimisation measure for the RANS mixing simulations is to change this slope by an adaption of the turbulent Prandtl number (in Ansys CFX the turbulent Prandtl number is identical to the turbulent Schmidt number). Hence, the CFD simulation of the nominal split case was repeated with a turbulent Prandtl number of 0.4. A comparison of the standard deviation derived from this simulation with the LIF experiment and with the baseline CFD simulation using a turbulent Prandtl number of 0.7 is shown in Figure 3.32. Although it is not expected that with an adjusted Prandtl number a more realistic simulation directly at the point of the fuel injection can be achieved, it can be seen that using the modified Prandtl number led to a significant improvement of the CFD simulation.

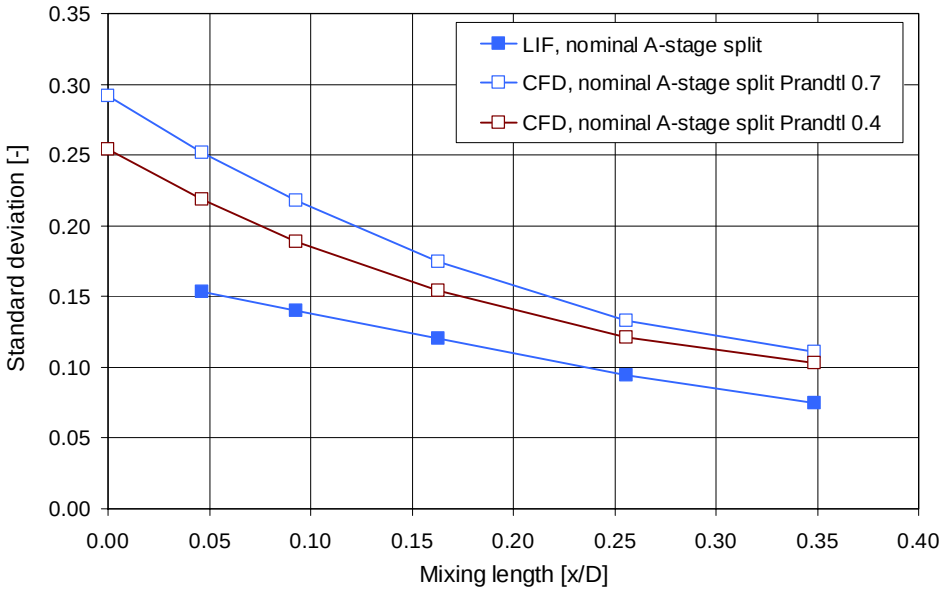

Figure 3.32: Standard deviation along flow path for LIF and CFD simulations with turbulent Prandtl numbers of 0.7 and 0.4

3.4 Setup and Results for the SGT6-8000H Combustor

This chapter deals with the LIF experiments conducted at Siemens SGT6-8000H combustors. The SGT6-8000H engine was introduced in 2012 and is equipped with 12 advanced Ultra-low NO_x Combustion Systems (ULN) with individual can combustors. The base power output at ISO conditions is 274 MW with a pressure ratio of 19.5 and a gross efficiency of 40%. Figure

3.33 shows a principal sketch of the GT mid-frame section with installed 8000H burner and can.

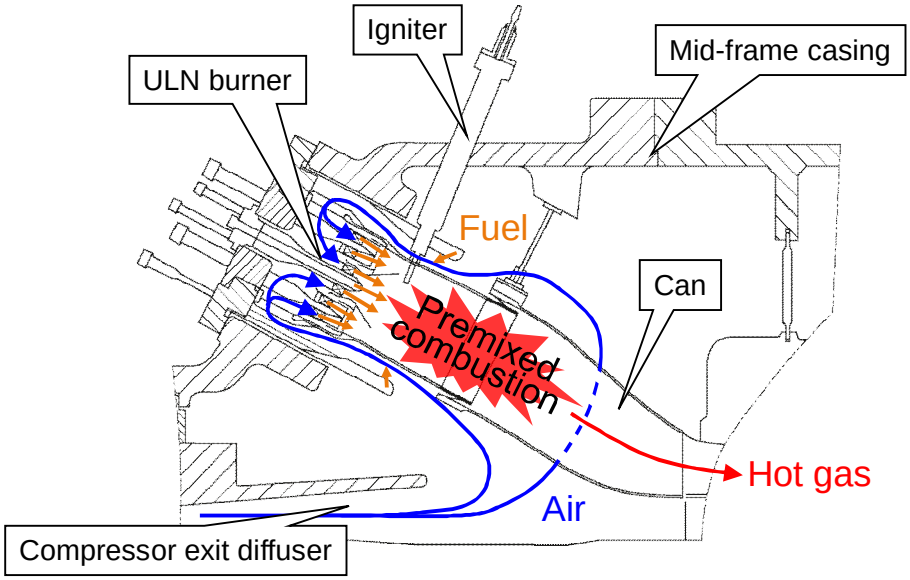

Figure 3.33: Principal sketch of a SGTX-8000H mid-frame section

Like the Hybrid burner the ULN burner is a swirl-stabilised lean premixed combustion system with a central pilot burner. The main parts of the ULN burner are the flow sleeve, the cover plate, the basket, the support housing with eight individual main swirlers, and the pilot swirler with the centrally installed pilot oil stick. The principal design of the ULN burner with the main components is shown in Figure 3.34. For more details of the ULN burner design please refer to [53] and [54].

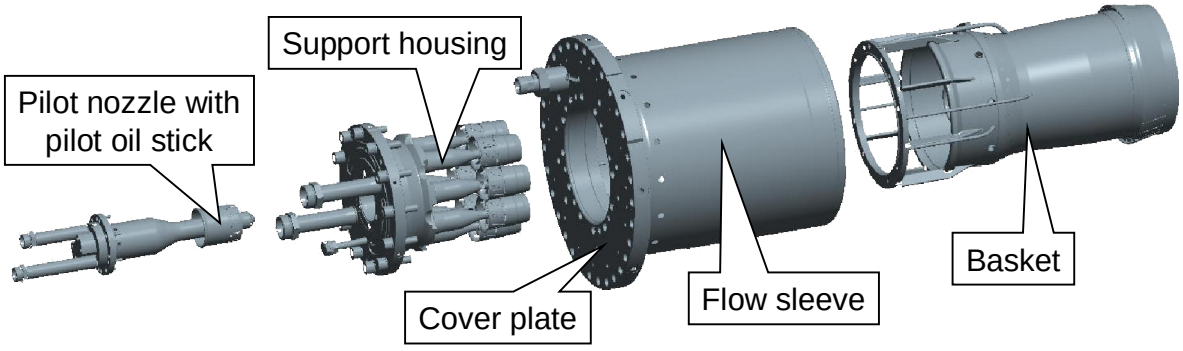

Figure 3.34: Main ULN burner components

The ULN burner features five independent natural gas stages to allow flexible operation and tuning regarding emissions and dynamics. Figure 3.35 shows the principal location of the five natural gas stages. The main fuel gas is injected through holes in the main swirler vanes (A-

and B-stage). The circumferential arrangement of these two premixed stages is shown in the lower right corner of Figure 3.35. The third premixed fuel gas stage is located upstream at the flow sleeve inlet. The central pilot features a premixed stage (D-stage) and a diffusion stage (pilot-stage). Furthermore, the ULN burner features three different premixed fuel oil stages.

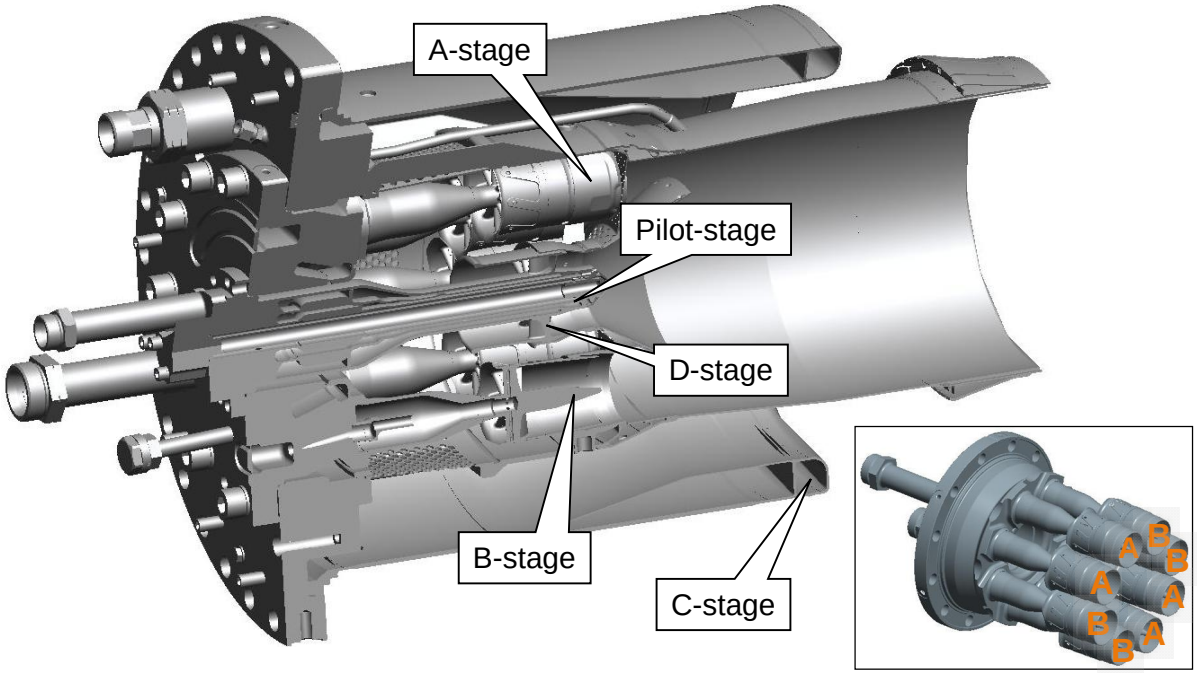

Figure 3.35: ULN burner with five natural gas stages

Details of the setup for LIF experiments at the SGT6-8000H combustor are given in chapter 3.4.1. The testing procedure is described in chapter 3.4.2. Finally, exemplary test results are presented and discussed in chapter 3.4.3.

3.4.1 Experimental Setup

For the LIF experiments with the ULN burner a special optical test rig with a full-scale SGT6-8000H single burner mid-frame section was designed. Due to the integration of the complete mid-frame geometry including flow relevant features like the compressor exit diffuser, this test rig also allows the investigation of important effects on the fuel/air mixture like an inhomogeneous air inflow at the burner inlet as it may occur in a real engine, for example.

Major parts of the new rig were made of acrylic glass fixed at an aluminium frame carrying the combustor load. A sketch for the SGT6-8000H test rig is shown in Figure 3.36. As can be seen the air enters the test rig from the left and exits through the flow channel on the right end

of the test rig. Since the test rig was operated in suction operation mode, the exit was connected to the air supply line in the flow lab. The four guiding arms at the upper left end of the test rig were used to support a fast and safe installation of the combustor hardware.

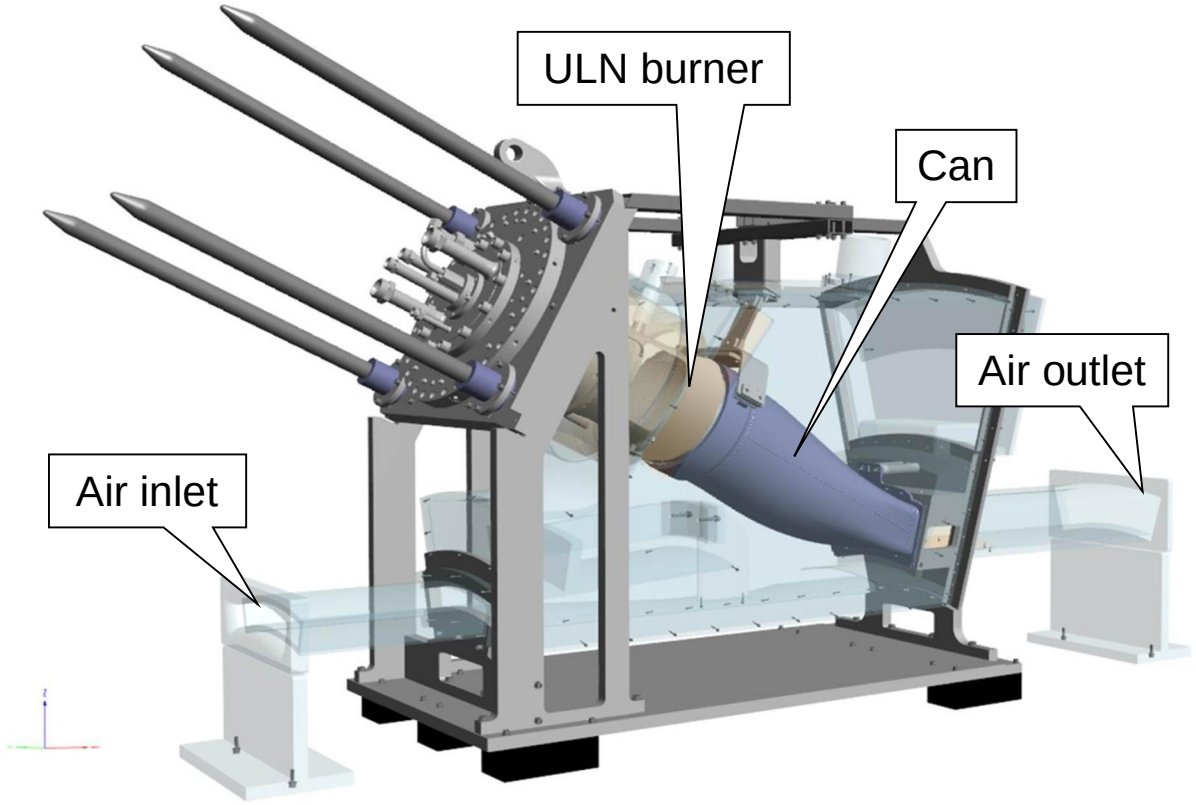

Figure 3.36: SGT6-8000H cold flow test rig

However, compared to the 4000F test rig, providing optical access to the ULN combustor was much more complex because three parts had to be designed with windows: the test rig, the flow sleeve, and the basket. The respective parts of the test rig were made of the special UV-transparent acrylic glass already introduced for the SGT5-4000F optical test rig. The flow sleeve was replaced by a part completely made of UV-transparent acrylic glass having the identical geometry as the original metal part and including the fully operational integrated C-stage. The basket had to be equipped with windows of only 3 mm thickness to ensure identical flow behaviour as the original part. Hence, a concept with three asymmetrically arranged windows was chosen providing sufficient mechanical integrity while allowing the sequential investigation of the whole burner outlet plane by a 180° rotation of basket (see Figure 3.37).

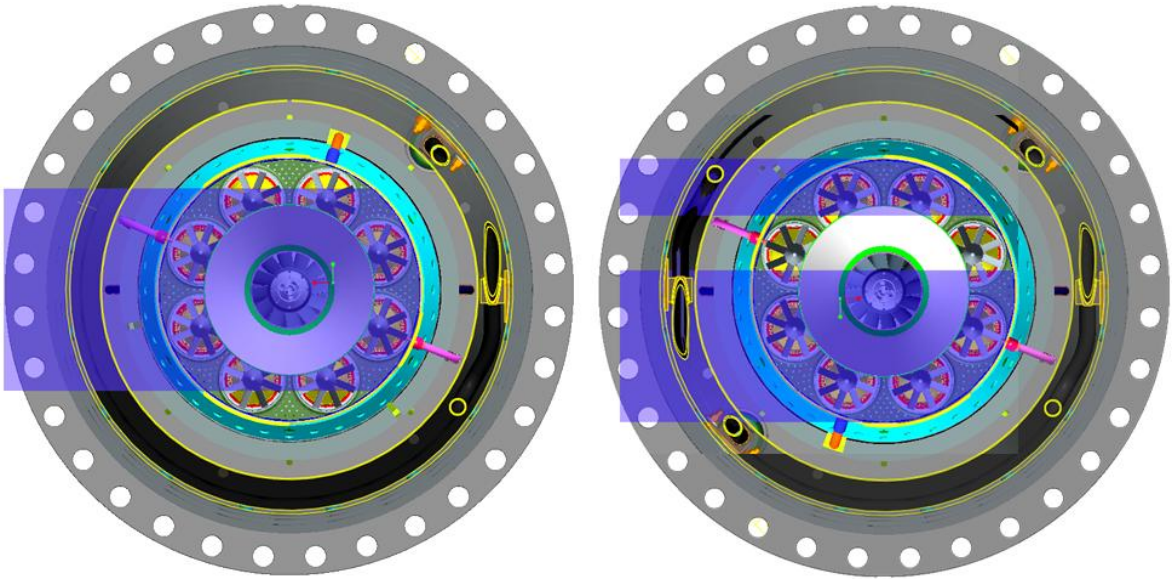

Figure 3.37: ULN burner with indicated laser sheet; installed in standard position (left hand side) and turned by 180° (right hand side)

The pictures shown in Figure 3.38 give an impression of the excellent optical access to the whole mid-frame (left hand side) and the combustor (right hand side).

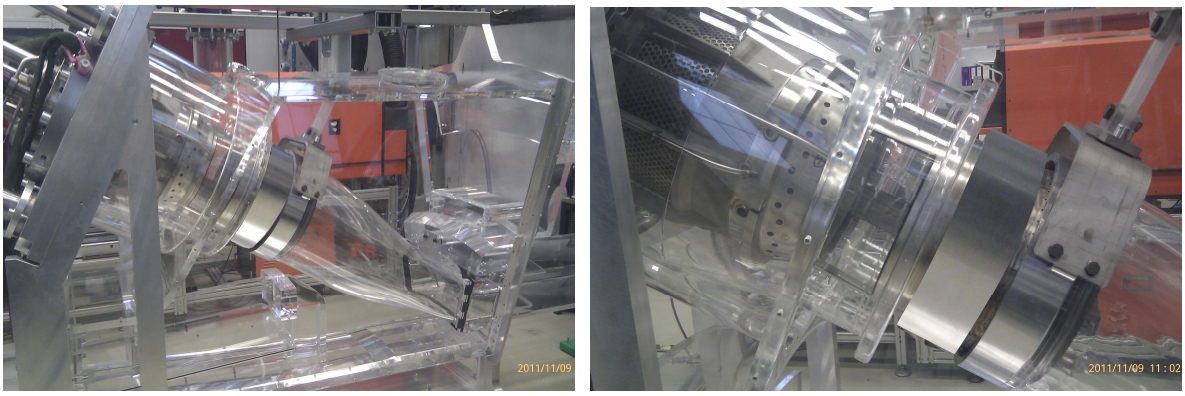

Figure 3.38: SGT6-8000H cold flow test rig with installed ULN hardware

3.4.2 Testing Procedure

Similar to the previously described SGT5-4000F experiments the investigated boundary conditions for the SGT6-8000H combustor are related to real engine base load and part load conditions with additional fuel gas staging variations at selected measurement points. However, due to the increased number of investigated parameter combinations with now four fuel stages (A-, B-, C-, and D-stage; the diffusion pilot (P-stage) was not investigated), the illustration of the investigated boundary conditions in a 3-D plot is not feasible here.

Due to the limitation of the tracer gas mixing facility to three lines and a total mass flow of about 90 g/s, single fuel stages and different fuel-stage combinations were measured sequentially. Theoretically, this procedure might affect the test results, e.g. due to a different air distribution caused by changed flow resistance when fuel is not injected at all stages simultaneously. To investigate the significance of such effects, selected fuel stages were recorded sequentially and simultaneously for comparison. Figure 3.39 shows the sequentially measured A- and B-stage and the A+B stage assembled in post-processing. The comparison of the assembled and the measured A+B stage images is shown in Figure 3.41. The procedure was repeated for A- and D- instead of the A- and B-stage (Figure 3.40 and Figure 3.42).

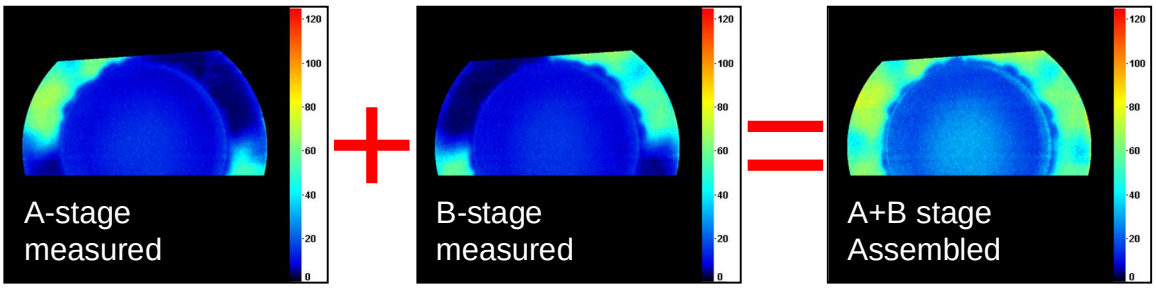

Figure 3.39: Assembling of a an A+B stage image by adding sequentially measured A- and B-stage images

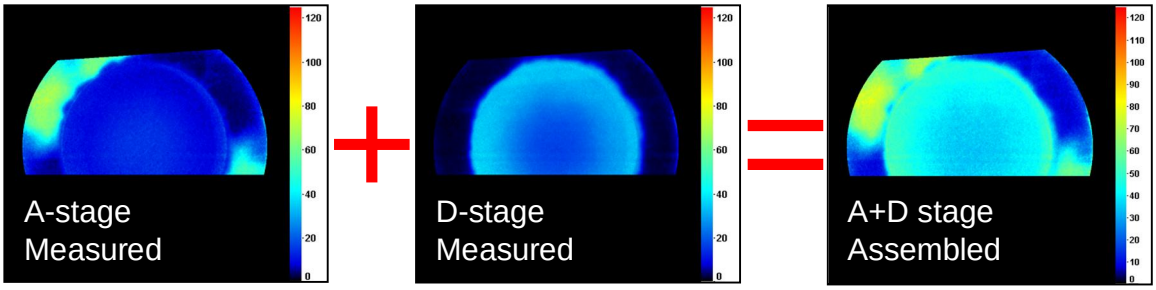

Figure 3.40: Assembling of a an A+D stage image by adding sequentially measured A- and B-stage images

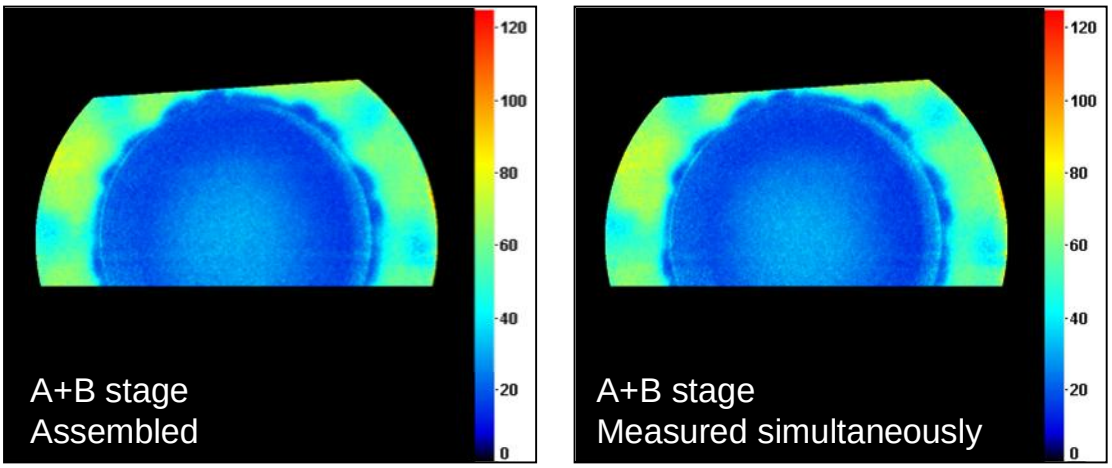

Figure 3.41: Comparison of sequentially measured and assembled A+B stage with simultaneously measured A+B stage

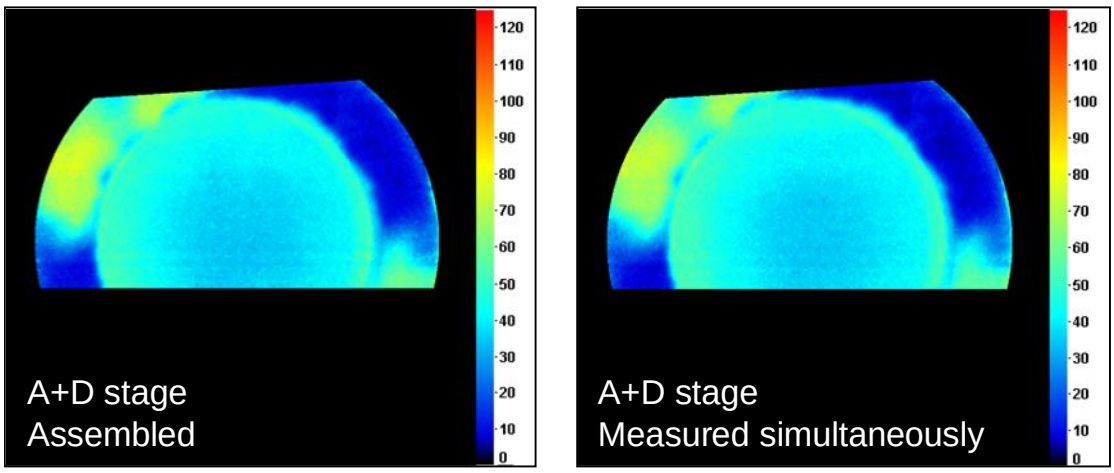

Figure 3.42: Comparison of sequentially measured and assembled A+D stage with simultaneously measured A+D stage

In Figure 3.41 and Figure 3.42 only minor differences for the afterwards assembled and measured cases can be identified. This leads to the assumption that separate measurements of single fuel stages are valid and the effect e.g. of a different air split is below the measuring resolution of the experimental setup.

As described in chapter 3.2, the tracer gas was a mixture of acetone as fluorescing marker and nitrogen as carrier gas. During testing with the ULN combustor the amount of acetone was adjusted to increase the signal-to-noise ratio (high acetone content) while staying within the limits of the mixing station (10 g/s) and without risking condensation of acetone (above 30% acetone). As a result, the optimal acetone concentration for the single fuel stages and their combinations was different (see Table 3.8).

Fuel stage	A	B	C	D	A + B	A + C	A + D
Acetone content [% by volume]	**10**	**10**	**30**	**30**	**6.5**	**10**	**10**

Table 3.8: Acetone content for different fuel stages

However, the direct comparison of the different fuel stages required a known correlation of acetone concentration and fluorescence signal to correct the images to an identical reference concentration during image post-processing. In the present case the fluorescence signal increased proportionally to the acetone concentration. Figure 3.43 shows an example of the linear correction of image A to the acetone concentration level of image B. After correction, the average intensity of the images was 1.13341 for image A and 1.13758 for image B which is equivalent to a deviation of 0.37%.

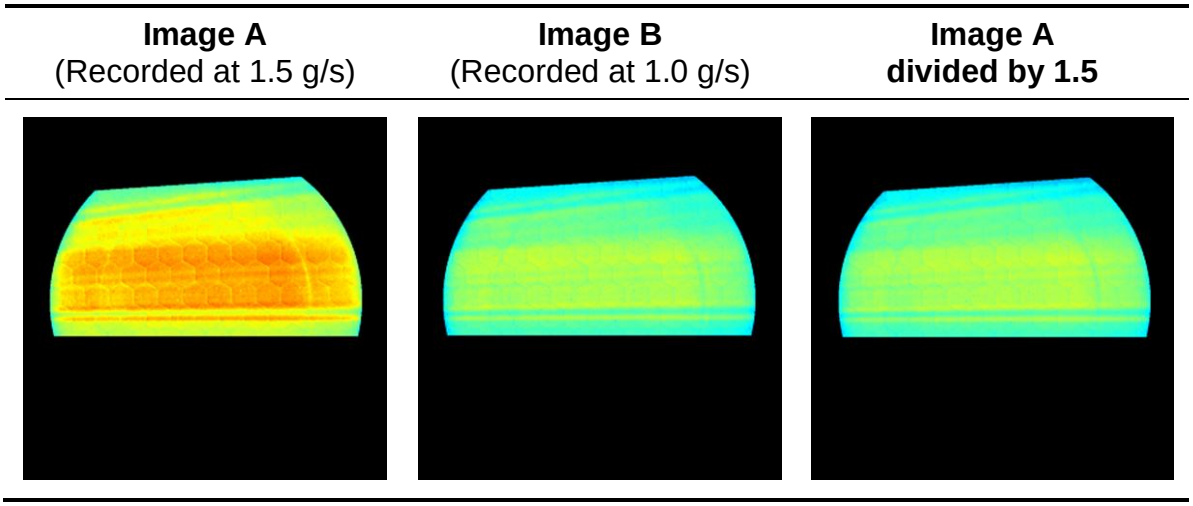

Figure 3.43: Typical example for the correction of different acetone concentrations to an identical reference level

To simplify the correction procedure, the target values listed in Table 3.8 and not the actually measured acetone concentration for each image was used for post-processing. The deviation of the measured values and the target values was always below ± 1.5% (cf. Appendix A). Therefore, this simplification did not lead to a significant error.

3.4.3 Results and Analysis

Figure 3.44 shows typical examples of post-processed single images of the ULN reference burner D-stage at base load reference conditions. It can be seen that the mixture field of the

D-stage significantly changes from image to image. Generally, the most fuel is shifted towards the outer diameter of the pilot cone whereas the inner pilot zone only shows significant amounts of fuel occasionally.

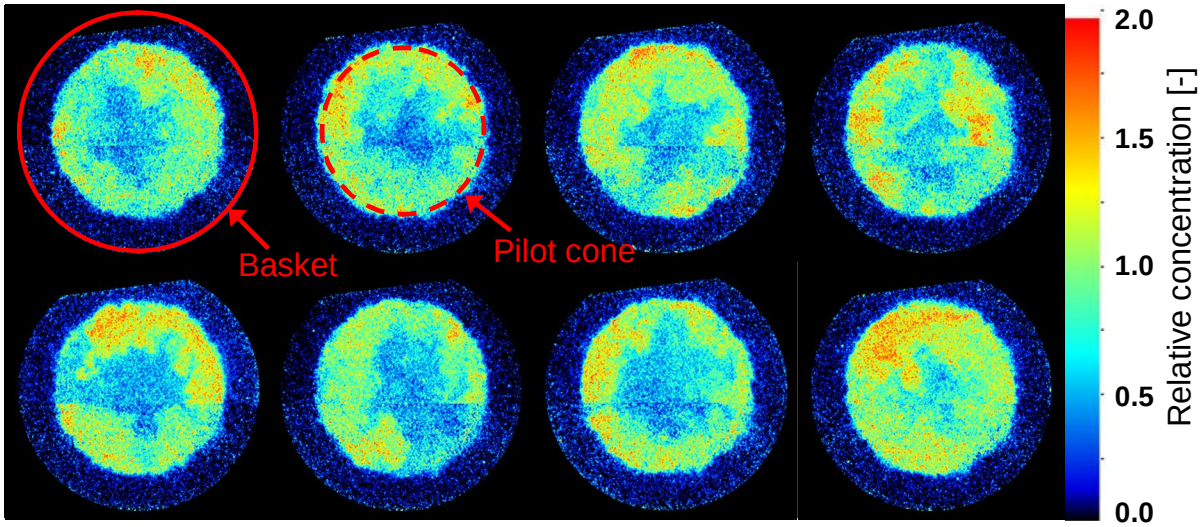

Figure 3.44: Selection of typical single images of ULN 2.0 D-stage base load reference case

Figure 3.45 shows the respective averaged and STD image for the D-stage reference case. In the averaged image on the left hand side one can see that the pilot fuel is mainly concentrated towards the outer diameter of the pilot cone. The fuel-lean area in the centre is most probably caused by dilution with air recirculating in the inner recirculation zone. The pilot area is surrounded by a small amount of fuel recirculating into the area of the main swirlers.

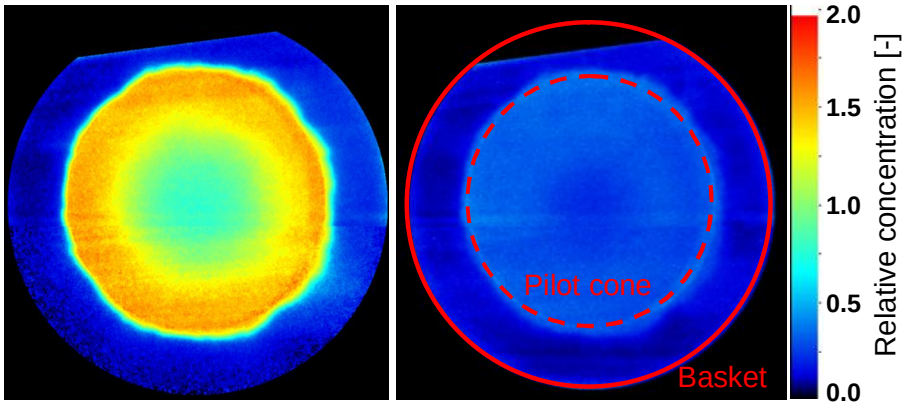

Figure 3.45: Averaged (left) and STD image (right) of ULN 2.0 D-stage base load reference case

The standard deviation shown in the image on the right hand side is significantly lower than the values of the averaged or single images. This means that the single-image to single-image fluctuations of the mixture profile are comparably low. Thus, it can be assumed that the ULN pilot has a temporally quite steady mixture profile. However, in both images slight stripes can be identified. These stripes are most probably artefacts from the post-processing with the 2-D laser energy distribution.

In Table 3.9 LIF images of the ULN reference burner and a variant slightly modified air flow conditioner recorded with different D-stage mass flows are presented. The respective D-stage split is expressed as a percentage amount compared to total fuel mass flow. It can be seen that the D-stage fuel distribution of the two presented ULN burner versions does not significantly differ. Hence, it can be assumed that the D-stage fuel injection is quite robust against minor changes of the air inflow. However, it can be seen that the tracer LIF measurements were sensitive enough to reliably detect the comparably small changes of the adjusted tracer gas mass flow for the different measurement points.

D-stage Sweep

D-stage	ULN reference	ULN variant A	Map
11.0%	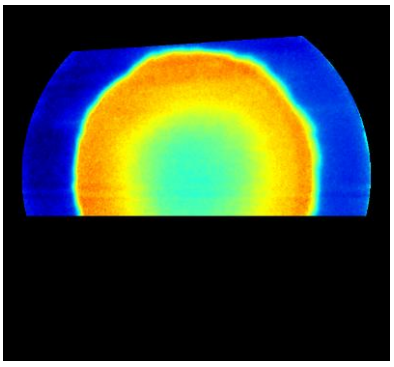	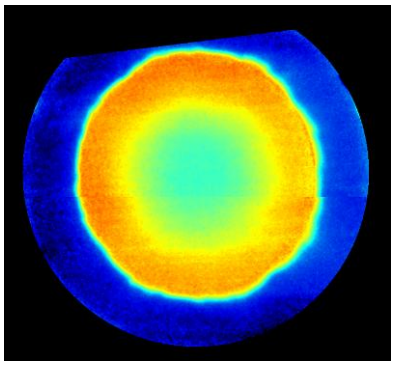	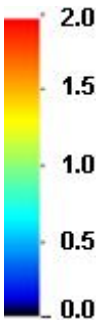
10.5%	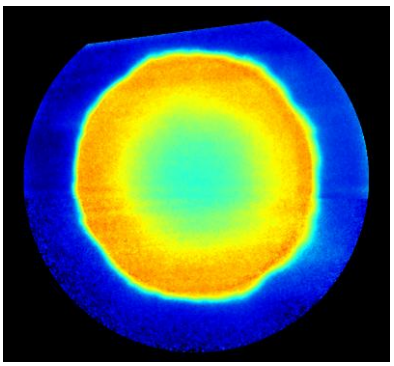	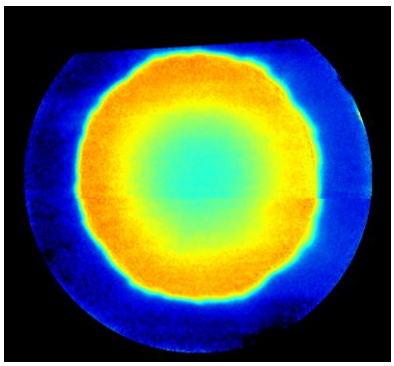	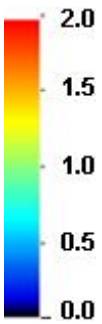

D-stage	ULN reference	ULN variant A	Map
9.0%	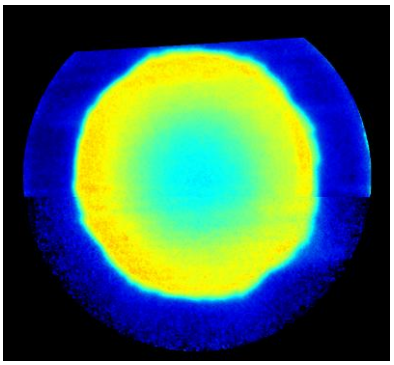	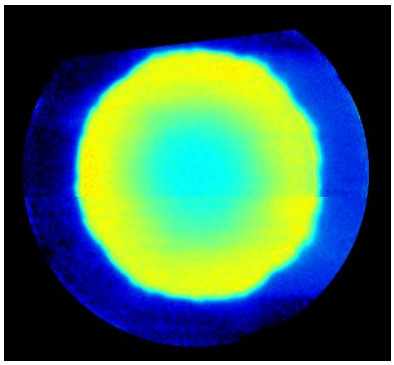	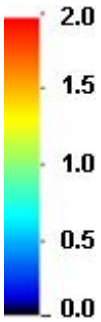
8.0%	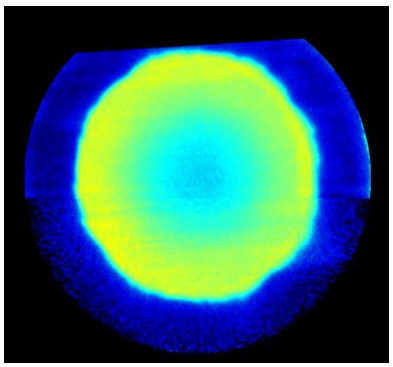	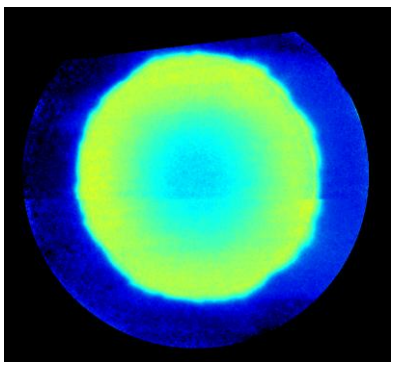	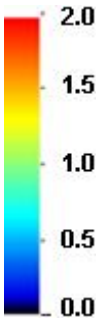

Table 3.9: LIF images of a D-stage split variation for the ULN reference burner and slightly modified ULN burner

B−A Bias Variation

As another example of LIF imaging applied to the ULN combustor a B−A bias variation is presented in Table 3.10. The B−A bias variation is basically a change of the fuel gas split between the A- and B-stage while the total fuel gas mass flow stays constant. As described earlier the A- and B- stage are the main fuel gas stages in the eight main swirlers which are surrounding the centrally installed pilot burner. In the images the arrangement of the stages is B, B, A, A, B, B A, A in clockwise direction. The pilot area is masked in black. The missing part in the upper region of the circular A-/B-stage distribution was not captured during the measurements. The mass flows are expressed as percentage B−A bias. A bias of 0% represents identical fuel mass flows for the A- and for the B-stage. Positive values indicate more B- than A-stage, and negative bias values vice versa. It can be seen that the measured fuel distribution changes with the B−A bias as expected. However, at a bias of 0% the fuel seems not equally distributed between the A- and B-stage.

B−A	ULN reference	ULN variant A	Map
10.4%	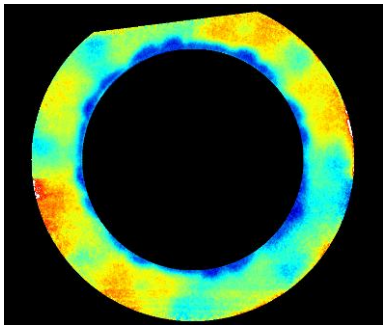	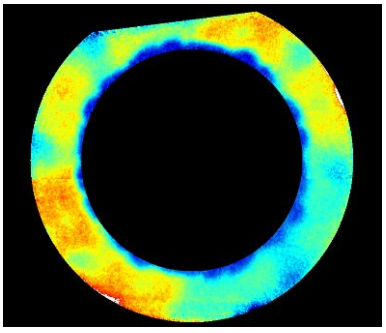	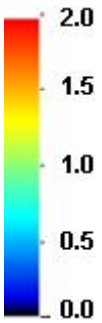
3.8%	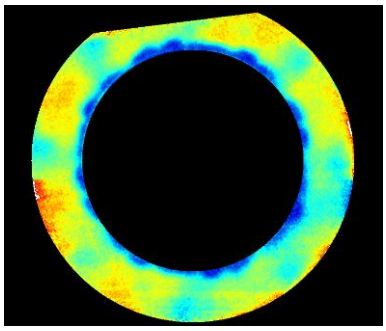	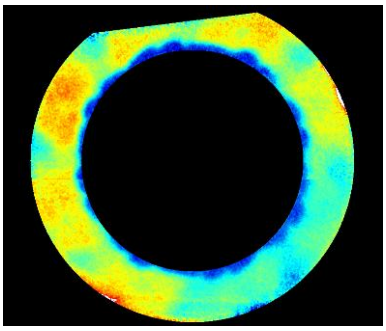	
0.0%	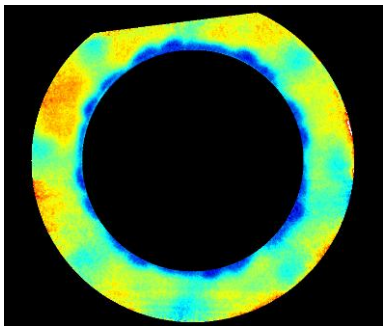	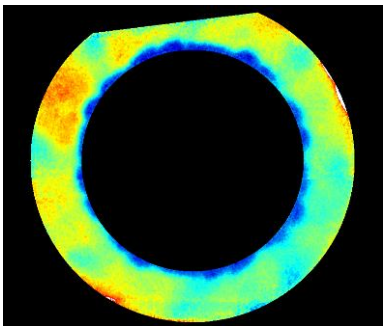	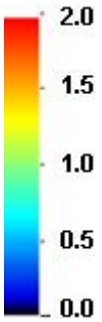
-4.2%	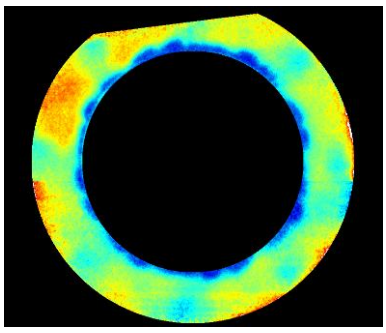	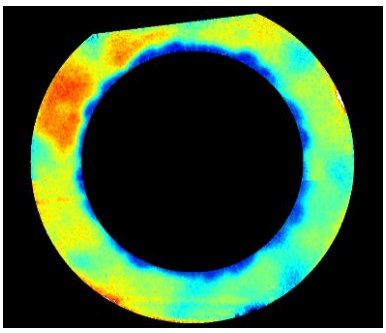	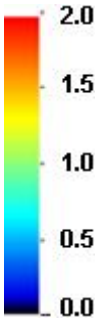
-14.1%	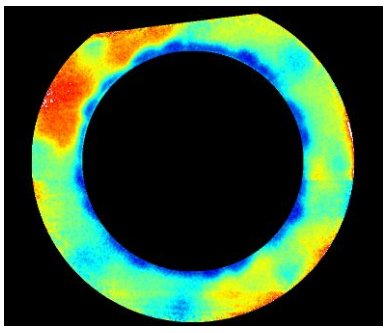	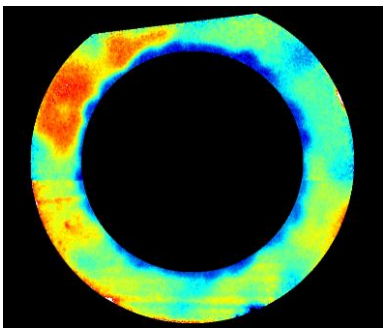	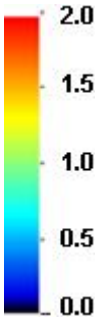

Table 3.10: LIF images from a B−A bias variation for ULN reference and ULN variant A

For a more detailed comparison of the two hardware variants the respective histograms of the B−A bias variation were investigated (see Table 3.11). As one would expect the intensity distribution shows increasing peaks above and below 1 with increasing bias. This effect was clearly stronger for the ULN variant A. However, the general trends when changing the B−A bias were quite similar for both investigated ULN variants.

B−A	ULN reference	ULN variant A
10.4%	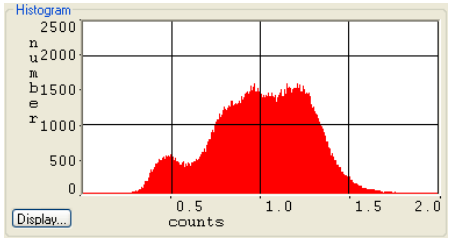	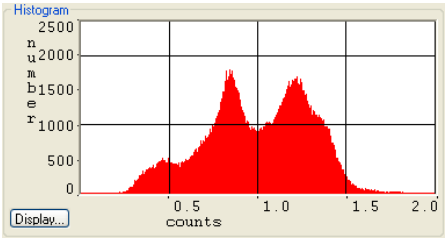
3.8%	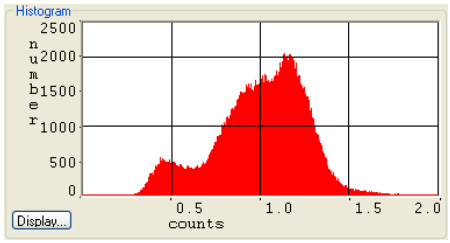	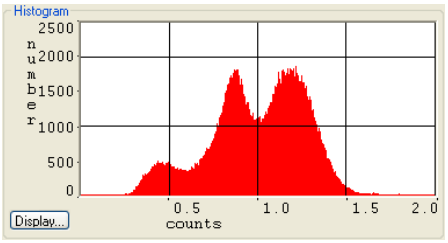
0.0%	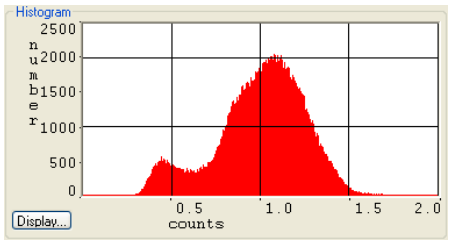	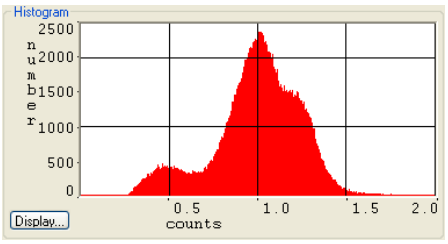
-4.2%	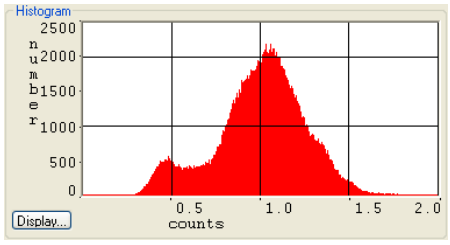	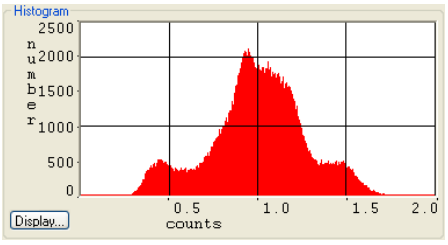
-14.1%	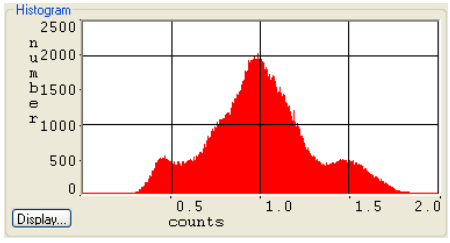	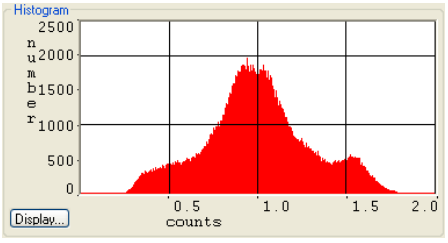

Table 3.11: Histograms derived from LIF images of a B−A bias variation for ULN reference and ULN variant A

3.5 Conclusions

The present chapter dealt with acetone LIF imaging applied to SGT5-4000F and SGT6-8000H combustors at atmospheric cold flow conditions scaled from real engine operation curves. The experimental setup and the required facilities were described in detail. Overall, the LIF experiments delivered worthwhile results with satisfying accuracy and reliability. Moreover, it could be proven that LIF imaging is sensitive enough to detect minor changes of the adjusted tracer mass flows even in the investigated large industrial-scale applications.

In parallel to the experiments, steady RANS CFD simulations were run for the SGT5-4000F case with identical geometry and boundary conditions as the experiment. The results from the experiment and the simulations were compared for different fuel splits and at different axial positions along the flow path in terms of averaged images, histograms, and radial profiles of the relative fuel concentration. It was found that the CFD tends to predict a less mixed fuel/air profile. It is believed that this is mainly caused by the limitations of the RANS approach regarding the modelling of turbulence which is directly affecting the fuel/air mixing. The potential impact of the turbulent Schmidt/Prandtl number for the simulations was investigated in this context and an improved setting for future CFD simulations with a decreased Prandtl number was found. However, general trends of the mixing profiles for different fuel splits or mixing lengths showed satisfactory agreement. Hence, steady RANS CFD simulations may be used as a reliable tool to systematically investigate and compare the effect of slight modifications on the mixing field with reasonable effort. However, it is recommended to frequently validate the most promising concepts by LIF measurements, especially in case of modifications aiming at improved mixing by increased turbulence.

Finally, for the SGT5-4000F the radial profiles measured with the suction probe method were compared with the LIF and CFD profiles. Despite the different measurement positions and the not exactly identical investigated hardware, the agreement between the two measurement techniques was quite satisfying. However, the suction probe method does not provide any temporal mixing information and has a comparatively coarse spatial resolution. Furthermore, the flow disturbing suction probe is not feasible to investigate the pilot stage with its sensitive inner recirculation zone. Finally, measurements with the suction probe method are much more time-consuming than the LIF experiments. Hence, the LIF approach is recommended as standard measurement technique for future measurement tasks.

4 Chemiluminescence Imaging Applied to a High-Pressure Combustion Test Facility

4.1 Introduction

Endoscopic chemiluminescence measurements were applied in three different high-pressure combustion test campaigns. The first campaign in July 2010 served as proof of concept for the water-cooled endoscopic probe and the selected ICCD-camera/filter combination. Based on the gained experience the second campaign was performed in March/April 2011 with an optimised combination of optical band-pass filters to record chemiluminescence images in the wavelength range of OH* (near 308 nm). Major results from this test campaign were presented at the ASME Turbo Expo 2012 in Copenhagen, Denmark [133]. In the third campaign in August/September 2012 the experimental setup was improved by using a fiberscope with a higher transmission factor and upgraded by a second intensified CCD-camera to simultaneously record images at two different spectral ranges. Furthermore, at single days of this test campaign a USB spectrometer was installed behind the fiberscope instead of the cameras to record the whole emission spectrum in the range of 250 nm to 800 nm.

In this chapter details of the endoscopic chemiluminescence measurements are described. This includes a brief introduction of the test rig and the lab facilities, the testing procedure, the optical setup, and the image post-processing steps. Afterwards, exemplary chemiluminescence images and spectra are presented and discussed. Finally, selected experimental results are compared to CFD simulations post-processed with a line-of-sight image generator.

4.2 Experimental Method

Performing single burner combustion tests at realistic gas turbine conditions requires significant infrastructure e.g. for compressed and preheated air and fuel mass flows, rig cooling, steam and exhaust gas treatment. Hence, Siemens cooperates with different partners providing sufficient facilities. The results presented in this thesis were obtained in a lab facility at the *German Aerospace Centre* (DLR) in Cologne, Germany.

4.2.1 High-Pressure Combustion Test Facility

Figure 4.1 shows an overview of the test facility at DLR Cologne. The main component is the Siemens high-pressure combustion test rig located in front of the exhaust stack and connected to the air supply line.

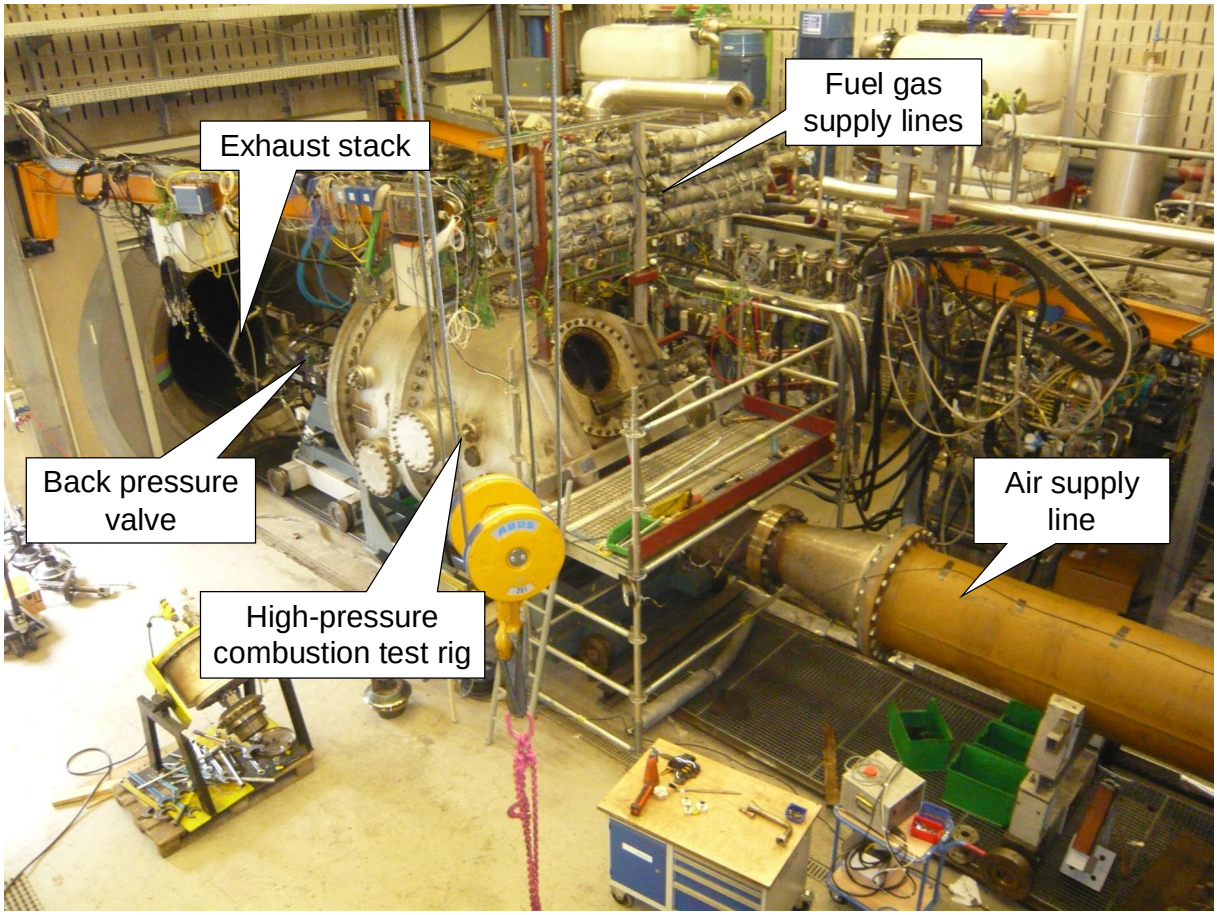

Figure 4.1: High-pressure combustion test facility at DLR Cologne

The high-pressure combustion test rig was designed for combustion tests at realistic thermodynamic gas turbine boundary conditions. With the adjustable back-pressure valve the rig can

be operated at different pressure levels up to full engine pressure. The test rig itself consists of a flow box installed in a pressure vessel. The flow box has the inner geometry of a full-scale single burner section of a real gas turbine mid-frame and includes the compressor exit diffuser and the first turbine vane row. To represent different gas turbine frames, the flow box can be changed. The chemiluminescence measurements were performed using the mid-frame flow box and combustion system of the SGT5-4000F engine with annular combustion chamber and ceramic heat shields as shown in Figure 4.2.

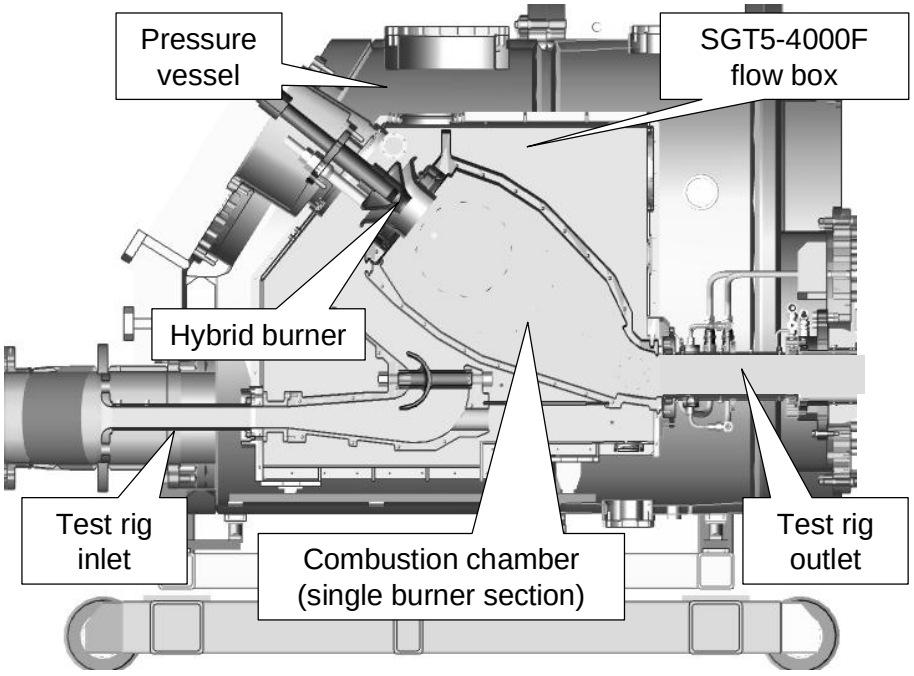

Figure 4.2: Siemens high-pressure combustion test rig with SGT5-4000F flow box

4.2.2 Testing Procedure

Similar to the previously described LIF experiments the high-pressure combustion tests were performed at flow boundary conditions derived from real engine conditions. However, the boundary conditions were typically scaled to half engine pressure. In the scale-down the air and fuel mass flow were adjusted to maintain flow velocity, residence time and relative pressure drop similar to full pressure conditions. This leads to reduced air and fuel mass flows (cf. the scaling rules introduced in chapter 3.2.1) and, hence, reduced testing costs while still providing test results sufficient for the prediction of the combustion performance at real engine pressure conditions. Figure 4.3 summarises the investigated boundary conditions, normalised by the base load reference conditions (red ball). As can be seen, the combustor load-

ing (black), the overall pilot stage split (blue), and A/B split of the main stage (green) were varied. Additionally, selected test points were repeated with fuel gas preheating to simulate the effect of different fuel gas qualities. Moreover, measurement points outside the standard operation curve were investigated to define regions of stable combustion (both not shown in Figure 4.3). This testing procedure was repeated with numerous different hardware design variants.

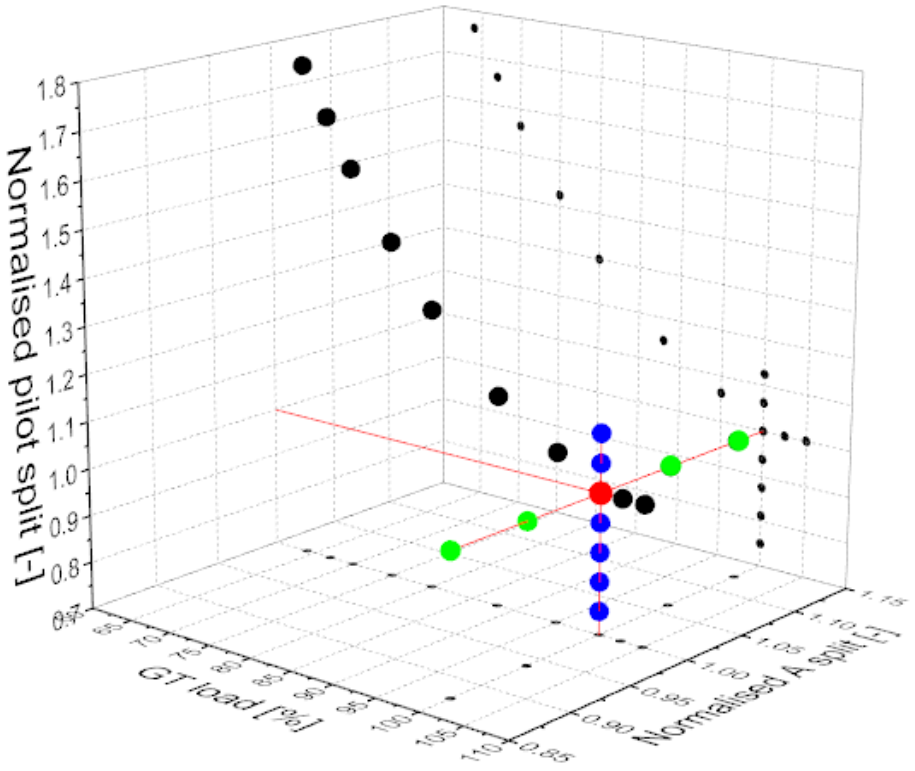

Figure 4.3: Matrix of investigated boundary conditions

Besides the chemiluminescence measurements, for all investigated boundary conditions and hardware variants the air and fuel mass flows, the fuel composition, static pressures at different locations, the dynamic pressure at several positions inside the combustion chamber, numerous media and metal temperatures, and the exhaust gas composition were recorded.

4.2.3 Optical Setup

The optical access to the test rig for the chemiluminescence measurements was realised by a water-cooled probe. The design of this probe was based on a validated video probe which was already used at numerous combustion tests before. The chemiluminescence probe featured a cooling sheath protecting a UV-transparent fiberscope from the high temperatures and pres-

sure inside the combustion chamber. Furthermore, the cooling sheath featured several channels for water and compressed air for cooling as well as a sapphire window that was flushed with nitrogen to reduce the risk of deposits on the window. The probe had a total length of approx. 1600 mm and an outer diameter of 42 mm. The fiberscope had an outer diameter of 8 mm and a beam deflection of 90°. Inside the fiberscope was a bundle with 30,000 optical fibres and an outer diameter of less than 3 mm. A sketch of the probe with details of the probe tip is given in Figure 4.4.

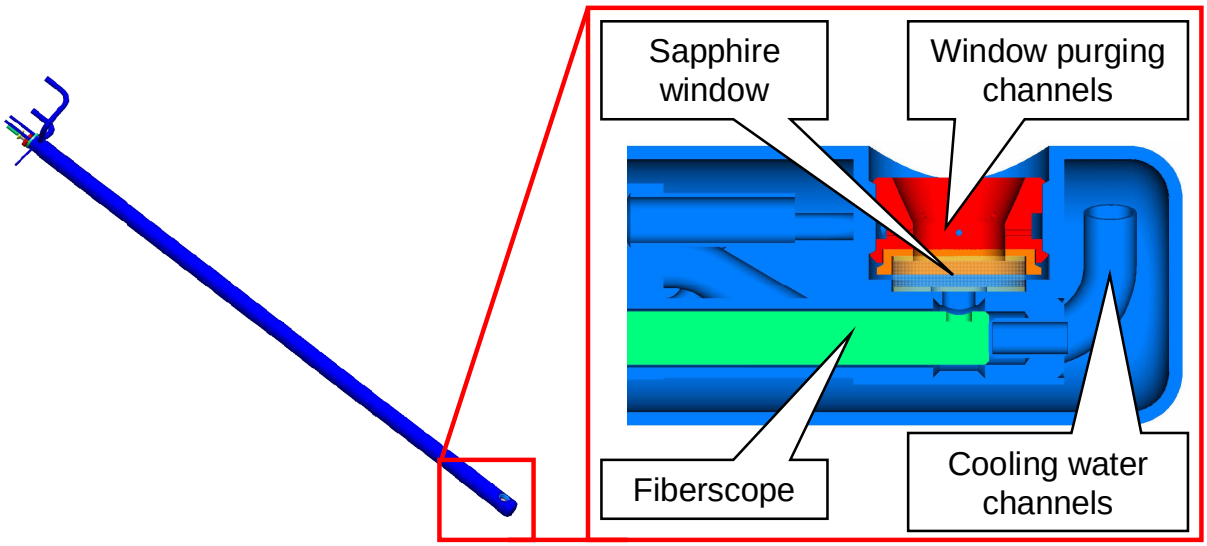

Figure 4.4: Chemiluminescence probe with probe tip details

As shown in Figure 4.5, the chemiluminescence probe was located in the test rig sidewall (indicated by the blue ball), approximately 3 *D* (*D:* burner diameter) downstream of the burner outlet. The dashed red lines indicate the probe viewing angle looking perpendicularly on the burner outlet plane.

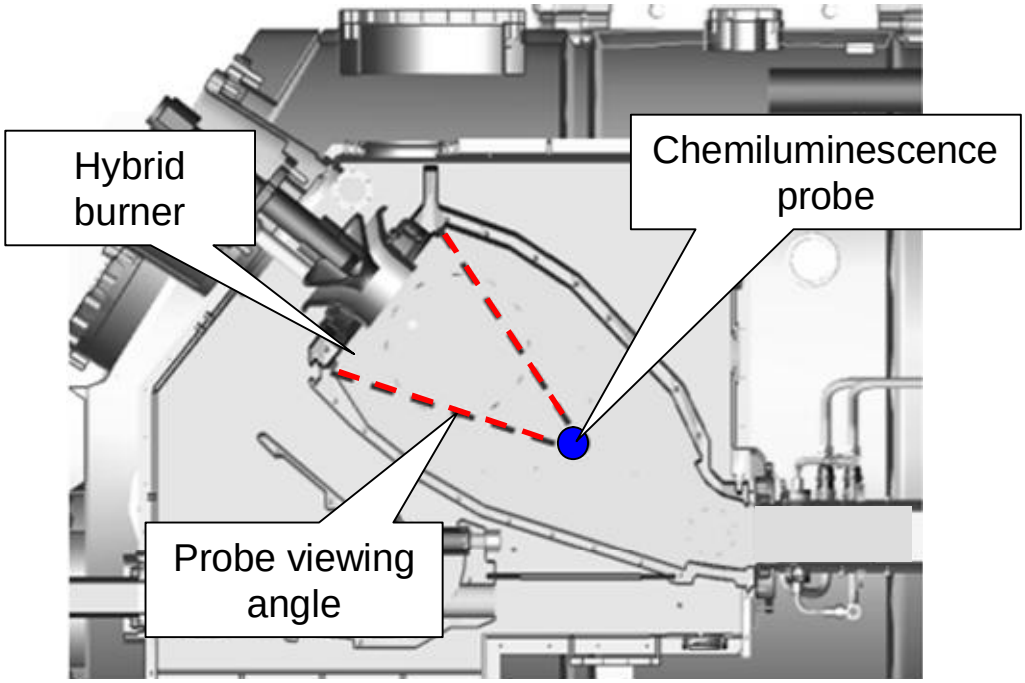

Figure 4.5: Side-view of the experimental setup indicating the probe location (blue) and the viewing angle (dashed red line)

To quantify the effect of the probe on the experiment, tests with and without the probe were performed. By varying the intrusion depth of the probe an optimized probe position could be found that had no significant effect on the combustion stability or emissions. However, with this setup, the centre of the burner was not aligned with the image centre (see Figure 4.6).

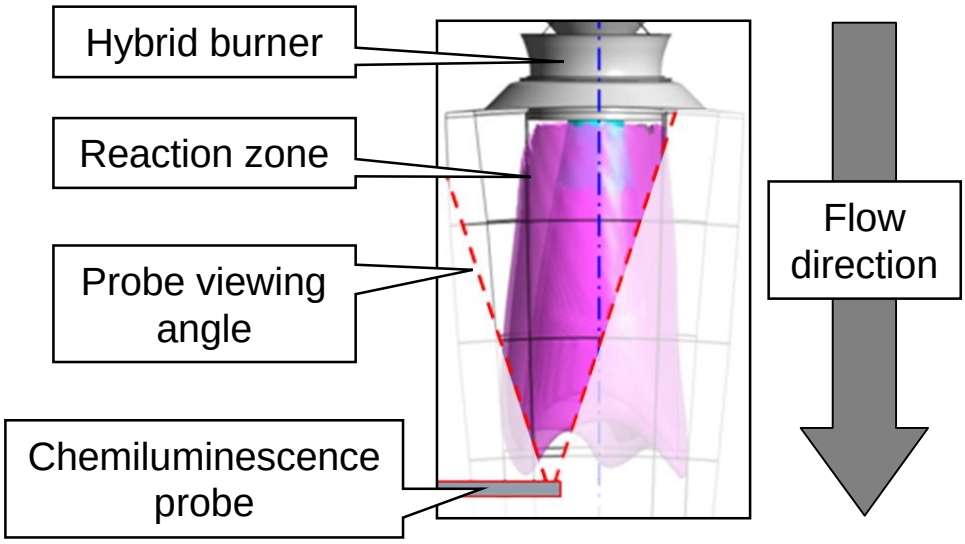

Figure 4.6: Top-view of the experimental setup indicating the probe location (grey), the viewing angle (dashed red line) and the reaction zone (purple)

The detected chemiluminescence signal was always filtered with optical band-pass filters. Depending on the species to be recorded different filter combinations were applied. For OH* a commercial band-pass (BP) filter with a central wavelength of 312 nm and a Schott UG11 were combined. CO_2* was recorded through a combination of a Schott WG345 and UG11. The CH* measurements were done with a commercial band-pass filter with a central wavelength of 430 nm. As previously mentioned, the latter two species were only measured in the third campaign where a second camera was used simultaneously. The first camera always recorded with the OH* filter combination, whereas the second camera recorded with the CH* or CO_2* filter combination. For these measurements an additional beam splitter was placed in front of the filters. The measured transmission curves of the single filter combinations including the beam splitter are shown in Figure 4.7.

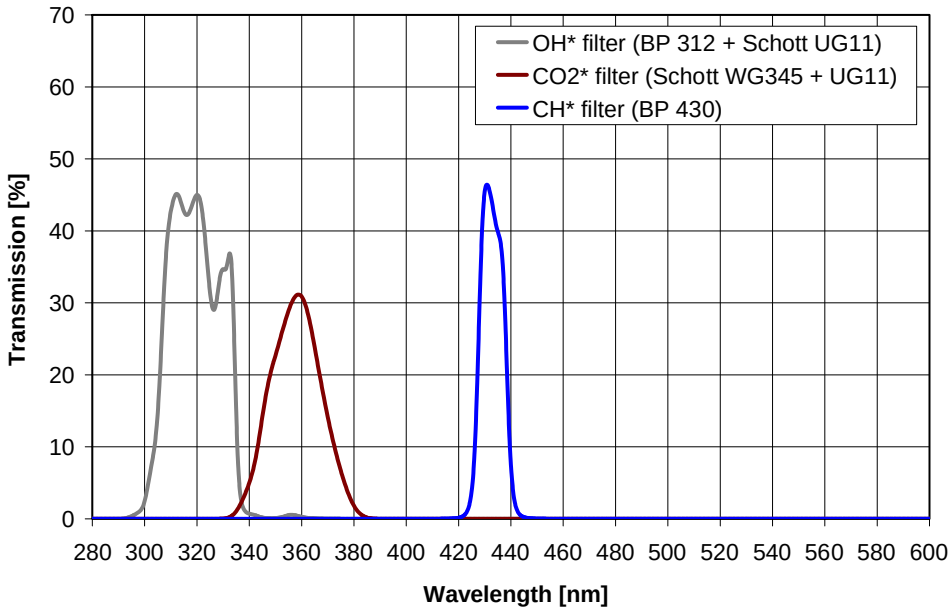

Figure 4.7: Applied filter combinations for selected chemiluminescent species

The filtered chemiluminescence signal was recorded with one or two *PCO Sensicam* CCD-cameras combined with UV-enhanced image intensifier from *LaVision GmbH*. To obtain images independently from changes of the axial flame position, lenses with high *f*-number and accordingly high depth of field were used.

4.2.4 Post-Processing Procedure

For each test point a set of 700 to 1000 single-images was recorded. The recording rate was 25 frames per second with an integration time of 500 µs and 2×2 pixel hardware binning. All

recorded images were post-processed with a dark image subtraction. To compensate effects like vignetting of the optical elements, all images were additionally corrected by a reference sensitivity map recorded with the help of a UV-light source mounted in an integrating sphere. Afterwards, the images were normalised to an identical reference intensity to allow the comparison of all images relative to each other, directly. The post-processed single-images then were used to calculate averaged and standard deviation (STD) images of the chemiluminescence signal. Videos assembled from the post-processed single images gave a good impression of the overall flame behaviour. The averaged images were used to evaluate the mean flame position for changing operation conditions and for different burner designs. The STD images additionally allowed identifying locations with increased temporal fluctuations of the flame. The post-processing steps are illustrated in Figure 4.8.

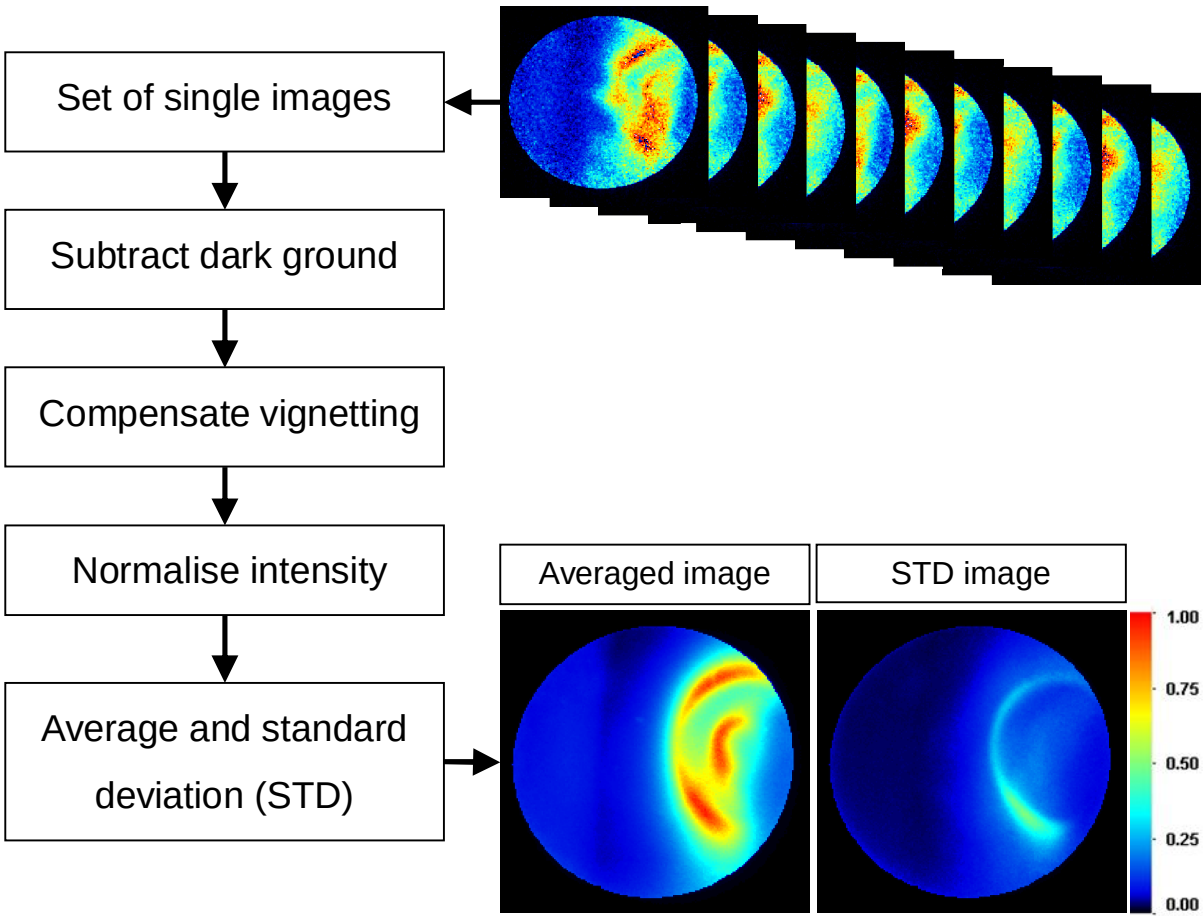

Figure 4.8: Chemiluminescence image post-processing procedure

During the chemiluminescence experiments the camera trigger signal was recorded simultaneously to time series of the acoustic pressure oscillations in the combustion chamber (see

Figure 4.9). These time series were required for the subsequent off-line phase angle reconstruction procedure as described in [25,35].

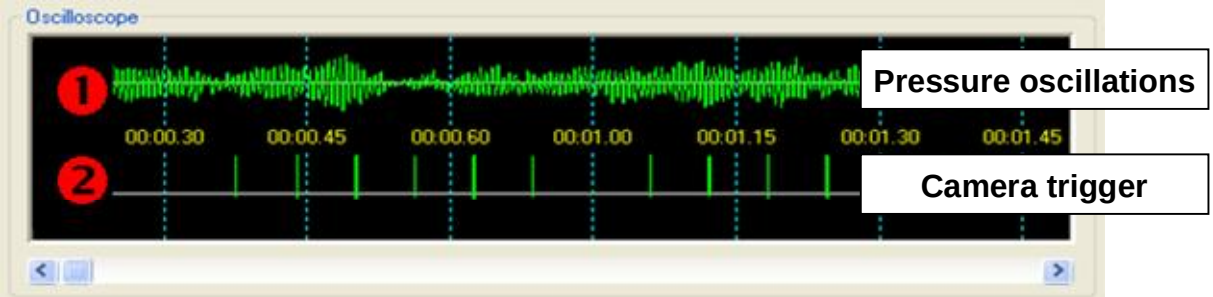

Figure 4.9: Simultaneous recording of pressure transducer signal (1) and camera trigger (2)

The applied reconstruction algorithm started with a FFT analysis of the pressure transducer time series to determine the acoustic mode frequency of interest. Next, the time series was band-pass filtered to the frequency of interest. Afterwards, the filtered signal $x(t)$ and its Hilbert transform $y(t)$

$$y(t) = \frac{1}{\pi} \int_{-\infty}^{\infty} \frac{x(t)}{(t - t)} dt \qquad \text{Equation 4.1}$$

were used to determine the "local" amplitude $A(t_i)$, phase angle $\phi(t_i)$, and frequency $\nu(t_i)$ of the pressure oscillation at the trigger time t_i when image i was recorded.

$$A(t_i) = \sqrt{x^2(t_i) + y^2(t_i)} \qquad \text{Equation 4.2}$$

$$\phi(t_i) = \arctan\left[\frac{y(t_i)}{x(t_i)}\right] \qquad \text{Equation 4.3}$$

$$\nu(t_i) = \frac{d\phi(t_i)}{dt} \qquad \text{Equation 4.4}$$

With this information linked to each stochastically recorded single image averaged images for each phase angle were calculated by statistically weighting and attaching to the 2 neighbouring phase angle groups. The resulting phase-angle uncertainty of this statistical phase averaging method is half of the width of each phase-angle group.

4.3 Results and Analysis

To ease the interpretation of the presented chemiluminescence images, at first an image recorded without flame is shown in Figure 4.10. It can be seen that the probe creates a circular image on the camera chip. The image was recorded without a burner, which is usually installed in the area of the white circle in the right half of the image. However, the outer radius of the main burner is indicated by the yellow circle and the position of the pilot burner in the centre of the burner is indicated by the green circle. As described earlier, the probe was located downstream of the burner in the test rig sidewall, viewing perpendicular towards the burner outlet. To minimise the impact of the probe on the flow, the probe was not inserted to the centre of the test rig and, hence, was not aligned with the burner centre (cf. Figure 4.6). Finally, Figure 4.10 was not post-processed with vignetting compensation to demonstrate the effect of vignetting as can be seen on the outer radius of the circular investigation window.

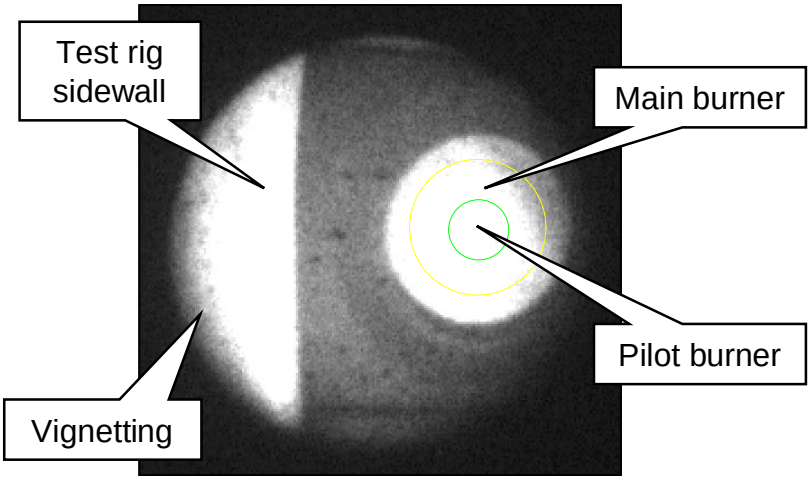

Figure 4.10: Image without flame recorded through the optical probe

Figure 4.11 shows typical single images recorded with the reference CBO burner at base load operation. The chemiluminescence signal intensity is given from dark blue (low intensity) over green and yellow to red (high intensity). The intensity scale was normalized to reference conditions taken from an averaged image recorded with the reference CBO burner at base load operation so that the maximum signal intensity is shown in red (= 1). Areas with higher intensity (e.g. at overfiring) will be shown in white. This intensity scale is identical for all images presented in this thesis. To interpret the chemiluminescence images, it is assumed that the recorded signal intensity is proportional to the line-of-sight integrated heat release rate. Based on this assumption, Figure 4.11 shows a strongly fluctuating reaction zone.

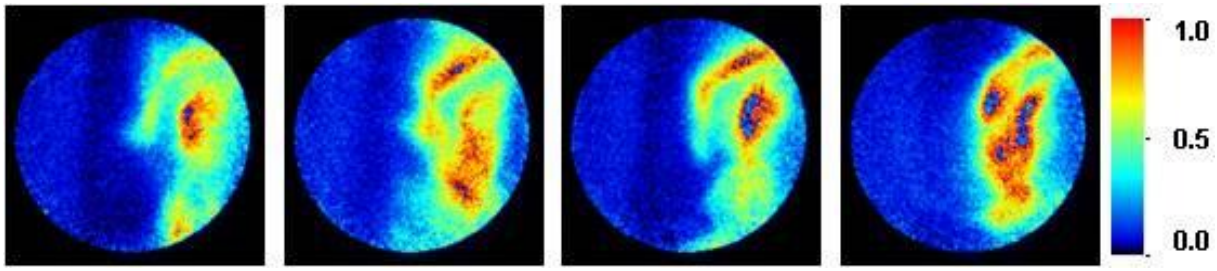

Figure 4.11: Typical single images of the reference CBO burner at base load operation

Figure 4.12 shows the respective averaged image of the reference CBO burner operated at reference base load conditions. In this image the main reaction zone is indicated with the dashed line. Furthermore, a clear distinction between the inner pilot stage and the outer main stage is possible. However, in spite of the fact that vignetting was compensated the recorded intensity on the right side of the reaction zone significantly decreases. This is believed to be caused by a combination of the line-of-sight integration of the chemiluminescence signal and the asymmetrical position of the probe.

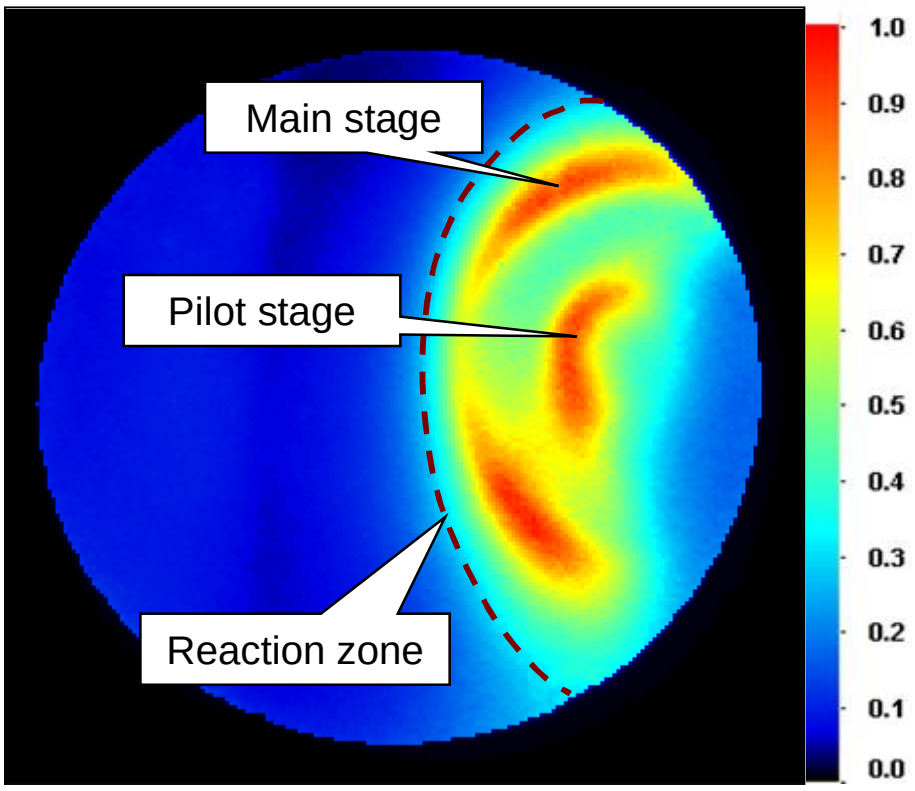

Figure 4.12: Averaged chemiluminescence image of the reference CBO burner operated at base load reference conditions

Load Variation

Figure 4.13 shows averaged chemiluminescence images recorded between 50% relative combustor load and overfiring (= 100% load plus 5% additional premix gas through the main stage). The images are linked to a qualitative sketch of the GT loading procedure showing that at part load the pilot gas fraction was relatively high to stabilize the flame and was decreased with increasing load. The chemiluminescence images clearly show that at 50% load the main chemiluminescence signal came from the pilot stage. With increasing load the pilot stage signal decreased while the main stage signal increased. During overfiring only the main stage signal increased while the pilot mass flow remained constant. This emphasizes the assumption that the separated zones with higher chemiluminescence intensity can be assigned to the main-stage and the pilot-stage respectively, as shown in Figure 4.12.

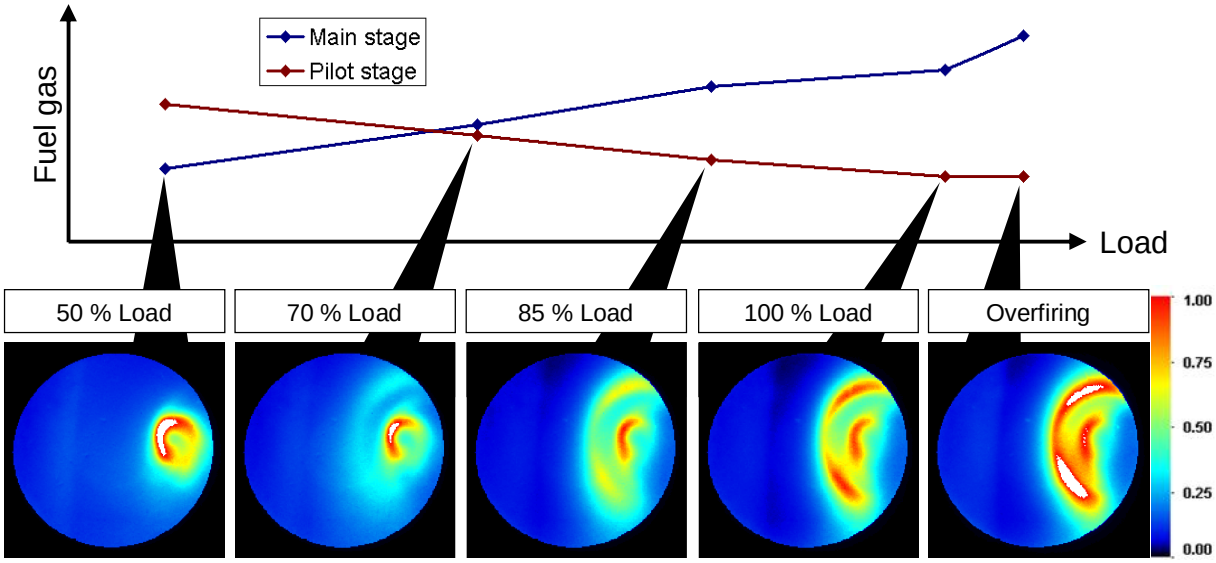

Figure 4.13: Chemiluminescence images of the reference burner recorded at different combustor load

Pilot Gas Variation

Figure 4.14 shows four images recorded at different pilot gas fractions. The pilot gas variations were performed with constant total fuel mass flow to maintain an identical adiabatic flame temperature. The pilot gas fraction has an impact on emissions and combustion stability and is an important parameter to tune the gas turbine for different operation conditions. Hence, the corresponding total NO_x emissions measured in the exhaust gas are shown for each image, too. The values were normalized to the reference conditions where the lowest

NO_x emissions were measured (middle right chemiluminescence image). With increasing pilot fraction the NO_x emissions also increased (right image). A decrease of the pilot fraction by 13% (middle left image) did not lead to a significant change of the NO_x level, whereas a further pilot fraction decrease led to a steep increase of the NO_x emissions (left image). This leads to the assumption that the increased NO_x emissions at lower pilot gas fraction were mainly produced in the main reaction zone (red and white: high chemiluminescence intensity), whereas the increased NO_x emissions at higher pilot gas fraction were mainly produced in the pilot reaction zone.

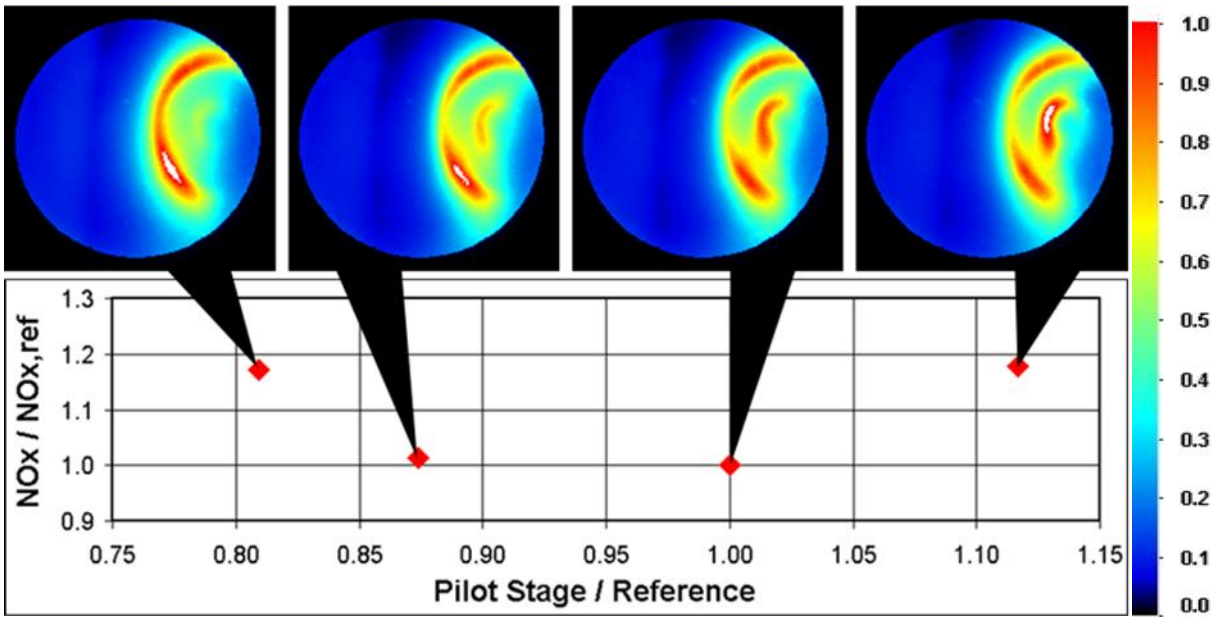

Figure 4.14: Pilot gas variation correlated with NO_x emissions

Fuel Gas Temperature Variation

The measurements with preheated and non-preheated fuel gas were performed with a fuel gas temperature difference of approximately 150 K. For preheated fuel gas the total amount of fuel was slightly decreased to balance the increased energy input and to maintain identical adiabatic flame temperatures for preheated and non-preheated fuel. However, the fuel gas preheating leads to a decreased fuel density and a correspondingly changed fuel/air momentum flux ratio. This results an increased fuel penetration depth as shown in Figure 4.15. Consequently, the fuel/air mixture and the flame position were expected to significantly differ for preheated and non-preheated fuel gas.

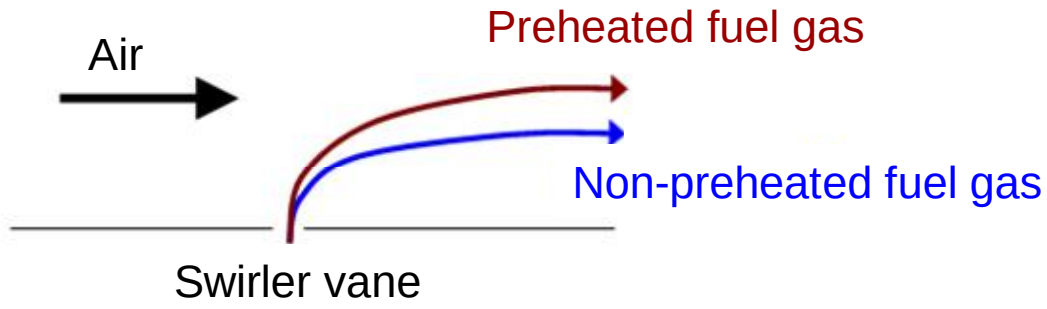

Figure 4.15: Effect of fuel preheating on fuel penetration depth

In Figure 4.16 exemplary results of chemiluminescence measurements with non-preheated fuel gas (left) and preheated fuel gas (right) are shown. It is notable that the chemiluminescence intensity without fuel gas preheating seems significantly increased, especially for the main stage, although the adiabatic flame temperature should be identical for both cases. However, this observation matches with increased NO_x emission measured for non-preheated fuel gas and emphasises the assumption that an increased chemiluminescence signal correlates with increased NO_x emissions as already observed for the investigated pilot gas variation.

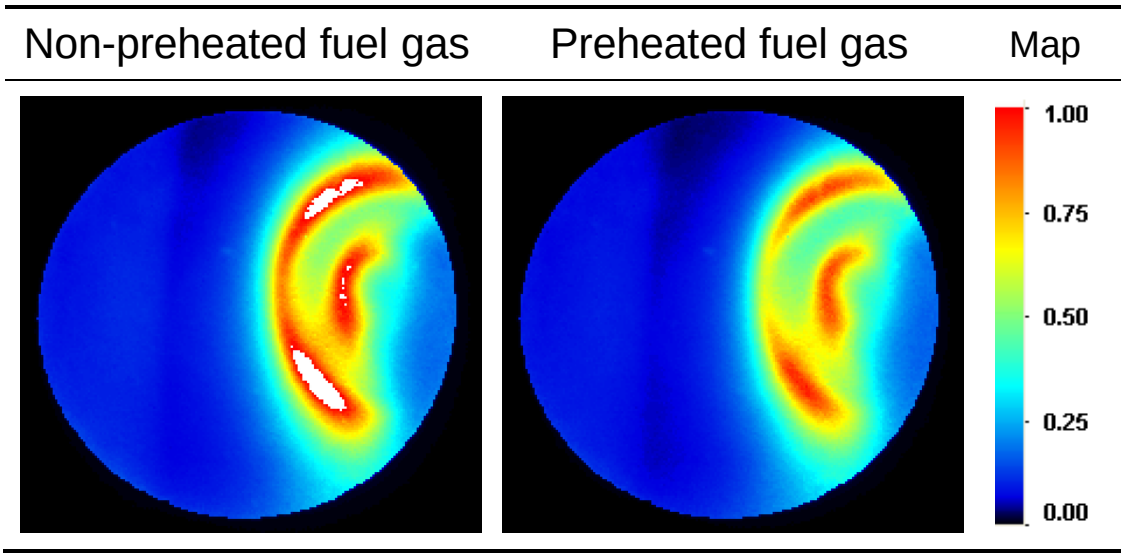

Figure 4.16: Chemiluminescence images recorded with non-preheated and preheated fuel gas

Design Variant Comparison

Figure 4.17 shows an exemplary comparison of the reference CBO burner with two burner design variants. The thermodynamic boundary conditions during recording of the presented images were identical.

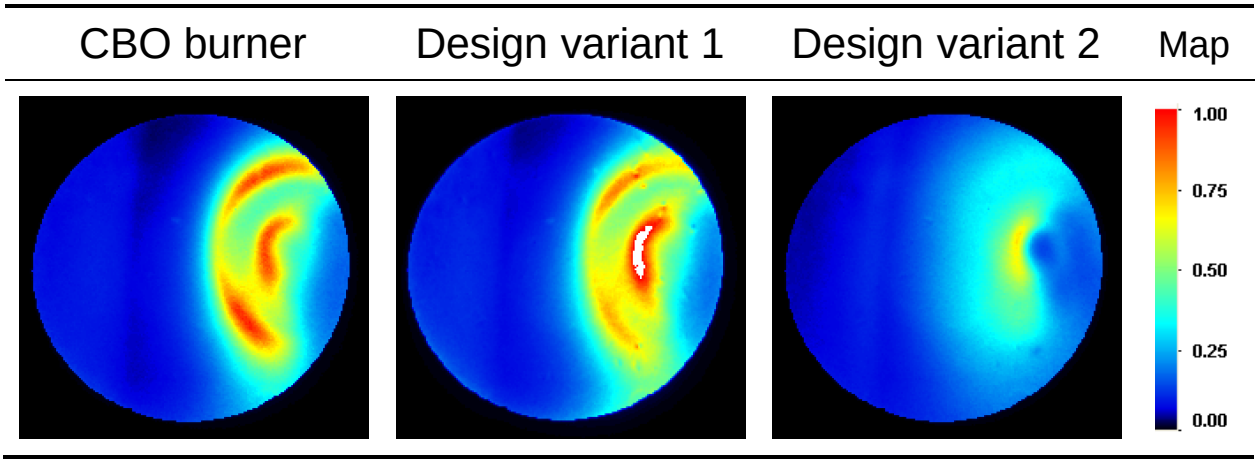

Figure 4.17: Comparison of chemiluminescence images from different burner designs

Compared to the reference CBO burner (left), design variant 1 (middle) only featured minor changes of the main burner air passage. Nonetheless, the recorded chemiluminescence image for design variant 1 showed a clear change of the flame distribution between the main stage and the pilot area. Thus, it can be assumed that the design minor changes applied at design variant 1 led to a significant change of the air split between main and pilot stage with slightly increased air mass flow through the main stage passage. Design variant 2 (right) showed a completely different reaction zone compared to the reference burner and design variant 1. A clear distinction between main and pilot reaction zone in the image was no longer possible and the overall chemiluminescence intensity is significantly lower due to the more distributed reaction zone. However, the significantly more homogeneous overall flame distribution resulted in reduced NO_x emissions, but was more prone to flame pulsations. In combination with the interpretation of the chemiluminescence image, this may suggest that a stable and separated pilot reaction zone was required to stabilize the flame.

Phase-Sorted Averaged Images

Chemiluminescence images were also recorded at boundary conditions leading to stable IFD (intermediate-frequency dynamics, here defined as 100–500 Hz). The pressure transducer for the simultaneously recorded pressure signal was located at the outer shell of the combustion chamber at an axial position close to the chemiluminescence probe. The recorded images were filtered, phase-sorted and averaged to visualise the behaviour of the reaction zone during pressure oscillations. Exemplary results of the phase-sorted averaged images are shown in Figure 4.18. The given degree value in the upper left corner of each image indicates the phase

angle of the chemiluminescence image relative to the measured pressure oscillation maximum.

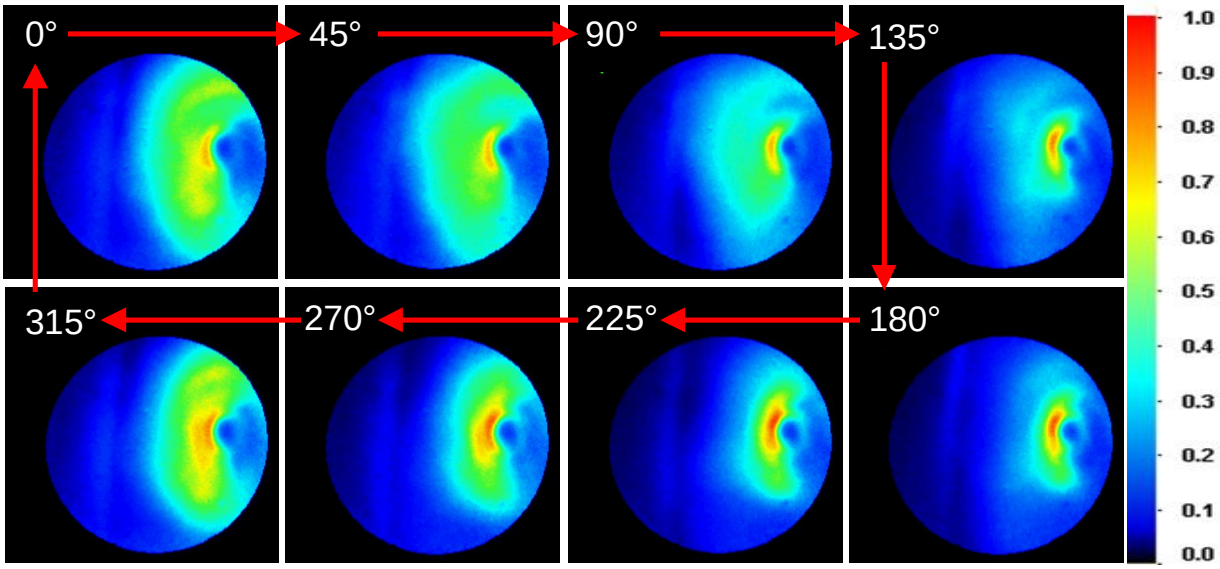

Figure 4.18: Phase-sorted averaged images showing the flame pulsation; given phase angle relative to pressure oscillation maximum

The phase-sorted images clearly show a fluctuation of the outer main stage, whereas the reaction zone of the pilot stage was nearly constant and seemed to stabilise the combustion process. This observation is consistent to the experience that an increase of the pilot fraction generally stabilises the flame, whereas a decrease of the pilot fraction may lead to flame pulsations up to a blow-off of the flame. Furthermore, it can be seen that the flame oscillation was in phase with the measured pressure oscillation inside the combustion chamber which emphasizes the assumption that pressure oscillations at the measured frequency stabilise at an axial mode.

Measured spectra

Single test days were used to record spectra inside the combustion chamber. The measurements were done without optical filters by using an Ocean Optics USB4000 spectrometer installed to the chemiluminescence probe instead of the camera(s). The aim of these measurements was to generate reference data for the correlation of the equivalence ratio and the intensity ratio of the measured species.

Figure 4.19 shows representative chemiluminescence spectra measured at base load (red) and lower part load conditions (blue). These spectra were corrected by the spectral sensitivity of the chemiluminescence probe. However, the spectral range below 300 nm should be treated with caution because the probe sensitivity in this range was strongly decreasing resulting in a correction by values close to zero (the respective correction curve for the chemiluminescence probe can be found in Appendix E). Black-body radiation for a temperature of 1600 K is shown in green.

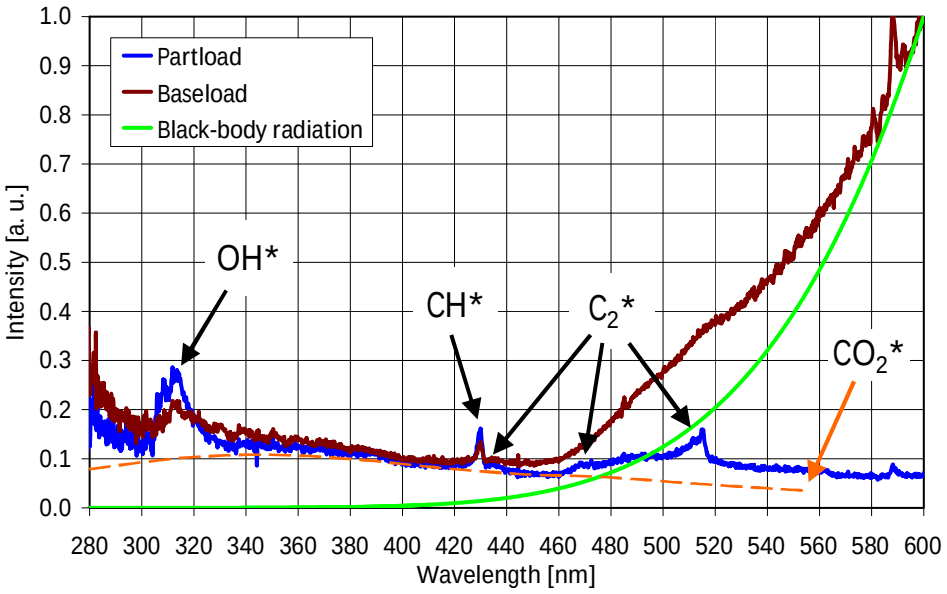

Figure 4.19: Representative spectra measured at lower part load (blue) and base load conditions (red), 1600 K black-body radiation (green), and CO_2* broad-band emission (dashed orange)

It can be seen that the base load spectrum is dominated by black-body radiation of the very hot ceramic heat shields inside the combustion chamber. Hence, a very effective blocking of the spectral range above 450 nm is mandatory to avoid overexposure when using an ICCD camera. Furthermore, the characteristic peaks of OH*, CH* and C_2* can be identified (cf. Figure 2.10). However, the OH* and CH* signals are significantly weaker for base load whereas C_2* radiation is only clearly visible in the part load spectrum. As expected, the whole spectrum is superposed by CO_2* broad-band emission (dashed orange line).

Unfortunately, the spectra recorded for parameter variations at constant load level did not show reproducible differences which would allow a satisfying interpretation. It was furthermore found that a one-to-one transfer of correlations proposed in previous studies was not

feasible, because the applied measurement method and experimental setup have a high influence on the chemiluminescence versus equivalence ratio curves. Hence, for each application a specific calibration is needed and, therefore, further investigations of the spectra are required to establish well-founded correlations for the equivalence ratio with the intensity ratios of OH*, CH* and CO_2*.

Statistical Evaluation

To increase the knowledge gained from the chemiluminescence measurements, numerous quantities were derived from the recorded images for further evaluation using statistical methods. As an example, Figure 4.20 shows the mean OH* chemiluminescence intensity from temporally averaged images correlated with the total fuel gas mass flow (left hand side) and the global lambda value (= 1/equivalence ratio, right hand side). Assuming complete combustion, the fuel gas mass flow should serve as measure for the total heat release. Figure 4.20 shows a satisfying agreement of the OH* signal intensity with the global heat release. However, also the global lambda value correlates well with the mean OH* chemiluminescence intensity (see right hand side of Figure 4.20). Hence, identical correlations are planned for the recorded CH* and CO_2* images to provide the required calibration data for further post-processing.

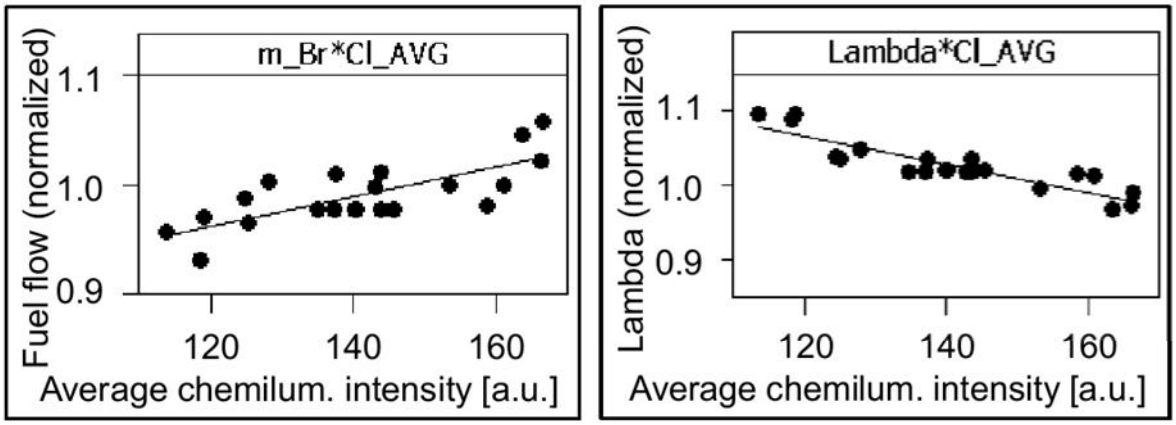

Figure 4.20: Natural gas mass flows (left) and global Lambda (right) vs. mean intensity of averaged OH* chemiluminescence images

Another example of a statistical evaluation of the chemiluminescence images is shown in Figure 4.21. On the left hand side the measured NO_x emissions are compared to the spatial standard deviation of the temporally averaged images, which serves as a measure for the spatial inhomogeneity of the chemiluminescence signal. The idea behind this evaluation is that

NO_x in gas turbines is mainly produced in regions with high temperature. Consequently, NO_x emissions may increase with increasing spatial standard deviation. On the right hand side the NO_x emissions are compared to the spatially averaged temporal standard deviation of sets of instantaneous images, which serves as a measure for the temporal fluctuation of the chemiluminescence signal.

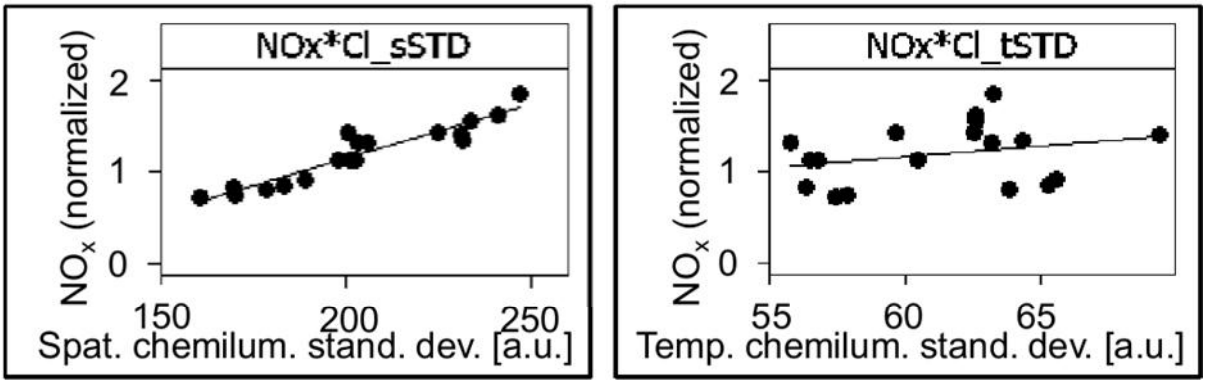

Figure 4.21: NO_x emissions vs. spatial standard deviation of temporally averaged OH* chemiluminescence image (left) and NO_x emissions vs. spatially averaged temporal standard deviation of a set of instantaneous OH* chemiluminescence images (right)

It can be seen that NO_x correlates well with the spatial standard deviation (left hand side) but not with the temporal deviation (right hand side). This may lead to the assumption that for the investigated SGT5-4000F combustor the main source for NO_x emissions are local high-temperature zones in temporally stable regions with higher heat release. However, this is contrary to previous investigation based on LES CFD simulations [16]. Potential reasons for this disagreement of experiment and simulation may be the different combustor type and thermodynamic boundary conditions, a potential lack of information about temporal chemiluminescence fluctuations due to signal integration along the line-of-sight, the missing separation of the effect of heat release and equivalence ratio fluctuations in the experiment, or simply the significantly smaller variation of temporal chemiluminescence signal fluctuations compared to the spatial chemiluminescence signal variation in the investigated experimental database. Hence, this topic will be investigated in a future LES CFD study for the identical combustion system as investigated with the chemiluminescence measurements.

4.4 Comparison to Numerical Simulations

Similar to the LIF experiments the chemiluminescence measurements were used to validate CFD simulations. Hence, RANS CFD simulations were done in parallel, again with identical geometry and flow boundary conditions as the experiment. The simulations were performed by Simon Görs within the scope of his master's thesis [30]. Figure 4.22 shows a sectional view of the computational domain for the CFD simulations. The polygonal mesh contained about 3.76 million nodes with a resolution adjusted to the burner and the boundary layer.

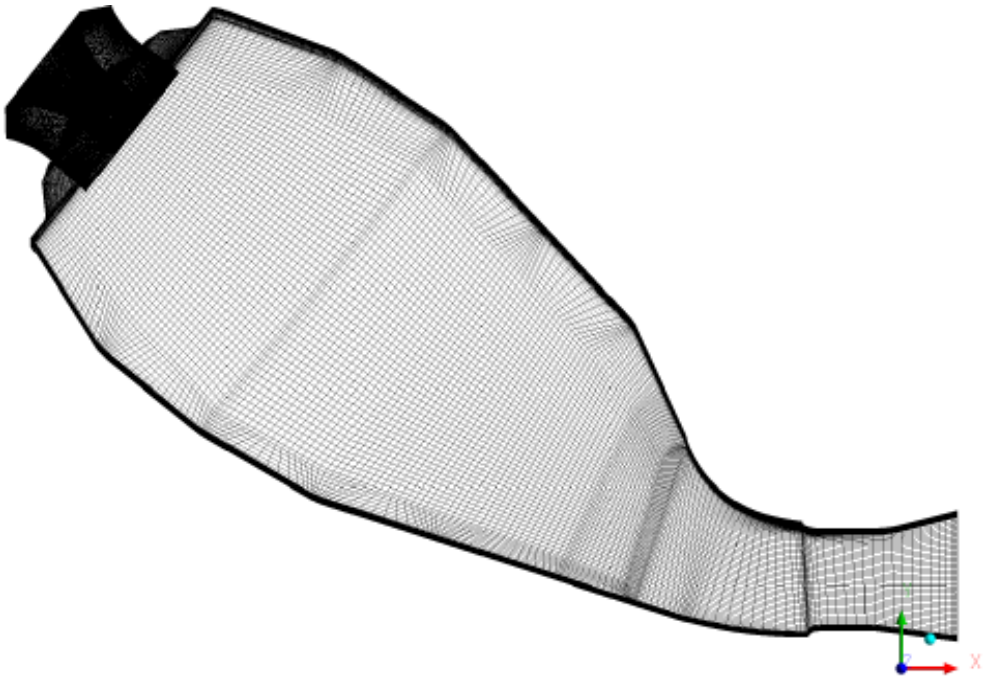

Figure 4.22: Computational domain of the SGT5-4000F high-pressure combustion test rig

As described earlier, the main difference between the real engine and the test rig is the single-burner arrangement. Hence, the test rig has sidewalls instead of the periodic conditions in the annular combustion chamber in the real engine. In CFD these sidewalls are assumed to be adiabatic. This assumption is valid due to the fact that the sidewalls consist of thick ceramic heat shields with negligible heat flux.

The thermodynamic boundary conditions were taken from the measured data from the test campaign. The several leakage airflows and the flow patterns of the pilot and main stage were tabulated for high accuracy and to uncouple the high resolution flow pattern calculation in the main and pilot stage from the combustion simulation. For turbulence modelling again the SST

model was used. The turbulent Prandtl and Schmidt numbers were set to 0.7. The turbulent burning velocity was calculated using a Zimont correlation with a pre-factor of 0.34. The simulations were done using an *Eddy Dissipation Model* (EDM). In this model the molar reaction rate is assumed to be proportional to the time required for mixing of the reactants.

The calculated temperature distributions are shown in Figure 4.23. The left hand side shows the axial temperature distribution at the centre plane and the right hand side shows the radial temperature distribution on a plane perpendicular to the burner axis, approx. 1.2 burner diameters downstream of the burner outlet.

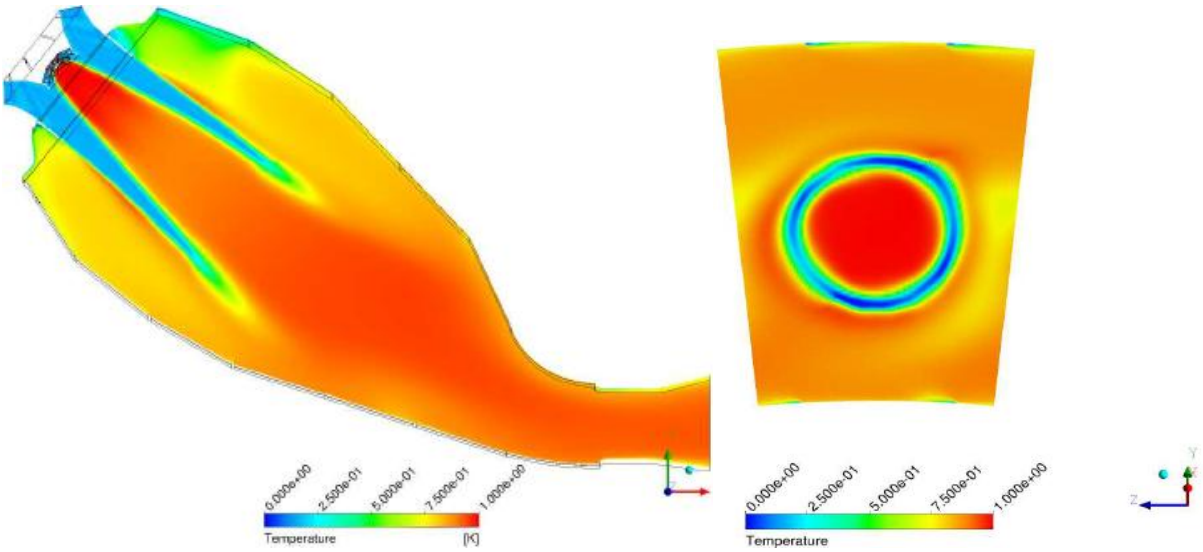

Figure 4.23: Axial and radial temperature distribution

In the temperature distribution one can see that the flame is anchored at the pilot exit and propagates into the combustion chamber with a conical shape. The highest temperatures can be found close to the pilot exit in the inner recirculation zone. The respective ISO-surface of the reaction progress value of c = 0.8 in Figure 4.24 shows a realistic flame shape with a pronounced 3-D structure.

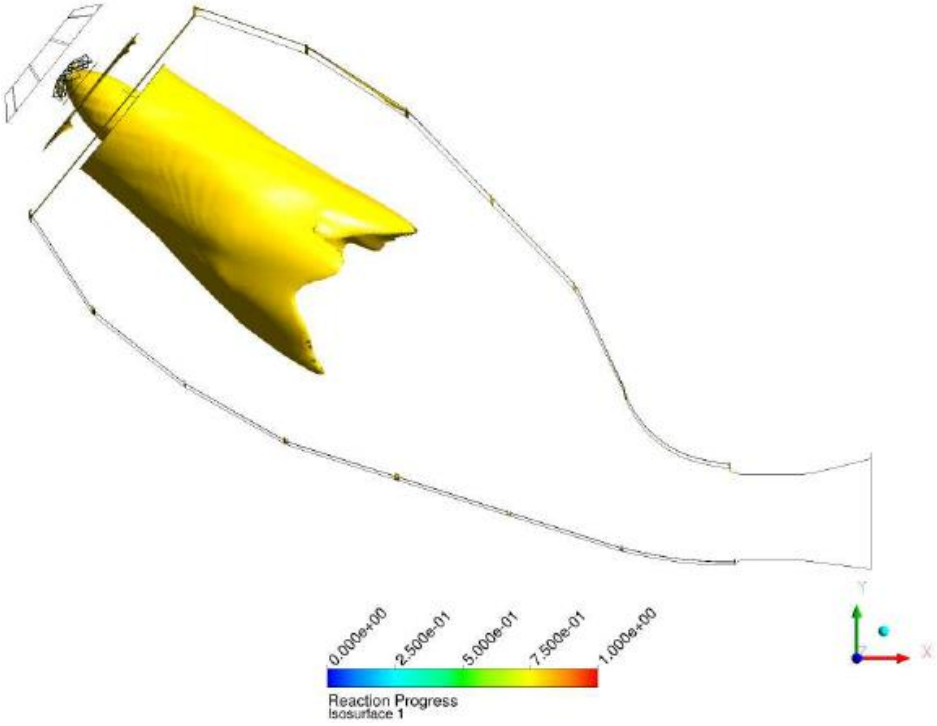

Figure 4.24: Flame ISO-surface defined as reaction progress 0.8

To allow reasonable comparison of CFD and experiment, the formation reactions, collision quenching, and the resulting radiative transit probabilities for the excited species OH* and CH* were implemented in the CFD code [30]. This data should serve as input for a ray-tracing tool generating line-of-sight images comparable to the recorded chemiluminescence images.

For the formation reactions the reaction coefficients proposed by Kojima et al. [65],[66] were taken. They were implemented in Ansys CFX in terms of tabulated chemistry depending on the local reaction progress, the mixture fraction, and the mixture fraction variance. The rate of radiative emission was defined by the Einstein coefficient for the transition probability. Collision quenching was considered for the perturber molecules N_2, O_2, H_2O, H_2, CO_2, CO, and CH_4.

However, the described tabulated approach for the modelling of the excited species was not applicable when using the EDM, because the EDM does not contain the required input parameters, i.e. the reaction progress, the mixture fraction and the mixture fraction variance. On the other hand, the *Burning Velocity Model* (BVM), which is capable to work with tabulated chemistry, did not converge for the investigated Hybrid burner case. Therefore, preparatory investigations were done using the BVM at a Bunsen burner and a ULN burner case to find a

dummy quantity for the Hybrid burner that may be used instead of the OH* and CH* concentration for the further post-processing. It was verified that the molar reaction rate is proportional to the conversion in the flame and occurred as a feasible flame front marker. Thus, the following post-processing steps were done with the molar reaction rate.

For the line-of-sight post-processing the molar reaction rate data was exported from CFD in 90 different planes. Figure 4.25 shows an example of the exported planes with every tenth plane visible. The planes were imported to *MATLAB* for calculating the required light source intensity as input for the subsequent ray-tracing tool *POV-Ray*. The light source intensity was defined as proportional to the chemiluminescence intensity calculated as product of the fluorescence yield y_i and the concentration c_i*of the excited molecules *i*. Before export to the *POV-Ray* the light intensity was grouped in ten intensity levels from 0.2 for the lowest to 1 as the brightest intensity respectively. In *POV-Ray* the optical aspects of the experimental setup like the camera perspective and the line-of-sight signal integration were simulated. The virtual camera position for the ray-tracing was taken from a CAD model of the test rig with the chemiluminescence probe. Furthermore, light fading was considered, as well. However, additional relevant effects like signal trapping by OH and beam steering were not taken into account. For further details of the preparatory investigations, the modelling approach, and the line-of-sight post-processing please refer to Görs' master thesis [30].

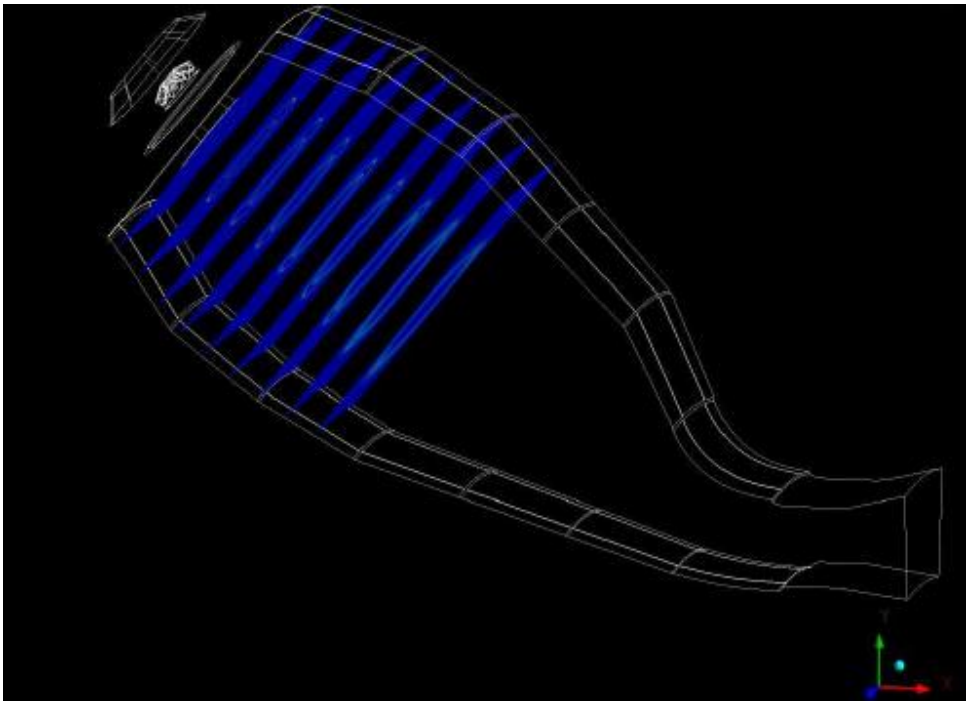

Figure 4.25: Plane-wise export of the molar reaction rate for ray tracing

Figure 4.26 shows a CFD image of the reaction zone with the line-of-sight integration post processing (left) and the respective OH* chemiluminescence image recorded in the test campaign (right).

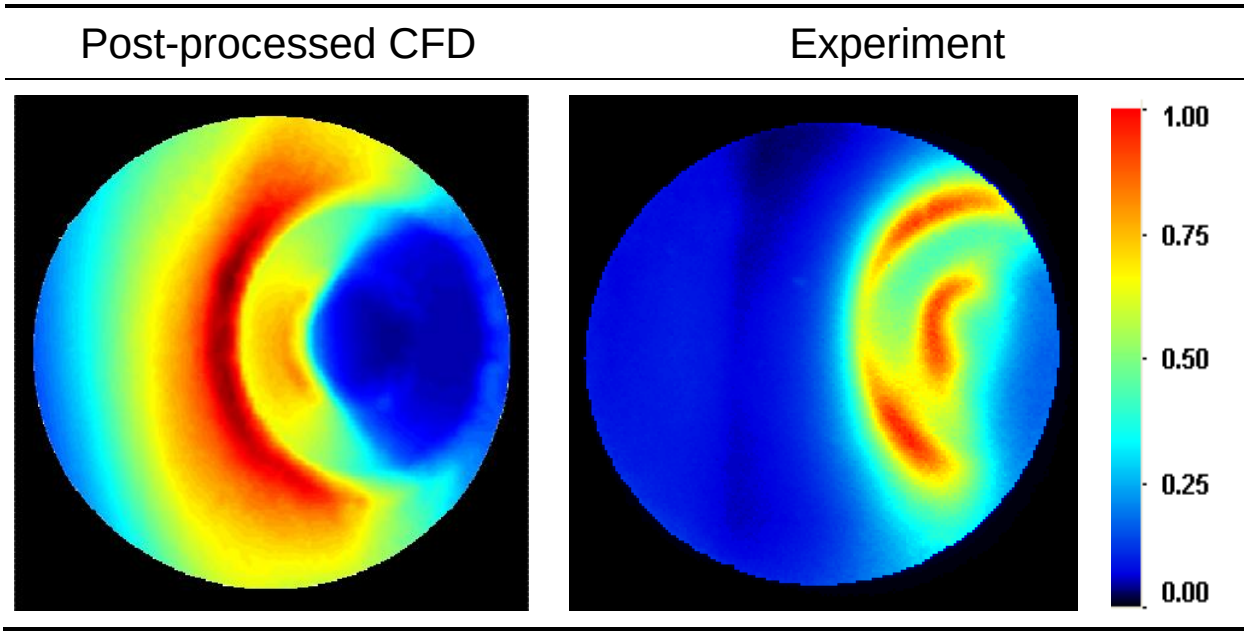

Figure 4.26: Comparison of the post-processed CFD image (left) with the respective experimental image (right)

In the post-processed CFD image the reaction zone has a higher overall intensity and is distributed over a wider area. One potential reason for this might be the missing simulation of signal trapping. Furthermore, the CFD image also shows the separated main and pilot burner reaction zones, though less pronounced as in the experiment. However, after simulation of the camera perspective the post-processed CFD image also shows the significant signal decrease on the right hand side of the image. This finally emphasises the assumption that the signal decrease was actually a consequence of the optical setup and not a real asymmetry of the reaction zone.

4.5 Conclusions

In this chapter the experimental setup and selected results from the application of chemiluminescence imaging to a full-scale SGT5-4000F high-pressure combustion test rig were presented.

It could be proven that the chemiluminescence probe could resist the challenging realistic boundary conditions during the experiments performed at a pressure of about 9 bar with the respective thermal load and the resulting mechanical stresses.

The presented test results demonstrated the feasibility of endoscopic OH*-chemiluminescence measurements to provide additional information about the complex processes during combustion at gas turbine combustion tests. The recorded images clearly showed differences of the reaction zone for varying boundary conditions like combustor load, pilot fraction, and fuel-gas temperature variation as well as for different combustor hardware designs. The evaluation of the images revealed a correlation between the main/pilot burner reaction zone and the NO_x emissions measured in the exhaust gas. Further information about the main source of NO_x emissions was derived from the chemiluminescence images with the help of simple statistical evaluations.

The phase-sorted averaged images gave insight into the type of flame fluctuation during the occurrence of pressure oscillations. It was found that this combination of image acquisition and off-line post-processing provided several advantages:

- No complicated and error-prone online camera trigger schemes and delay generators as needed for online phase-locking setups were required.
- The measuring time was used very effectively.
- The systematic phase shift errors for frequencies deviating from the centre frequency could be avoided.
- All parameters of interest like relevant frequencies, phase resolution, band-pass filtering, conditional sampling with respect to amplitude, frequency, etc. could be specified during post-processing.

For selected test days a USB spectrometer was installed instead of the cameras to measure reference data for the correlation of the OH*, CH* and CO_2* chemiluminescence signal with equivalence ratio. However, the measured spectra did not show reproducible differences allowing a well-founded interpretation. Hence, it was decided to spend additional effort on further investigations of the spectra in a future test campaign.

In parallel to the experiments, a post-processing method was developed to derive line-of-sight integrated images from CFD simulations. The results were compared to recorded chemiluminescence images. With the simulation of the camera perspective the post-processed CFD images showed the same signal decrease on the right hand side of the image as the experiment which finally indicates that this signal decrease was caused by the optical setup. Moreover, the developed post-processing method provides a valuable opportunity for a further investigation of the general feasibility of chemiluminescence imaging for CFD validation.

5 Summary and Outlook

5.1 Summary

The worldwide energy market is changing continuously. The current demands especially focus on renewable energy sources, cleaner and more efficient fossil power generation, and increased flexibility in terms operational range, load gradients, and fuels. This also poses high challenges for next generation gas turbines, particularly for the combustion systems. The processes and interactions in highly turbulent premixed combustion systems as applied in state-of-the-art low-NO_x gas turbines, however, are complex and difficult to predict with numerical tools. Hence, experiments for design validation play an important role in the combustion system development process. The objective of this thesis was to evaluate and improve the available experimental tools by utilising advanced optical measurement techniques. In particular, acetone LIF for fuel/air mixture imaging as well as endoscopic chemiluminescence measurements for flame visualisation were applied to various full-scale single burner test rigs.

Acetone-LIF imaging was performed at various original-size combustor variants of the SGT5-4000F and SGT5/6-8000H engine. For the investigation of SGT5-4000F combustors an already existing test rig was modified with UV transparent parts. For the SGT5/6-8000H combustors a completely new optical test rig with full-scale SGT6-8000H mid-frame geometry was developed and put into operation. A newly designed supply facility provided sufficiently high tracer mass flows and an easily adaptable optical setup allowed for fast and flexible adaption to the two different test rigs.

LIF experiments showed sufficient accuracy and sensitivity to capture the slight adjustments in gas concentration that typically occur during gas turbine operation as well as minor design differences of the investigated combustor variants, even in this large industrial-scale setup.

Furthermore, the results provided new information about the fuel/air mixture of the investigated combustors. This knowledge was meanwhile used to support the development of the latest SGT5-4000F combustion system evolution [62] as well as the latest SGT5/6-8000H combustion system upgrade [55].

Results from the SGT5-4000F were compared to suction-probe measurements and steady RANS CFD simulations. The overall agreement of the two measurement techniques was quite satisfying. Finally, due to better performance in terms of impact on the experiment, application flexibility, availability of temporally resolved mixture information, spatial resolution, and time required for testing, acetone-LIF imaging was recommended as standard measurement technique for future fuel/air mixing measurements. With respect to the CFD comparison it was found that the CFD tends to under-predict the mixing of fuel in air, which can most probably be assigned to the RANS modelling approach for the turbulent scales. However, general trends between LIF and CFD for different fuel splits or mixing lengths showed satisfactory agreement. Moreover, improved setting for future CFD simulations with an adjusted Prandtl number could be found. With the confirmation of predicting the correct trends and the knowledge of the CFD limitations, steady RANS CFD can now be used with increased confidence for systematic optimisations of combustor mixing fields.

Flame chemiluminescence imaging was performed in a high-pressure single-burner high-pressure combustion test rig at realistic thermodynamic boundary conditions. Optical access to the test rigs was provided by a water-cooled endoscopic probe installed in the test rig sidewall. The probe was successfully operated at boundary conditions of 9 bar and ~1800 K.

First results recorded with an intensified CCD camera with OH* band-pass filter demonstrated the general feasibility of endoscopic chemiluminescence measurements as robust experimental tool providing more insight into the complex processes during combustion tests. Simultaneous recording of chemiluminescence images and pressure oscillations allowed for phase sorting of the images during post processing. This method provided additional valuable information about flame/acoustic interaction.

Moreover, chemiluminescence images were recorded with two cameras simultaneously. The first camera was filtered for OH* whereas the second camera was filtered for CH* or CO_2* detection. To gather the required calibration data for the calculation of equivalence ratio and/or heat release from the simultaneously recorded images, additionally chemiluminescence

spectra were recorded by using a fibre-coupled spectrometer. In the measured spectra the characteristic peaks of OH*, CH*, and C_2* could be identified overlapping with a significant portion of CO_2* broad-band emission. Furthermore, a significant contribution of black-body radiation from hot combustor parts could be seen. The spectra, however, only showed little sensitivity against changes of the operation conditions so that additional effort is needed to derive the required information for post processing of the simultaneously recorded OH*/CH* and OH*/CO_2* images. The spectra did not show an expected dip in the range of 308 nm which indicates a well-chosen probe position with comparably low OH* signal trapping by OH.

Statistical evaluations of quantities derived from OH* chemiluminescence images showed correlations of the average OH* signal intensity with the total fuel gas mass flow (as measure for the total heat release) and the equivalence ratio. On the one hand, this confirms the conclusions from other studies that OH* alone is not a reliable marker for heat release, which was already addressed by the simultaneous recording of two species. On the other hand, the correlations generally indicate that with the current experimental arrangement well-founded conclusions can be made from chemiluminescence measurements despite the line-of-sight integration of the measured signals. Statistical evaluations of the OH* signal and NO_x emission showed a high correlation with the spatial standard deviation, but not with temporal signal fluctuations. This information may help to identify burner-specific leading NO_x formation mechanisms as a direct feedback for the validation process. Because the temporal distribution is expected to be at least similarly important, numerical studies were initiated for further investigation of this topic.

A post-processing method for CFD was developed to simulate line-of-sight signal integration. A comparison of in this way post-processed steady RANS CFD images with experimental results helped to interpret certain observations in the recorded chemiluminescence images. To increase the agreement between simulation and experiment, it is planned to add signal trapping to the post-processing method and to apply it to more-detailed LES CFD simulations.

5.2 Outlook

The conclusions from the acetone LIF measurements led to initiating an extensive CFD study where the experimental data will be used as reference. Within this study further optimisation of parameter settings for steady RANS simulations will be done as well as a comparison with results from unsteady DES and LES. The purpose of the study is to develop validated numerical tools optimised for specific design tasks with respect to the level of details provided vs. the required meshing effort and computational cost. Furthermore, the study will lead to a better understanding of potential limitations of each simulation approach avoiding misinterpretations and wrong conclusions. To also increase the usability of mixing measurements as direct pre-selector for costly high-pressure tests, it is recommended to generate more experimental data with comparable boundary conditions and combustor hardware to investigate the coupling of measured mixture profiles and combustion performance.

On the 27th of September 2013 Siemens laid the foundation stone for a new burner test centre *Clean Energy Center* in Ludwigsfelde near Berlin [116]. Encouraged by the good experience made within the presented study, it is planned to intensify the application of optical measurement techniques at high-pressure combustion tests at this test centre. Hence, publicly co-funded cooperation projects with several research institutes were started in 2013. One of the biggest tasks in this context is the enhancement of the chemiluminescence measurements towards multi-species high-speed imaging, a more flexible optical probe design, and the development of a tomographic reconstruction algorithm to derive volumetric flame information from simultaneous measurements at multiple positions. Moreover, the developed optical accesses will be used for the application of CO TDLAS measurements, FRS and surface temperature measurements using thermographic phosphors.

In summary, the realisation of the initiated measures will make an important contribution to aid the development of the next generation of cleaner and more flexible gas turbine combustion systems at reduced development time and costs.

Bibliography

[1] ATKINS, P. W.
Physikalische Chemie
VCH Verlagsgesellschaft, 1990.

[2] BALLING, L.
GT-Kraftwerke
Stationäre Gasturbinen, 2nd Edition, edt. by C. Lechner and J. Seume, pp. 49-100, Springer-Verlag, Berlin Heidelberg, 2010.

[3] BECKER, B.; SCHULENBERG, T.; TERMUEHLEN, H.
The 3A-Series Gas Turbines with HBR™ Combustors
Proceedings of the ASME Turbo Expo, 95-GT-458, 1995.

[4] BESSLER, W. G.; SCHULZ, C.
Quantitative Multi-line NO-LIF Temperature Imaging
Applied Physics B-Lasers Opt., 78, pp. 519-533, 2004.

[5] BIAGIOLI, F.; GÜTHE, F.
Effect of Pressure and Fuel-Air Unmixedness on NO_x Emissions from Industrial Gas Turbine Burners
Combustion and Flame, 151, pp. 274-288, 2007.

[6] BLAHA, C.
Laser-2-Focus Measurements in a Transonic Compressor Blisk-Rotor and Comparison with 3D Numerical Simulations
International Symposium Air Breathing Engines, Chattanooga, USA, 1997.

[7] BOGUSZKO, M.; ELLIOTT, G. S.
On the Use of Filtered Rayleigh Scattering for Measurements in Compressible Flows and Thermal Fields
Experiments in Fluids, Vol. 38, pp. 33-49, 2005.

[8] BOZKURT, M.; FIKRI, M.; SCHULZ, C.
Investigation of the Kinetics of OH and CH* Chemiluminescence in Hydrocarbon Oxidation Behind Reflected Shock Waves*
Applied Physics B-Lasers Opt., 107, pp. 515-527, 2012.

[9] BRAUN, J.
Thermodynamische Grundlagen
Stationäre Gasturbinen, 2nd Edition, edt. by C. Lechner and J. Seume, pp. 29-35, Springer-Verlag, Berlin Heidelberg, 2010.

[10] BROCKHINKE, A.; KRÜGER, J.; HEUSING, M.; LETZGUS, M.
Measurement and Simulation of Rotationally-Resolved Chemiluminescence Spectra in Flames
Applied Physics B-Lasers Opt., 107, pp. 539-549, 2012.

[11] BROCKHINKE, A.; SCHULZ, C.
Editorial: Selected Papers About Chemiluminescence of Flames
Applied Physics B-Lasers Opt., 107, pp. 513-514, 2012.

[12] CABOT, W.; MOIN, P.
Approximate Wall-Boundary Conditions in the Large-Eddy Simulation of High Reynolds Number Flows
Flow, Turbulence and Combustion, Vol. 63, pp. 269-291, 2000.

[13] CLARK, T.
Studies of OH, CO, CH and C2 Radiation from Laminar and Turbulent Propane-Air and Ethylene-Air Flames - NACA Technical Note 4266
National Advisory Committee for Aeronautics, Lewis Flight Propulsion Laboratory Cleveland, Ohio, 1958.

[14] CLARK, T.; BITTKER, D.
A Study of the Radiation from Laminar and Turbulent Open Propane-Air Flames as a Function of Flame Area, Equivalence Ratio, and Fuel Flow Rate
National Advisory Committee for Aeronautics, Lewis Flight Propulsion Laboratory Cleveland, Ohio, 1954.

[15] COX JR., G. B.
Multiple Jet Correlations for Gas Turbine Engine Combustor Design
Journal of Engineering and Power April 1976, ASME Paper No. 75-GT-45, pp. 265-273, 1976.

[16] DEDERICHS, S.; ZARZALIS, N.; HABISREUTHER, P.; BECK, C.; PRADE, B.; KREBS, W.
Assessment of a Gas Turbine NO_x Reduction Potential Based on a Spatiatemporal Unmixedness Parameter
Journal of Engineering for Gas Turbines and Power, Vol. 135, 111504, 2013.

[17] DEMTRÖDER, W.
Laserspektroskopie, Grundlagen und Techniken, 5. Auflage
Springer-Verlag, Berlin Heidelberg New York, 2007.

[18] DREIER, T.; RAKESTRAW, D.J.
Degenerate Four-Wave Mixing Diagnostics on OH and NH Radicals in Flames
Applied Physics B (Photophysics and Laser Chemistry), 50, 479-485, 1990.

[19] DÜSING, K. M.; CIANI, A.; EROGLU, A.
Effect of Mixing Quality on NOx Emissions in Reheat Combustion of GT24 & GT26 Engines
Proceedings of the ASME Turbo Expo, GT2011-45676, 2011.

[20] EBERT, V.; FERNHOLZ, T.; GIESEMANN, C.; PITZ, H.; TEICHERT, H.; WOLFRUM, J.; JARITZ, H.
Simultaneous Diode-Laser-Based In Situ Detection of Multiple Species and Temperature in a Gas-Fired Power Plant
Proceedings of the Combustion Institute, 28, pp. 423-430, 2000.

[21] ECKBRETH, A. C.
CARS Investigations in Flames
Proceedings of the Combustion Institute, 17, pp. 975-983, 1979.

[22] ECKBRETH, A. C.
Laser Diagnostics for Combustion Temperature and Species, 2nd Edition
Combustion Science and Technology Book Series, Vol. 3, 1996.

[23] EPSTEIN, A. H.
Quantitative Density Visualization in a Transonic Compressor Rotor
Journal of Engineering for Power, 99, pp. 460-475, 1977.

[24] ERTEM, C. K.; JANICKA, J.; DREIZLER, A.
Ray Tracing of Chemiluminescence in an Unconfined Non-Premixed Turbulent Jet Flame Using Large-Eddy Simulation
Applied Physics B-Lasers Opt., 107, pp. 603-610, 2012.

[25] FISCHER, A.; BAKE, F.; HEINZE, J.; DIERS, O.; WILLERT, C.; ROEHLE, I.
Off-line Phase-averaged Particle Image Velocimetry and OH Chemiluminescence Measurements Using Acoustic Time Series
Measurement Science and Technology, Vol. 20, 075403 (10 pp.), 2009.

[26] FISCHER, M.; STOCKHAUSEN, G.; HEINZE, J.; SEIFERT, M.; MÜLLER, M.; SCHODL, R.
Development of Doppler Global Velocimetry (DGV) Measurement Devices and Combined Application of DGV and OH Chemiluminescence Imaging to Gas Turbine Combustor*
12th International Symposium on Application of Laser Techniques to Fluid Mechanics, Lisbon, 2004.

[27] GAYDON, A. G.
The Spectroscopy of Flames
Wiley, New York, 1957.

[28] GAYDON, A. G.; WOLFHARD, H. G.
Spectroscopic Studies of Low-Pressure Flames
3rd Symposium on Combustion, Flame and Explosion Phenomena, pp. 504-518, 1949.

[29] GAYDON, A. G.; WOLFHARD, H. G.
Flames: Their Structure, Radiation, and Temperature
Chapman and Hall, London, 1978.

[30] GÖRS, S.
Development and Implementation of a Flame Chemiluminescence Post Processing for Industrial CFD Modeling
Master thesis, Siemens AG, Energy Sector, Mülheim a. d. Ruhr, 2012.

[31] GÖRS, S.; WITZEL, B.; HEINZE, J.; STOCKHAUSEN, G.; VAN KAMPEN, J.; SCHULZ, C.; WILLERT, C.; FLEING, C.
Endoscopic Chemiluminescence Measurements as a Robust Experimental Tool in High-Pressure Gas Turbine Combustion Tests
Proceedings of the ASME Turbo Expo, GT2014-26977, 2014.

[32] GRAF, N.
Einsatz der Laserinduzierten Fluoreszenz organischer Moleküle zur Visualisierung von Gemischbildungs- und Verbrennungsprozessen
Dissertation, Naturwissenschaftlich-Mathematische Gesamtfakultät, Ruprecht-Karls-Universität Heidelberg, 2003.

[33] GREENWOOD, S.A.
Combustion Driven Pressure Oscillations (Humming)… a Low Emission Design Problem
ASME IGTI Global Gas Turbine News, Vol. 41, No. 1, pp. 12-15, 2001.

[34] GROSSMANN, F.; MONKHOUSE, P. B.; RIDDER, M.; SICK, V.; WOLFRUM, J.
Temperature and Pressure Dependences of the Laser-induced Fluorescence of Gas-phase Acetone and 3-Pentanone
Applied Physics B-Lasers Opt., 62, pp. 249-253, 1996.

[35] GÜTHE, F.; SCHUERMANS, B.
Phase-locking in Post-processing for Pulsating Flames
Measurement Science and Technology, Vol. 18, pp. 3036-3042, 2007.

[36] GÜTHE, F.; GUYOT, D.; SINGLA, G.; NOIRAY, N.; SCHUERMANS, B.
Chemiluminescence as Diagnostic Tool in the Development of Gas Turbines
Applied Physics B-Lasers Opt., 107, pp. 619-636, 2012.

[37] GUYOT, D.; GÜTHE, F.; SCHUERMANS, B.; LACARELLE, A.; PASCHEREIT, O.
CH/OH* Chemiluminescence Response of an Atmospheric Premixed Flame Under Varying Operation Conditions*
Proceedings of the ASME Turbo Expo, GT2010-23135, 2010.

[38] HAAS, Y.
Photochemical Alpha-cleavage of Ketones: Revisiting Acetone
Photochem. Photobiol. Sci., 3: pp. 6-16, 2004.

[39] HABER, L. C.
An Investigation into the Origin, Measurement and Application of Chemiluminescent Light Emissions from Premixed Flames
Master thesis, Virginia Polytechnic Institute and State University, 2000.

[40] HABER, L. C.; VANDSBURGER, U.; SAUNDERS, W.; KHANNA, V.
An Experimental Examination of the Relationship between Chemiluminescenct Light Emissions and Heat-Release Rate under Non-Adiabatic Conditions
Proceedings of the ASME Turbo Expo, 2000-GT-0121, 2000.

[41] HAKEN, H.; WOLF, H. C.
Molekülphysik und Quantenchemie
Springer-Verlag, Berlin Heidelberg, 3. Auflage, 1998.

[42] HARDALUPAS, Y.; ORAIN, M.
Local Measurements of the Time-Dependent Heat Release Rate and Equivalence Ratio Using Chemiluminescent Emission From a Flame
Combustion and Flame, 139, pp. 188-207, 2004.

[43] HANSON, R. K.; SEITZMANN, J. M.; PAUL, P. H.
Planar Laser-Fluorescence Imaging of Combustion Gases
Applied Physics B (Photophysics and Laser Chemistry), 50, pp .441-454, 1990.

[44] HARDALUPAS, Y.; PANOUTSOS, C. S.; TAYLOR, A. M. K. P.
Spatial Resolution of a Chemiluminescence Sensor for Local Heat Release Rate and Equivalence Ratio Measurements in a Model Gas Turbine Combustor
Experiments in Fluids, 49, pp. 883-909, 2010.

[45] HERZBERG, G.
Molecular Spectra and Molecular Structure, I. Spectra of Diatomic Molecules
Robert E. Krieger Publishing Comp., Malabar, Florida, 1989.

[46] HIGGINS, B.; MCQUAY, M.; LACAS, F.; CANDEL, S.
An Experimental Study of Pressure and Strain Rate on CH Chemiluminescence on Premixed Fuel lean Methane/Air Flames
Fuel, 80, pp. 1583-1591, 2001.

[47] HIGGINS, B.; MCQUAY, M.; LACAS, F.; ROLON, J.; DARABIHA, N.; CANDEL, S.
Systematic Measurements of OH Chemiluminescence for Fuel-lean High-pressure, Premixed, Laminar Flames
Fuel, 80, pp. 67-74, 2001.

[48] HIRONOBU, U; MASAHIRO, I.; DAISAKU, S.
Optical Measurement Technology for Turbomachinery. Laser 2-Focus Velocimeter for Flow Measurements in Turbomachinery
Turbomachinery, 28; pp. 257-264, 2000.

[49] HOEREN, A.
Laserspektroskopische Untersuchung turbulenter Mischprozesse in einer Gasturbinen-Vormischstrecke
Dissertation, Faculty of Mechanical Engineering, Ruhr-Universität Bochum, 2000.

[50] HOFFMAN, A.
Strukturanalyse turbulenter Flammen mit Hilfe abbildender laserspektroskopischer Verfahren
Dissertation, Faculty of Natural Sciences and Mathematics, Ruprecht-Karls-Universität Heidelberg, 2006.

[51] HOLDEMAN, J. D.
Mixing of Multiple Jets With a Confined Subsonic Crossflow
27th Joint Propulsion Conference, Sacramento, California, June 24-27, 1991.

[52] HUBSCHMID, W.; BOMBACH, R.; INAUEN, A.; GÜTHE, F.; SCHENKER, S.; TYLLI, N.; KREUTNER, W.
Thermoacoustically Driven Flame Motion and Heat Release Variation in a Swirl-stabilized Gas Turbine Burner Investigated by LIF and Chemiluminescence
Experiments in Fluids, 45, pp. 167-182, 2008.

[53] HUTH, M.; GRUSCHKA, U.; JANUS, B.; MEISL, J.; WASIF, S.
ULN System for the New SGT5-8000H Gas Turbine: Design and High Pressure Rig Test Results
Proceedings of the ASME Turbo Expo, GT2008-51208, 2008.

[54] HUTH, M.; GRUSCHKA, U.; JANUS, B.; MEISL, J.
Design of the Combustion System for the SGT5-8000H and First Experiences in the Irsching Power Plant
VGP Power Tech 10/2009.

[55] JANUS, B.; BIGALK, J.; HELMERS, L.; WITZEL, B.; GHERMAY, Y.; HUTH, M.; JOHNSON, C. E.; LANDRY, K.; SUNSHINE, R.
Successfully Validated Combustion System Upgrade for the SGT5/6-8000H Gas Turbines: Technical Features and Test Results
Proceedings of the ASME Turbo Expo, GT2014-27015, 2014.

[56] KAPULLA, R.; BRAVO NAJERO, S.
Operation Conditions of a Phase Doppler Anemometer: Droplet Size Measurements with Laser Beam Power, Photomultiplier Voltage, Signal Gain and Signal-to-Noise Ratio as Parameters
Measurement Science and Technology, Vol. 17, pp. 221-227, 2006.

[57] KATHROTIA, T.; FIKRI, M.; BOZKURT, M.; HARTMANN, M.; RIEDEL, U.; SCHULZ, C.
Study of the H + O + M Reaction Forming OH: Kinetics of OH* Chemiluminescence in Hydrogen Combustion Systems*
Combustion and Flame, 157, pp. 1261–1273, 2010.

[58] KATHROTIA, T.; RIEDEL, U.; SEIPEL, A.; MOSHAMMER, K.; BROCKHINKE, A.
Experimental and Numerical Study of Chemiluminescent Species in Low-Pressure Flames
Applied Physics B-Lasers Opt., 107, pp. 571-584, 2012.

[59] KATHROTIA, T.; RIEDEL, U.; WARNATZ, J.
A Numerical Study on the Relation of OH, CH*, and C2* Chemiluminescence and Heat Release in Premixed Methane Flames*
Proceedings of the European Combustion Meeting, 2009.

[60] KOCH, J. D.; HANSON, R. K.; KOBAN, W.; SCHULZ, C.
Rayleigh-calibrated Fluorescence Quantum Yield Measurements of Acetone and 3-Pentanone
Applied Optics, 43, pp. 5901-5910, 2004.

[61] KOCK, B. F.
Zeitaufgelöste Laserinduzierte Inkandeszenz (TR-LII): Partikelgrößenmessung in einem Dieselmotor und einem Gasphasenreaktor
Dissertation, Institut für Verbrennung und Gasdynamik, Universität Duisburg, Germany, 2005.

[62] KOCK, B. F.; PRADE, B.; WITZEL, B.; STREB, H.; KOENIG, M. H.
Combustion System Update SGT5-4000F – Design, Testing & Validation
Proceedings of the ASME Turbo Expo, GT2013-95569, 2013.

[63] KOHSE-HÖINGHAUS, K.; BARLOW, R. S.; ALDÉN, M.; WOLFRUM, J.
Combustion at the Focus: Laser Diagnostics and Control
Proceedings of the Combustion Institute, 30, pp. 89-123, 2005.

[64] KOHSE-HÖINGHAUS, K.; JEFFRIES, J. B.
Applied Combustion Diagnostics
Taylor & Francis, London, 2002.

[65] KOJIMA, J.; IKEDA, Y.; NAKAJIMA, T.
Spatially Resolved Measurement of OH, CH*, and C_2* Chemiluminescence in the Reaction Zone of Laminar Methane/Air Premixed Flames*
Proceedings of the Combustion Institute, 28, pp. 1757–1764, 2000.

[66] KOJIMA, J.; IKEDA, Y.; NAKAJIMA, T.
Basic Aspects of OH(A), CH(A) and C2(d) Chemiluminescence in the Reaction Zone of Laminar Methane-Air Premixed Flames
Combustion and Flame, 140, pp. 34-45, 2005.

[67] KOPP, M.; BROWER, M.; MATHIEU, O.; PETERSEN, E.; GÜTHE, F.
CO2 Chemiluminescence Study at Low and Elevated Pressures*
Applied Physics B-Lasers Opt., 107, pp. 529-538, 2012.

[68] KRÄMER, H.; DINKELACKER, F.; LEIPERTZ, A.; POESCHL, G.; HUTH, M.; LENZE, M.
Optimization of the Mixing Quality of a Real Size Gas Turbine Burner with Instantaneous Planar Laser-Induced Fluorescence Imaging
Proceedings of the ASME Turbo Expo, 99-GT-135, 1999.

[69] KREBS, W.; FLOHR, P.; PRADE, B.; HOFFMANN, S.
Thermoacoustic Stability Chart for High-Intensity Gas Turbine Combustion Systems
Combustion Science and Technology, 174, pp. 99-128, 2002.

[70] KREBS, W.; HELLAT, J.; EROGLU, A.
Technische Verbrennungssysteme
Stationäre Gasturbinen, 2nd Edition, edt. by C. Lechner and J. Seume, pp. 453-491, Springer-Verlag, Berlin Heidelberg, 2010.

[71] KREBS, W.; KREDIET, H.; PORTILLO, E.; HERMETH, S.; POINSOT, T.; SCHIMEK, S.; PASCHEREIT, C. O.
Comparison of Nonlinear to Linear Thermoacoustic Stability Analysis of a Gas Turbine Combustion System
Proceedings of the ASME Turbo Expo, GT2012-69477, 2012.

[72] LAUER, M.
Determination of the Heat Release Distribution in Turbulent Flames by Chemiluminescence Imaging
Dissertation, Faculty of Mechanical Engineering, TU München, 2011.

[73] LAUER, M.; SATTELMAYER, T.
On the Adequacy of Chemiluminescence as a Measure for Heat Release in Turbulent Flames with Mixture Gradients
Journal of Engineering for Gas Turbines and Power, Vol. 132, 061502 (8 pp.), 2012.

[74] LIEUWEN, T.; NEUMEIER, Y.; ZINN, B. T.
The Role of Unmixedness and Chemical Kinetics in Driving Combustion Instabilities in Lean Premixed Combustors
Combustion Science and Technology, 135, pp. 193-211, 1998.

[75] LIEUWEN, T.; RICHARDS, G.; WEBER, J.
Approaching Zero
Mechanical Engineering, Vol. 132, pp. 22-27, 2010.

[76] LIEUWEN, T.; ZINN, B. T.
The Role of Equivalence Ratio Oscillations in Driving Combustion Instabilities in Low NO_x Gas Turbines
Proceedings of the Combustion Institute, 27, pp. 1809-1816, 1998.

[77] LÖFFLER, M. G.
Entwicklung einer planaren Lasermesstechnik zur simultanen Temperatur- und Konzentrationsmessung bei Gemsichbildungsprozessen im Ottomotor
Dissertation, Technical Faculty of the University of Erlangen-Nürnberg, 2011.

[78] LOZANO, A.; YIP, B.; HANSON, R. K.
Acetone: A Tracer for Concentration Measurements in Gaseous Flows by Planar Laser-induced Fluorescence
Exp. Fluids, 13, pp. 369-376, 1992.

[79] LÜCKERATH, R.; LAMMEL, O.; STÖHR, M.; BOXX, I.; STOPPER, U.; MEIER, W.; JANUS, B.; WEGNER, B.
Experimental Investigations of Flame Stabilization of a Gas Turbine Combustor
Proceedings of ASME Turbo Expo, GT2011-45790, 2011.

[80] LUONG, M.; KOBAN, W.; SCHULZ, C.
Novel Strategies for Imaging Temperature Distribution Using Toluene LIF
Journal of Physics: Conference Series, 45, pp. 133-139, 2006.

[81] LUQUE, J.; CROSLEY, D. R.
LIFBASE: Database and Spectral Simulation Program (Version 1.5)
SRI International Report MP 99-009, 1999.

[82] MILONNI, P. W.; EBERLY J. H.
Lasers
John Wiley & Sons, New York, USA, 1988.

[83] MURUGANANDAM, T. M.; KIM, B.; OLSEN, R.; PATEL, M.; ROMIG, B.; SEITZMAN, J. M.
Chemiluminescence Based Sensors for Turbine Engines
39th AIAA/ASME/SAE/ASEE Joint Propulsion Conference, Huntsville, AL, July 20–23, Paper No. AIAA-2003-4490, 2003.

[84] NAJM, H. N.; PAUL, P. H.; MUELLER, C. J.; WYCKOFF, P. S.
On the Adequacy of Certain Experimental Observables as Measurements of Flame Burning Rate
Combustion and Flame, 113, pp. 312-332, 1998.

[85] NIEDERBERGER, A. S. P.; FRITSCHE, D.; BOULOUCHOS, K.; GUZZELLA, L.
Thermoacoustic Instability Suppression by Gain-Delay and H_∞ Controllers Designed for Secondary Fuel Injection
IEEE Transactions on Control Systems Technology, Vol. 17, pp. 1028-1042, 2009.

[86] NORI, V.; SEITZMAN, J.
Chemiluminescence Measurements and Modeling in Syngas, Methane and Jet-A Fueled Combustors
45th Aerospace Sciences Meeting, Reno, NV, Jan. 8–11, Paper No. AIAA-2007-0466, 2007.

[87] NORI, V.; SEITZMAN, J.
Evaluation of Chemiluminescence as a Combustion Diagnostic under Varying Operating Conditions
46th Aerospace Sciences Meeting and Exhibition, Reno, NV, Jan. 7–10, Paper No. AIAA-2008-0953, 2008.

[88] NORI, V.; SEITZMAN, J.
CH Chemiluminescence Modeling for Combustion Diagnostics*
Proceedings of the Combustion Institute, 32, pp. 895–903, 2009.

[89] OBERTACKE, R.; LEIPERTZ, A.; WINTRICH, H.; WINTRICH, F.
A New Sensor System for Industrial Combustion Monitoring and Control Using UV Emission Spectroscopy and Tomography
Combustion Science and Technology, 121, pp. 133-151, 1996.

[90] PANOUTSOS, C. S.; HARDALUPAS, Y.; TAYLOR, A. M. K. P.
Numerical Evaluation of Equivalence Ratio Measurement Using OH and CH* Chemiluminescence in Premixed and Non-Premixed Methane-Air Flames*
Combustion and Flame, 156, pp. 273-291, 2009.

[91] PFADLER, S.
Entwicklung und Einsatz der konditionierten Particle Image Velocimetry zur Charakterisierung und Modellvalidierung turbulenter Vormischflammen
Dissertation, Lehrstuhl für Technische Thermodynamik, Universität Erlangen-Nürnberg, Germany, 2008.

[92] PFADLER, S.; BEYRAU, F.; LÖFFLER, M.; LEIPERTZ, A.
Application of a Beam Homogenizer to Planar Laser Diagnostics
Opt. Express, 14, pp. 10171-10180, 2006.

[93] PIOMELLI, U.; BALARAS, E.
Wall-Layer Models for Large-Eddy Simulations
Annular Review Fluid Mechanics, 34, pp. 349-374, 2002.

[94] PIV
Special Issue: Particle Image Velocimetry
Measurement Science and Technology, 8, pp. 1379-1583, 1997.

[95] POINSOT, T.; VEYNANTE, D.
Theoretical and Numerical Combustion, 2nd Edition
R. T. Edwards, Inc., Philadelphia, PA, USA, 2005.

[96] POPE, S. B.
Turbulent Flows
Cambridge University Press, 2000.

[97] PRABASENA, B.; RÖDER, M.; KATHROTIA, T.; RIEDEL, U.; DREIER, T.; SCHULZ, C.
Strain Rate and Fuel Composition Dependence of Chemiluminescent Species Profiles in Non-Premixed Counterflow Flames: Comparison With Model Results
Applied Physics B-Lasers Opt., 107, pp. 561-569, 2012.

[98] PUTNAM, A. A.
Combustion-Driven Oscillation in Industry
American Elsevier, New York, 1971.

[99] RAFFEL, M.; WILLERT, C.; KOMPENHANS, J.
Particle Image Velocimetry
Springer Verlag, Berlin Heidelberg, 1998.

[100] RAKESTRAW, D.J.; FARROW, R.L.; DREIER; T.
Two-dimensional Imaging of OH in Flames by Degenerate Four-Wave Mixing
Optics Letters, 15, pp. 709-711, 1990.

[101] RAYLEIGH, J. W. S.
The Explanation of Certain Acoustical Phenomena
Nature, XVIII, pp. 319-321, 1878.

[102] RÖDER, M.; DREIER, T.; SCHULZ, S.
Simultaneous Measurement of Localized Heat Release with OH/CH2O-LIF Imaging and Spatially Integrated OH Chemiluminescence in Turbulent Swirl Flames*
Applied Physics B-Lasers Opt., 107, pp. 611-617, 2012.

[103] RÖDER, M.; DREIER, T.; SCHULZ, S.
Simultaneous Measurement of Localized Heat Release with OH/CH2O-LIF Imaging and Spatially Integrated OH Chemiluminescence in Turbulent Swirl Flames*
Proceedings of the Combustion Institute, 34, pp. 3549-3556, 2013.

[104] ROEHLE, I.; SCHODL, R.; VOIGT, P.; WILLERT, C.
Recent Developments and Applications of Quantitative Laser Light Sheet Measuring Techniques in Turbomachinery Components
Measurement Science and Technology, 11, pp. 1023-1035., 2000.

[105] SARAVANAMUTTOO, H. I. H.
Recommended Practices for Measurement of Gas Path Pressures and Temperatures for Performance Assessment of Aircraft Turbine Engines and Components
North Atlantic Treaty Organisation, AGARD Advisory Report No. 245, 1990.

[106] SCHARR, H.; JÄHNE, B.; BÖCKLE, S.; KAZENWADEL, J.; KUNZELMANN, T.; SCHULZ, C.
Flame Front Analysis in Turbulent Combustion
22nd DAGM Symposium, Kiel, Germany, Sept. 13-15 2000.

[107] SCHILDMACHER, K.-U.
Experimentelle Charakterisierung der Instabilitäten vorgemischter Flammen in Gasturbinen-Brennkammern
Dissertation, Faculty of Mechanical Engineering, University of Karlsruhe, 2005.

[108] SCHILDMACHER, K.-U.; HOFFMANN, A.; SELLE, L.; KOCH, R.; SCHULZ, C.; BAUER, H.-J.; POINSOT, T.; KREBS, W.; PRADE, B.
Unsteady Flame and Flow Field Interaction of a Premixed Model Gas Turbine Burner
Proceedings of the Combustion Institute, 31, pp. 3197-3205, 2007.

[109] SCHNEIDERS, T.
Laserspektroskopische Untersuchung instationärer Strahlmischungprozesse in Gasturbinen-Vormischbrennern mit einem Tracer-LIF-Verfahren
Dissertation, Faculty of Mechanical Engineering, Ruhr-Universität Bochum, 2001.

[110] SCHNEIDERS, T.; HOEREN, A.; MICHALSKI, B.; PFOST, H.; SCHERER, V.
Investigation of Unsteady Gas Mixing Processes in Gas Turbine Burners Applying Tracer-LIF Method
Proceedings of ASME Turbo Expo, 2001-GT0049, 2001.

[111] SCHOENUNG, S. M.; HANSON, R. K.
Temporally and Spatially Resolved Measurements of Fuel Mole Fraction in a Turbulent CO Diffusion Flame
Proceedings of the Combustion Institute, 19, pp. 449-458, 1982.

[112] SCHULZ, C.; DREIZLER, A.; EBERT, V.; WOLFRUM, J.
Laser-Based Combustion Diagnostics
Springer Handbook of Experimental Fluid Dynamics, edt. by C. Tropea, A. Yarin and J. F. Foss, pp. 1241-1315, Springer-Verlag, Berlin Heidelberg, 2007.

[113] SCHULZ, C.; KOCK, B. F.; HOFMANN, M.; MICHELSEN, M.; WILL, S.; BOUGIE, B.; SUNTZ, R.; SMALLWOOD, G.
Laser-induced Incandescence: Recent Trends and Current Questions
Applied Physics B-Lasers and Optics, 83, pp. 333–354, 2006.

[114] SCHULZ, C.; SICK, V.
Tracer-LIF Diagnostics: Quantitative Measurement of Fuel Concentration, Temperature and Fuel/Air Ratio in Practical Combustion Systems
Progress in Energy and Combustion Science 31, pp. 75-121, 2005.

[115] SETTLES, G. S.
Schlieren and Shadowgraph Techniques: Visualizing Phenomena in Transparent Media
Springer Verlag, Berlin Heidelberg, 2001.

[116] SIEMENS AG
66 Million Euros for New Burner Test Center - The Energy sector lays the foundation stone for a gas turbine burner test center in Berlin
https://newscenter.siemens.com/siemens-news/index.php?webcode=50001519&lang=en (accessed online in November 2013)

[117] SMITH, G. P.; GOLDEN, D. M.; FRENKLACH, M.; MORIARTY, N. W.; EITENEER, B.; GOLDENBERG, M.; BOWMAN, C. T.; HANSON, R. H.; SONG, S.; GARDINER JR., W. C.; LISSIANSKI, V. V.; QUIN, Z.
GRI-MECH 3.0
http://www.me.berkeley.edu/gri_mech/ (accessed online in May 2013)

[118] STODOLA, A.
Steam and Gas Turbines
McGraw-Hill, New York, 1927.

[119] STOPPER, U.; AIGNER, M.; MEIER, W.; SADANANDAN, R.; STÖHR, M.; KIM, I. S.
Flow Field and Combustion Characterization of Premixed Gas Turbine Flames by Planar Laser Techniques
Journal of Engineering for Gas Turbine and Power, 131, 021504 (8 pages) 2009.

[120] STREB, H.; PRADE, B.; HAHNER, T.; HOFFMANN, S.
Advanced Burner Development for the Vx4.3A Gas Turbines
Proceedings of the ASME Turbo Expo, 2001-GT-0077, 2001.

[121] STRICKER, W.; LÜCKERATH, R.; MEIER, U.; MEIER, W.
Temperature Measurements in Combustion - Not Only With CARS: a Look Back at One Aspect of the European CARS Workshop
Journal of Raman Spectroscopy, vol. 34 issue 12 (Proceedings of the European Conference on Nonlinear Optical Spectroscopy (ECONOS) Besançon, France, 30 March–1 April, 2003), pp. 922-931, 2003.

[122] SUN, D.; GANG, L.; ZHOU, H.; YAN, Y.
Flame Stability Monitoring and Characterization Through Digital Imaging and Spectral Analysis
Measurement Science and Technology, 22, 114007 (9 pp.), 2011.

[123] TAYLOR, A. M. K. P.
Instrumentation for Flows with Combustion
Academic Press Limited, London, United Kingdom, 1993.

[124] THURBER, M. C.
Acetone Laser-Induced Fluorescence for Temperature and Multiparameter Imaging in Gaseous Flows
Dissertation, Thermosciences Division, Department of Mechanical Engineering, Stanford University, 1999.

[125] THURBER, M. C.; GRISCH, F.; HANSON, R. K.
Temperature Imaging with Single- and Dual-wavelength Acetone Planar Laser-induced Fluorescence
Optical Letters, 22, pp. 251-253, 1997.

[126] THURBER, M. C.; HANSON, R. K.
Pressure and Composition Dependencies of Acetone Laser-induced Fluorescence with excitation at 248, 266, and 308 nm
Applied Physics B-Lasers and Optics, pp. 229-240, 1999.

[127] TROPEA, C.
Laser Doppler Anemometry: Recent Developments and Future Challenges
Measurement Science and Technology, 6, pp. 605-619, 1995.

[128] VAN KAMPEN, J. F.
Acoustic Pressure Oscillations Induced by Confined Turbulent Premixed Natural Gas Flames
Dissertation, University of Twente, Enschede, 2006.

[129] VOS, I.
The Impact of Wind Power on European Natural Gas Markets
International Energy Agency, OECD/IEA, Paris, 2012.

[130] WALSH, K. T.; LONG, M. B.; TANOFF, M., A.; SMOOKE, M. D.
Experimental and Computational Study of CH, CH, and OH* in an Axisymmetric Laminar Diffusion Flame*
Proceedings of the Combustion Institute, 27, pp. 615-623, 1998.

[131] WARNATZ, J.; MAAS, U.; DIBBLE, R. W.
Combustion
Springer-Verlag, Berlin Heidelberg New York, 2006.

[132] WILLERT, C.; HASSA, C.; STOCKHAUSEN, G.; JARIUS, M.; VOGES, M.; KLINNER, J.
Combined PIV and DGV Applied to a Pressurized Gas Turbine Combustion Facility
Measurement Science and Technology, 17, pp. 1670-1679, 2006.

[133] WITZEL, B.; HEINZE, J.; KOCK, B. F.; STOCKHAUSEN, G.; STREB, H.; VAN KAMPEN, J.; SCHULZ, C.; WILLERT, C.; FLEING, C.
Application of Endoscopic OH-Chemiluminescence Measurements at a Full-Scale High-Pressure Gas Turbine Combustion Test Rig*
Proceedings of the ASME Turbo Expo, GT2012-68965, 2012.

[134] WOLFF, D.
Quantitative laserdiagnostische Untersuchung der Gemischaufbereitung in technischen Verbrennungssystemen
Dissertation, Faculty of Physics, University of Bielefeld, 1995.

[135] WOLFRUM, J.
Lasers in Combustion: From Basic Theory to Practical Devices
Proceedings of the Combustion Institute, 27, pp. 1-41, 1998.

[136] YUEN, L. S.; PETERS, J.; LUCHT, R. P.
Pressure Dependence of Laser-induced Fluorescence from Acetone
Applied Optics, 36, pp. 3217-3277, 1997.

[137] ZALICKI, P; ZARE, R. N.
Cavity Ring-Down Spectroscopy for Quantitative Absorption Measurements
J. Chem. Phys. 102, pp. 2708-2717, 1995.

[138] ZELDOVICH, J.
The Oxidation of Nitrogen in Combustions and Explosions
Acta Physicochimica U.R.S.S., 21, pp. 577–628, 1946.

Appendix A Properties of Methane and Frequently Used Tracers

	Methane	**Acetone**	**3-Pantanone**	**Acetaldehyde**	**Biacetyl**	**Toluene**
Molecular weight (g/mol)	16.0	58.1	86.1	44.1	86.1	92.1
Density at 25°C (g/cm^3)	-	0.79	0.81	0.77	0.98	0.87
Boiling point (°C)	−161.5	56.1	102.0	20.1	88.0	110.6
Heat of vaporisation at 25°C (kj/mol)	-	31.0	38.5	25.5	-	38.0
Flash point (°C)	−188	−18	7	−27	3	4.5-7
Autoignition temperature in air (°C)	537-632	465-727	425-608	175-275	365	480-810
Flammability limits in 1 bar air (% vol)	5.0-15	2.6-13	1.6-8	4.0-60	2.4-13	1.2-7.1

Gas-phase viscosity at 100°C (µPa s)	13.4	9.5	8.2	10.7	-	8.8
Gas-phase diffusion coeff. (1 bar air, 100°C) (cm^2 s^{-1})	0.344	0.166	0.129	0.218	0.135	0.132

Table 5.1: Relevant physical and thermodynamic properties of most frequently used organic tracer molecules compared to methane (compilation derived from [114])

Appendix B Tracer Gas Supply Facility

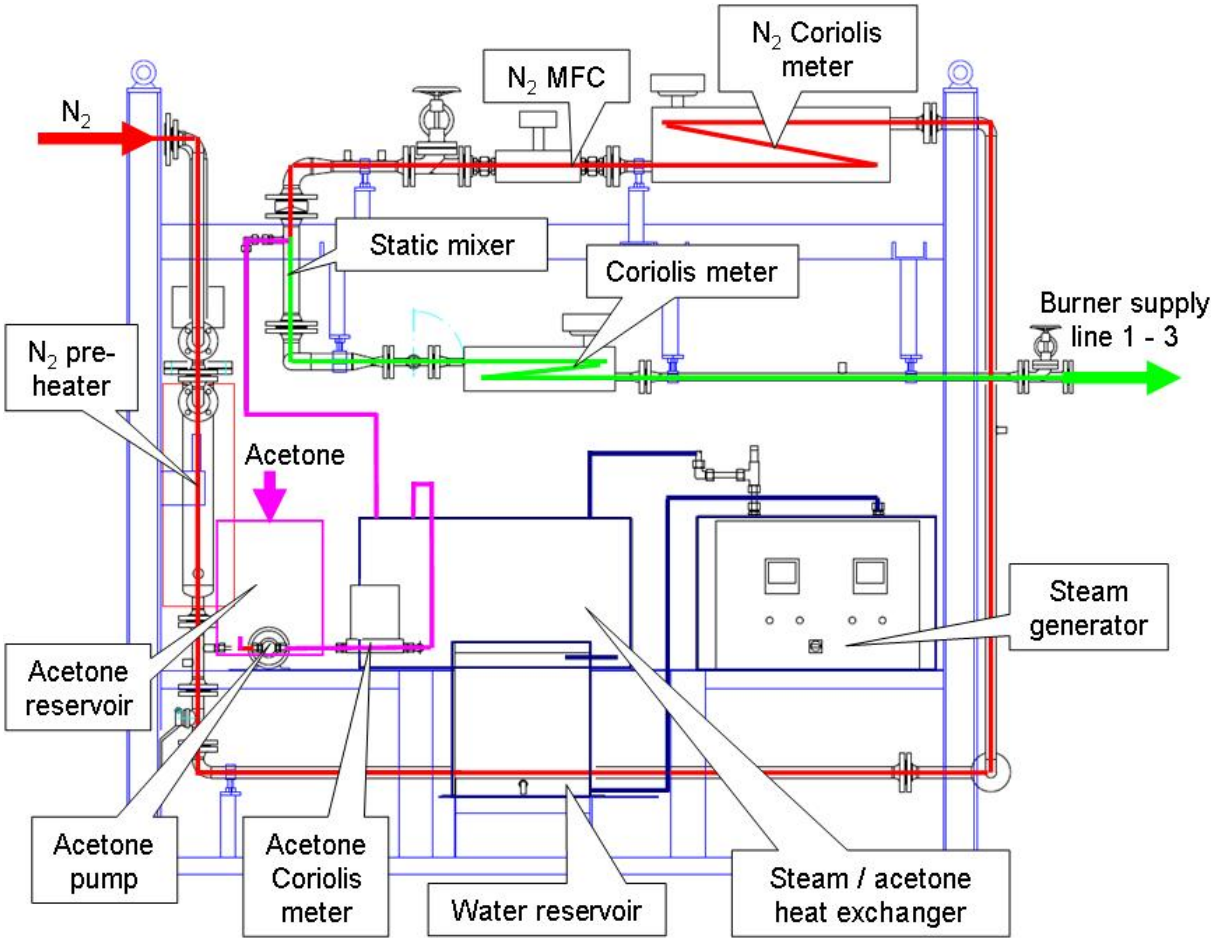

Figure B.1: Sketch of the tracer gas supply facility

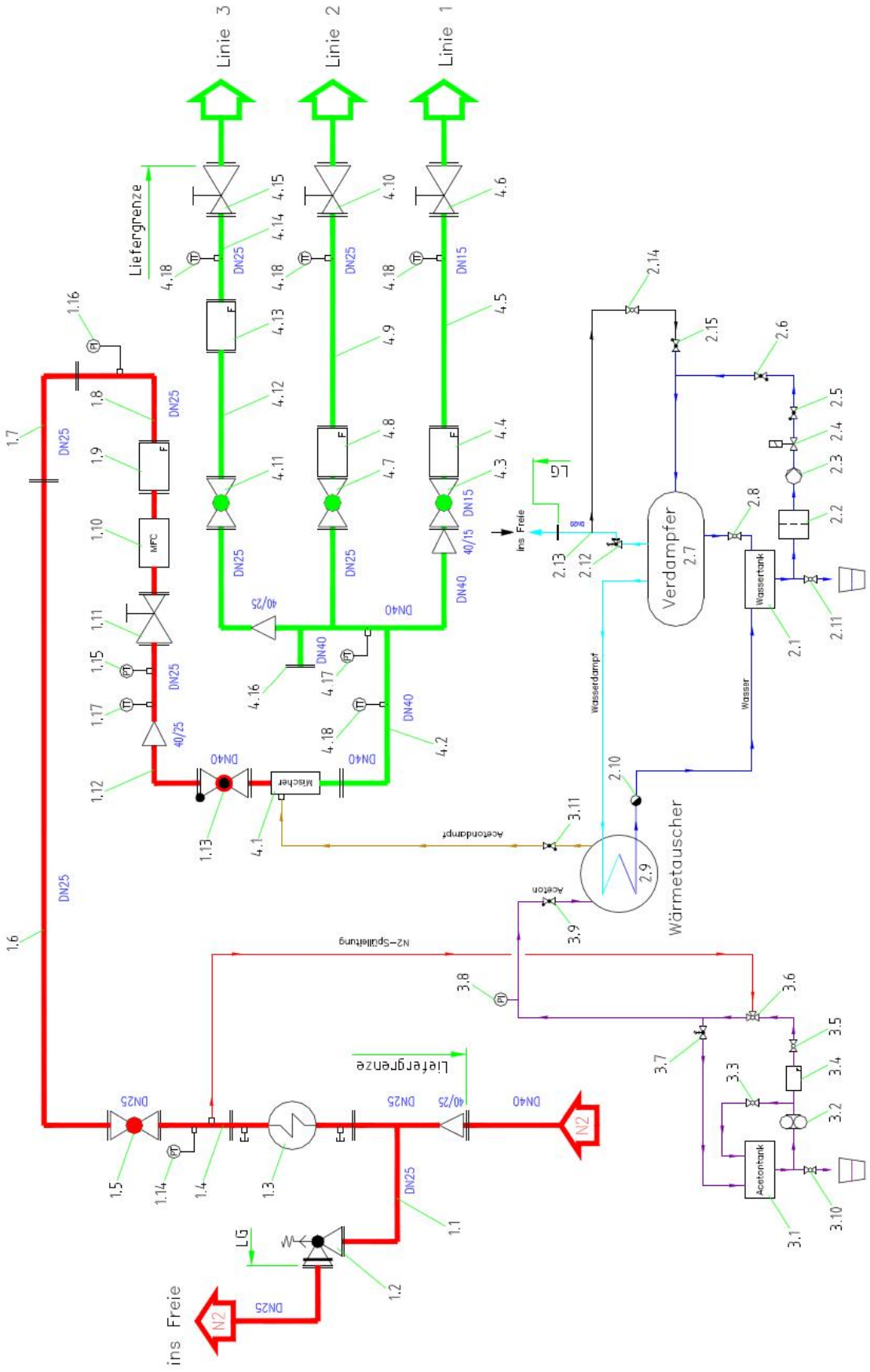

Figure B.2: Piping and instrumentation diagram of the tracer gas supply facility

Messstelle	Typ	Messbereich	Modul	Kanal
t 1	Pt 100 Widerstandsthermometer (1/3 Klasse B)	0-100°C	4	2
t 2	Pt 100 Widerstandsthermometer (1/3 Klasse B)	0-100°C	4	3
t 3	Pt 100 Widerstandsthermometer (1/3 Klasse B)	0-100°C	4	4
t Verteiler	Pt 100 Widerstandsthermometer (1/3 Klasse B)	0-100°C	4	1
t N_2	Pt 100 Widerstandsthermometer (1/3 Klasse B)	0-100°C	4	5
p 1	Sitrans P, DS III Differenzdruckmessumformer	0-75 mbar	4	8
p2	Sitrans P, DS III Differenzdruckmessumformer	0-350 mbar	4	11
p3	Sitrans P, DS III Differenzdruckmessumformer	0-350 mbar	4	10
p N_2	Sitrans P, DS III Differenzdruckmessumformer	0-7000 mbar	4	12
p Verteiler	Rosemount 1151 SMART Differenzdruckmessumformer	0-7000 mbar	4	7
p CN_2	Manometer, Absolutdruck	0-1600 mbar	-	-
p Aceton	Manometer, Absolutdruck	0-16000 mbar	-	-
Coriolis N_2	Sitrans FC MASS 2100 Massenstrom	0-90 g/s	3	7
	Sitrans FC MASS 2100 Dichte	0-0,002 g/cm³	3	8
Coriolis 1	Sitrans FC MASS 2100 Massenstrom	0-15 g/s	3	1
	Sitrans FC MASS 2100 Dichte	0-0,002 g/cm³	3	2
Coriolis 2	Sitrans FC MASS 2100 Massenstrom	0-55 g/s	3	3
	Sitrans FC MASS 2100 Dichte	0-0,002 g/cm³	3	4
Coriolis 3	Emerson CMF100 Massenstrom	0-90 g/s	3	5
	Emerson CMF100 Dichte	0-0,002 g/cm³	3	6
Cori-Flow	Bronkhorst Cori-Flow	0-10 g/s	3	10

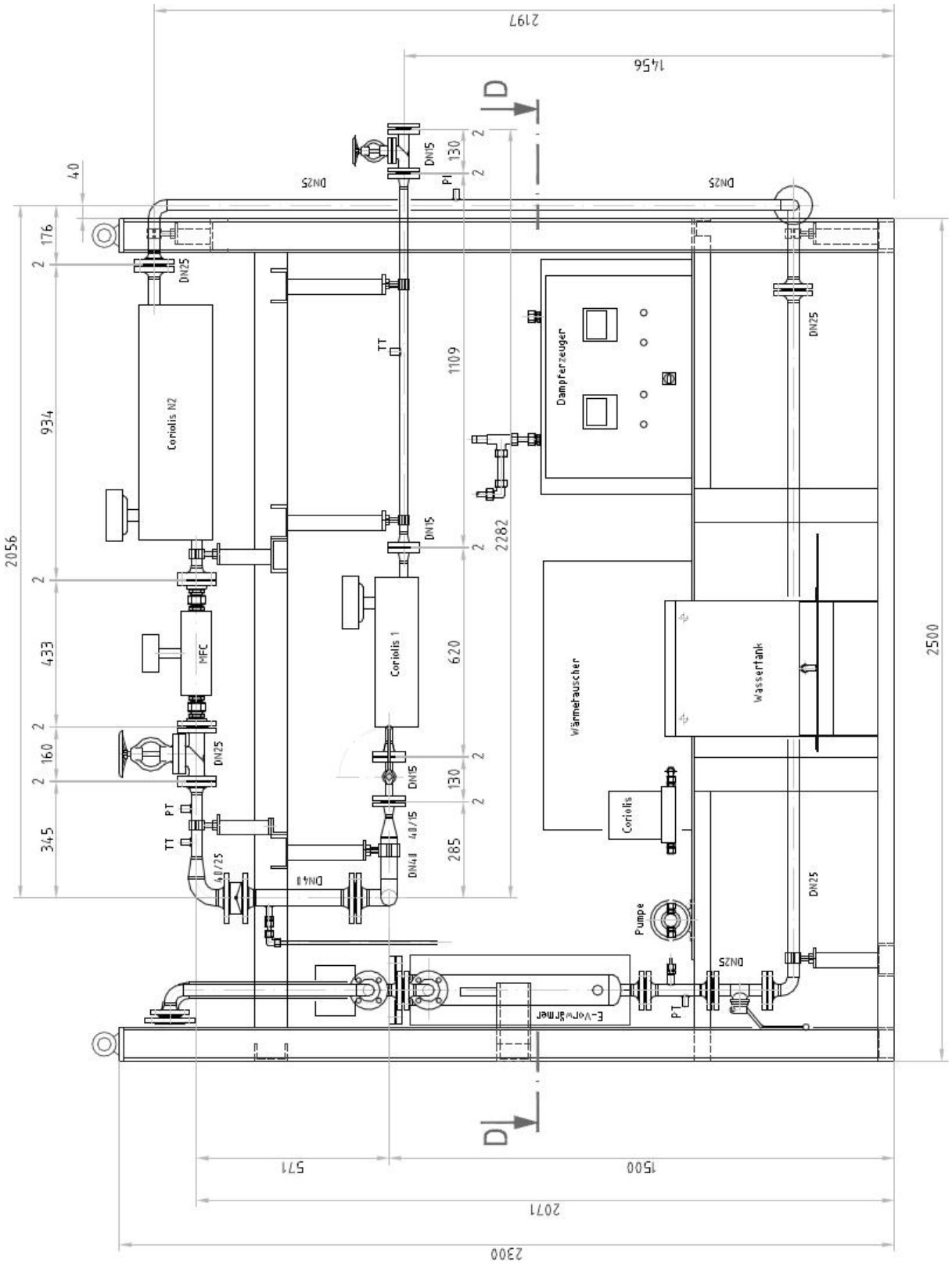
2197
1456
D
DN15
130
PI
DN25
40
176
934
2056
433
160
345
TT
Coriolis N2
MFC
DN25
PT
TT
40/25
DN40
DN15
1109
2282
620
Coriolis 1
DN15
130
40/15
DN40
285
Dampferzeuger
DN25
Wärmetauscher
Wassertank
2500
Coriolis
DN25
Pumpe
DN25
E-Vorwärmer
PT
D
571
1500
2071
2300

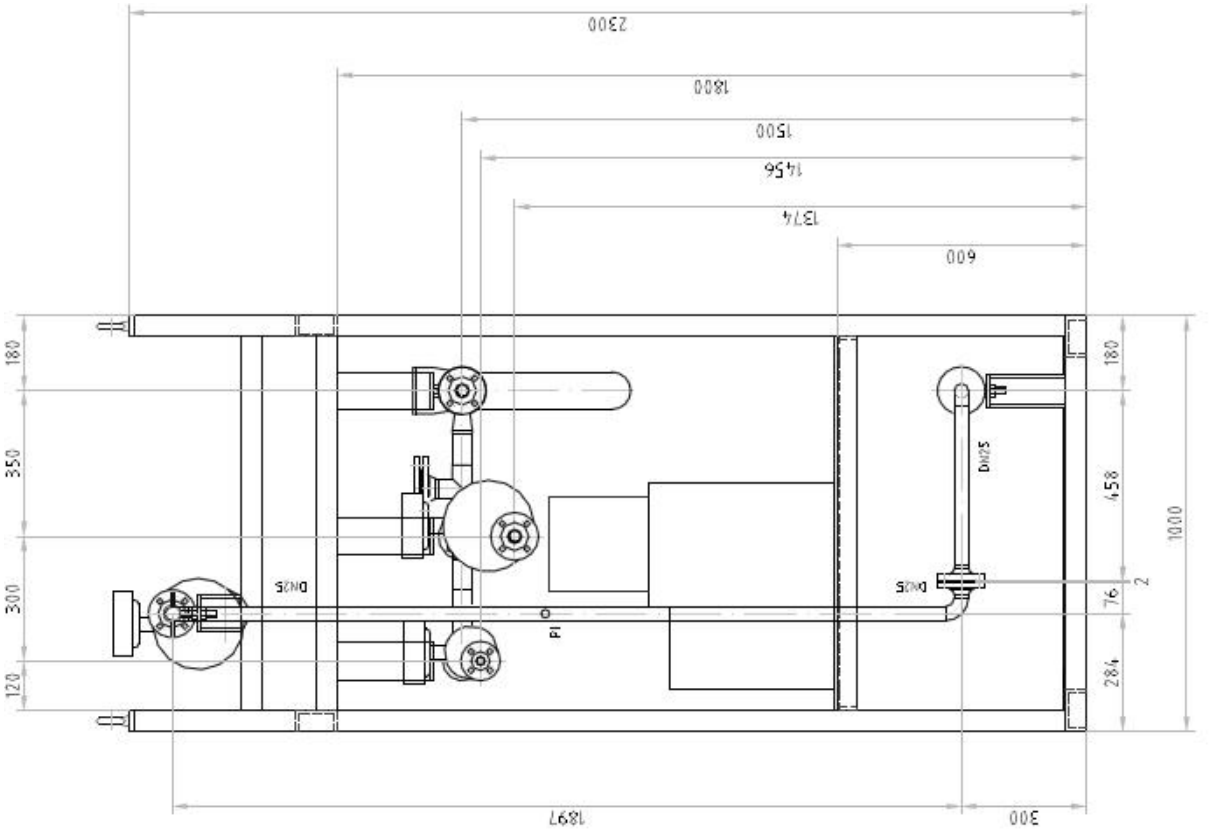
2300
1800
1500
1456
1374
600
180
350
300
120
180
458
76
284
1000
2
DN25
DN25
PI
1897
300

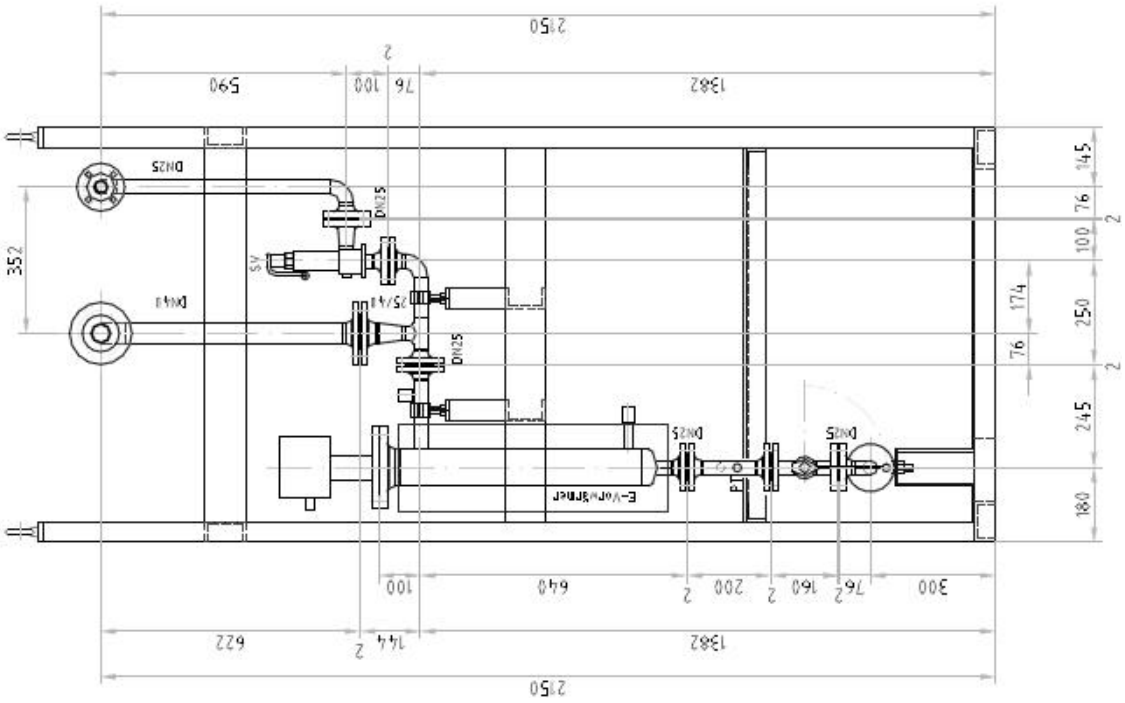
2150
2
590
100
76
1382
DN25
DN25
DN25
DN25
DN25
DN25
PI
352
145
76
100
174
250
245
180
2
2
2
100
640
200
160
76
300
622
144
1382
2150

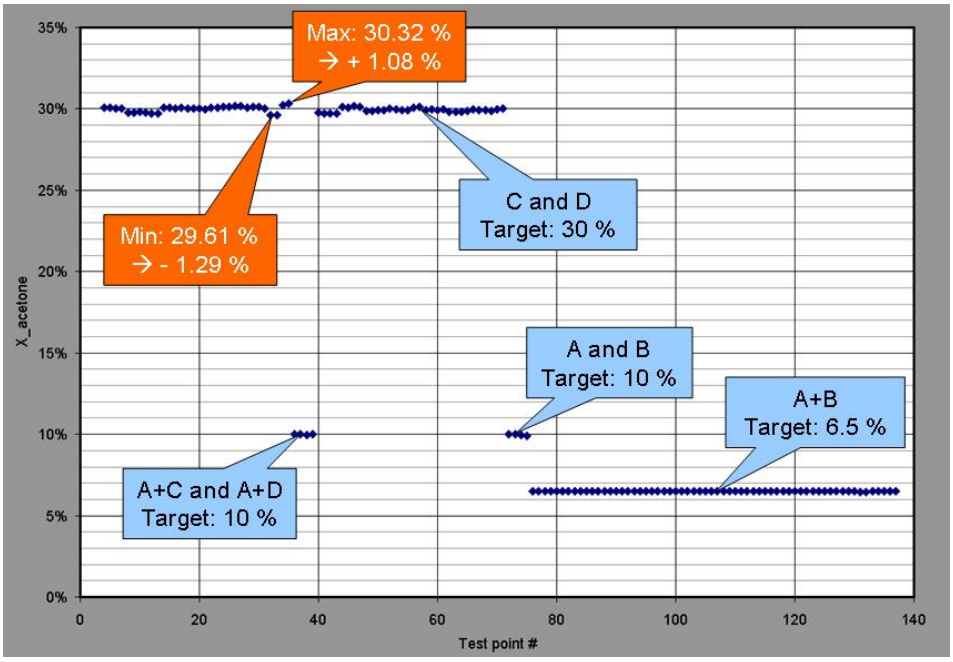

Figure B.3: Measured acetone concentrations of a typical test day

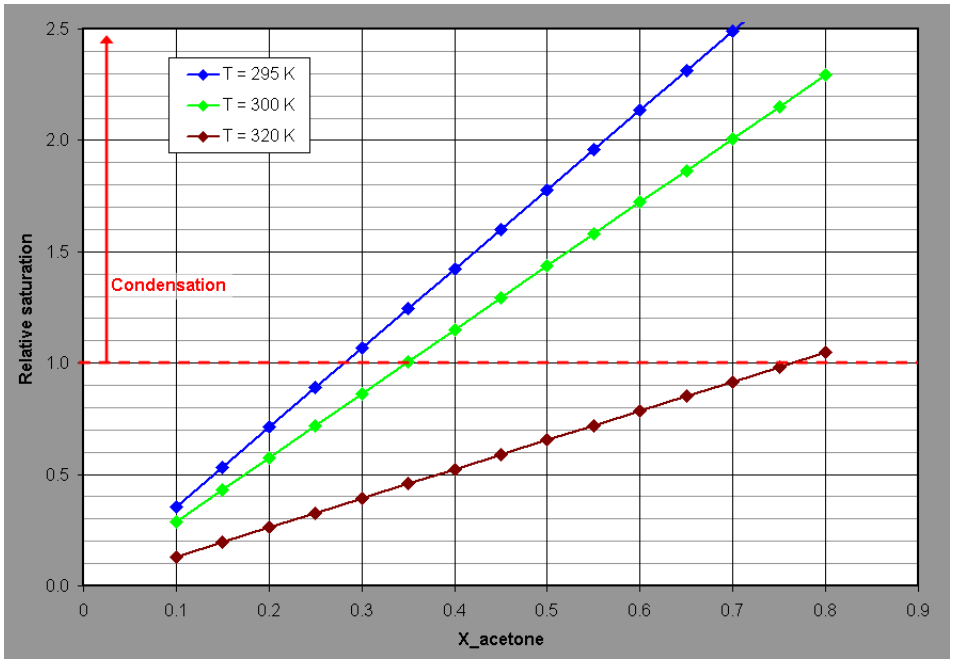

Figure B.4: Estimation of relative acetone saturation in air at different temperature levels

Appendix C UV-Transparent Acrylic Glass

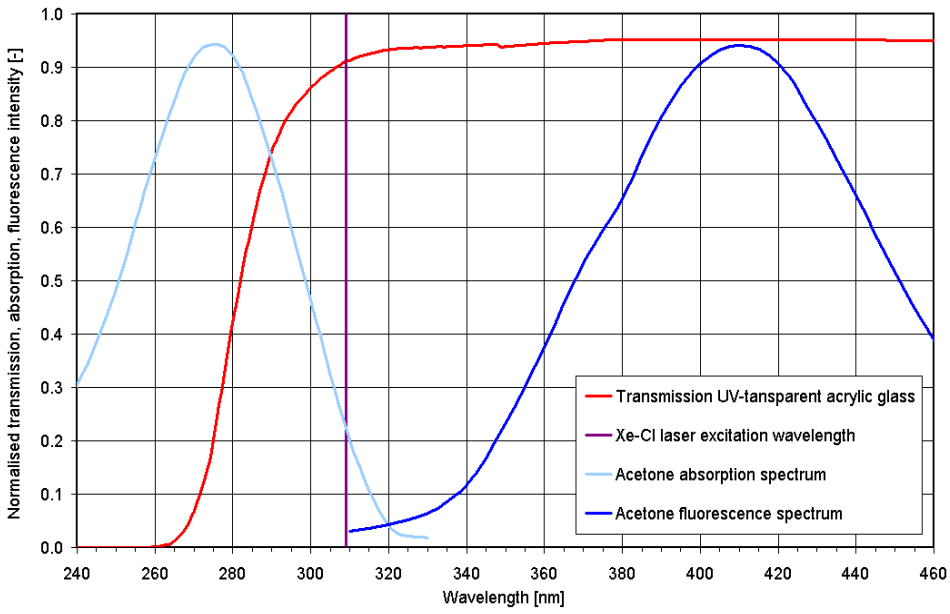

Figure C.1 Comparison of absorption and fluorescence spectra from acetone with laser excitation wavelength and transmission spectrum of UV-transparent acrylic glass

Appendix D SGT6-8000H Cold Flow Test Rig

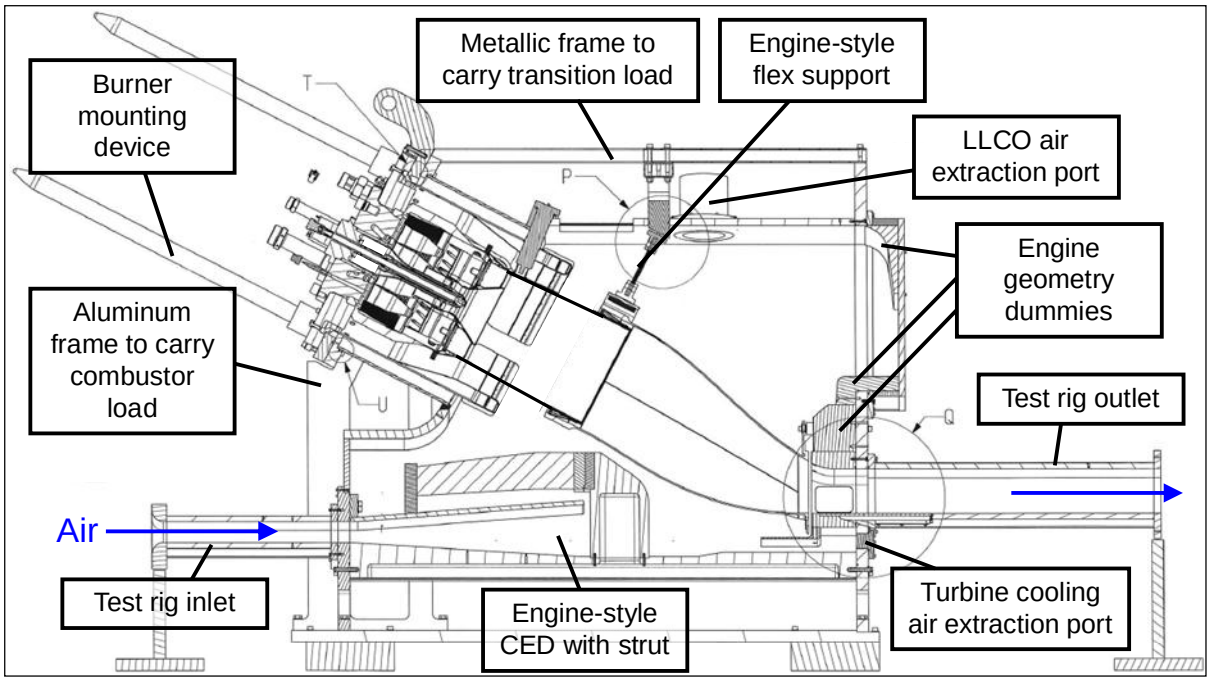

Figure D.1: Sectional drawing with main features

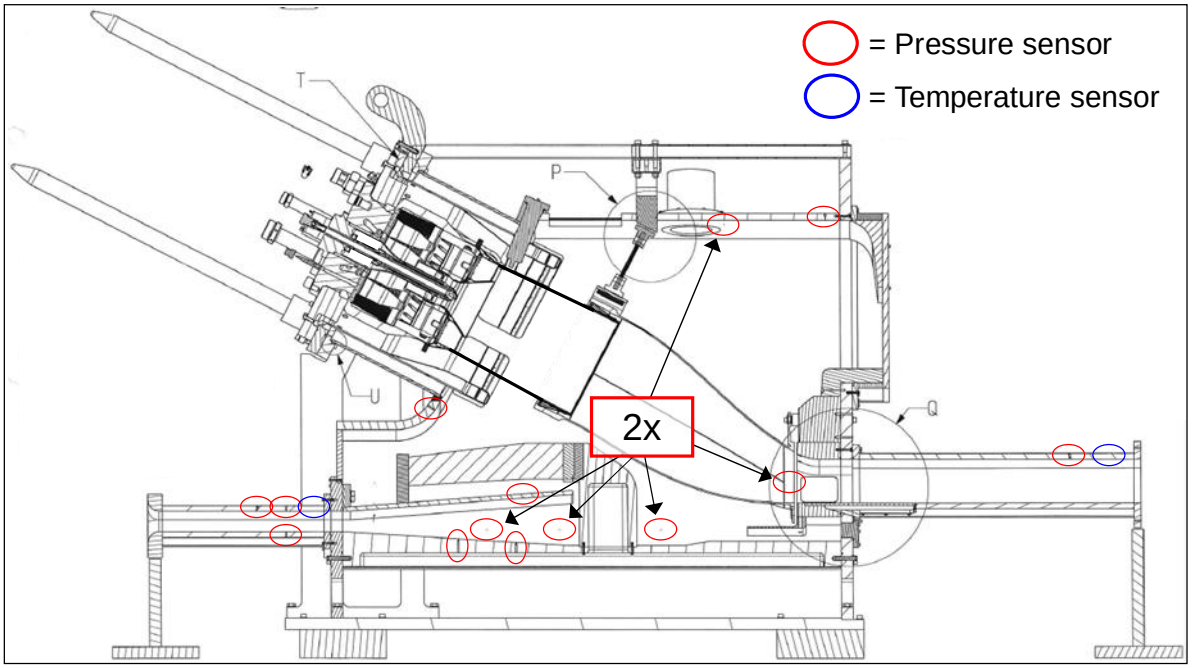

Figure D.2: Test rig instrumentation (temperature and static pressure)

Appendix E Chemiluminescence Probe Sensitivity

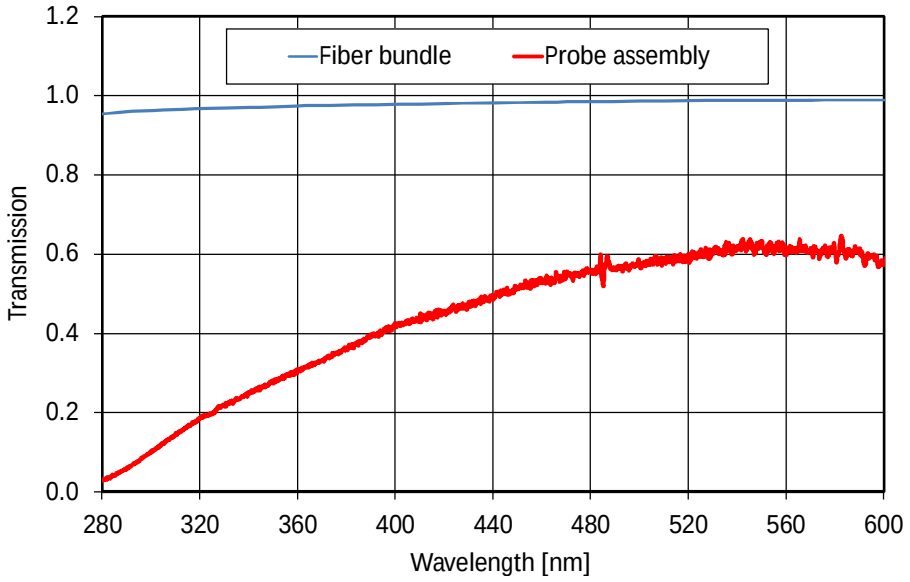

Figure E.1: Spectral sensitivity of the chemiluminescence probe assembly as used for the correction of the measured chemiluminescence spectra